Experimentelle Untersuchungen des Nachlaufverhaltens und der Dynamik einzelner schwimmender Windenergieanlagen sowie Anlagen im Parkverbund

Stanislav Rockel

Von der Fakultät für Mathematik und Naturwissenschaften
der Carl von Ossietzky Universität Oldenburg
zur Erlangung des Grades und Titels eines

Doktors der Naturwissenschaften
Dr. rer. nat.

angenommene Dissertation

von Herrn Stanislav Rockel
geboren am 22.07.1982 in Kujbyschew

Gutachter: Prof. Dr. Joachim Peinke
Zweitgutachter: Prof. Dr. Martin Kühn
Tag der Abgabe: 20.02.2017
Tag der Disputation: 01.06.2017

Inhaltsverzeichnis

Abbildungsverzeichnis

Abstract

Wind energy, in particular offshore wind energy, is a key solution for increasing energy demands from renewable energy sources. Recent offshore wind turbines use monopiles or tripods as foundations, which are feasible in shallow waters up to a depth of 50 m. Such areas are rare and often already exploited. Therefore, the application of offshore wind turbines in deep water is considered to utilize wind energy more flexible, overcoming current areal limitations. In particular, offshore wind turbines installed on floating platforms are considered a feasible solution.

Given that for economical reasons wind turbines are operated in wind farms, knowledge of the interaction of wind turbines via wakes is of particular interest for reliable operation and power yield prediction of such farms. Floating wind turbines possess additional degrees of freedom when compared to bottom fixed turbines. Those impact their operational conditions and the wake development, thus the inflow of further turbines within a wind farm. A detailed understanding of the influence of the degrees of freedom on the aerodynamic performance of the rotor and its wake characteristics are important when planing and designing layouts of floating wind turbines and farms.

This work provides insights into wake dynamics induced by turbines with additional degrees of freedom, in particular pitch motion. Therefore, wind tunnel experiments with models of bottom fixed wind turbines and wind turbines allowed to freely oscillate in streamwise direction were performed. The turbines were operated under various turbulent inflow conditions while their wakes were measured and compared to identify motion induced wake effects. Firstly, wake measurements of single turbines as well as of two turbines in streamwise displacement were performed using the optical measurement method *particle image velocimetry*. The provided results allow for characterization of averaged statistical wake dynamics. Secondly, simultaneous measurements of 16 hot-wire anemometers were performed for flow investigations in time-, spectral- and spatial-domain. It was found that, by deflecting the flow, platform pitch motion has a strong impact on the averaged development of the wake structure and its fluctuations. Structures found in the wake of fixed turbines are dampened or smeared out by floating turbines. Also, wake characteristics are strongly susceptible to the inflow conditions with varying influence of the fixed or floating turbine type, depending on the inflow turbulence level. This potentially results in variable operational conditions in terms of performance and loads for downstream floating wind turbines, that differ from those of bottom fixed turbines and have to be addressed in the design.

Zusammenfassung

Windenergie, im Besonderen Offshore Windenergie, spielt eine Schlüsselrolle zur Erfüllung des Energiebedarfs aus erneuerbaren Quellen. Aktuelle Offshore-Windenergieanlagen nutzen Monopiles oder Tripods als Fundamente, die in flachen Gewässern bis zu einer Wassertiefe von 50 m rentabel einsetzbar sind. Solche Gewässer sind rar und häufig anderweitig genutzt. Daher werden Einsatzmöglichkeiten von Offshore-Windenergieanlagen in tiefen Gewässern betrachtet, um Windenergie flexibler und unabhängig von aktuellen arealen Einschränkungen zu nutzen. Als eine realisierbare Lösung werden vorrangig Offshore-Windenergieanlagen auf schwimmenden Plattformen erachtet.

Da Windenergieanlagen aus ökonomischen Gründen in Windparks betrieben werden, ist die Kenntniss der gegenseitigen Beeinflussung durch ihre Nachlaufströmungen von erhöhtem Interesse für den zuverlässigen Betrieb und die Leistungsprognose von Windparks. Schwimmende Windenergieanlagen haben im Vergleich zu Anlagen auf festen Fundamenten zusätzliche Freiheitsgrade. Diese beeinflussen die Betriebsbedingungen und die Entwicklung der Nachlaufströmungen, somit die Einströmung weiterer Anlagen innerhalb des Windparks. Ein detailliertes Verständnis der Einflüsse der Freiheitsgrade auf das charakteristische, aerodynamische Verhalten des Rotors und der Nachlaufströmung ist bei der Planung und Auslegung schwimmender Windenergieanlagen erforderlich.

Diese Arbeit vermittelt Erkenntnisse über die Dynamik der Nachlaufströmungen, die durch Windenergieanlagen mit zusätzlichen Freiheitsgraden, hier der Neigungs-Bewegung, verursacht werden. Es wurden Windkanalexperimente mit Modellen von feststehenden Windenergieanlagen und mit Anlagen, die frei in Strömungsrichtung oszillieren können, durchgeführt. Die Anlagen wurden unter unterschiedlichen turbulenten Einströmungsbedingungen betrieben. Ihre Nachlaufströmungen wurden vermessen, um Effekte die durch Anlagenbewegungen hervorgerufen werden zu identifizieren. Erstens wurden Nachlauf-Messungen einzelner Anlagen als auch zweier hintereinanderstehender Anlagen mittels der optischen, nicht-invasiven Methode *particle image velocimetry* durchgeführt. Die erlangten Ergebnisse ermöglichen eine Charakterisierung gemittelter, statistischer Dynamiken von Nachlaufströmungen. Zweitens wurden Messungen mit 16 Hitzdrähten gleichzeitig durchgeführt um zeit-, frequenz- und ortsaufgelöste Strömungsuntersuchungen zu ermöglichen. Die Untersuchungen ergaben, dass Neigungsbewegungen von Windenergieanlagen-Fundamenten, die gemittelten Strukturen der Nachlaufströmungen und deren Fluktuationen durch Ablenkung der Strömung sehr stark beeinflussen. Vorhandene Nachlauf-Strukturen, die bei feststehenden Anlagen eindeutig vorhanden sind, werden in den Nachlaufströmungen

schwimmender Anlagen gedämpft und ausgeschmiert. Zusätzlich sind Charakteristika von Nachlaufströmungen stark durch die vorherrschenden Einströmungsbedingungen beeinflusst. Der Einfluss des Anlagentyps, feststehend oder schwimmend, variiert stark mit der Turbulenzintensität der Einströmung. Das resultiert in potenziellen Schwankungen der Betriebsbedingungen, der erzeugten Leistungen und vorherrschenden Lasten von schwimmenden Windenergieanlagen, die sich deutlich von denen aktueller Windenergieanlagen unterscheiden und in den Auslegungen der Anlagen berücksichtigt werden müssen.

1 Introduction

In this work the influence of platform motion on the performance and wake development of floating wind turbines is investigated using model wind turbines in wind tunnel experiments.

1.1 Motivation

Wind energy is a key factor for the goal to cover increasing energy demands by using renewable energy sources. An increase in installed power is found for wind energy onshore and offshore, where offshore wind energy is expected to have highest growth rates due to sustained winds which are unaffected by complex terrain [6]. Also, general regulations in terms of e.g. distances to urban areas, noise production and disturbance of air traffic infrastructure make offshore wind energy a favorable choice. For economic reasons, wind turbines are operated in farms, whose implementations onshore are limited due to space constraints. Recently installed offshore wind turbines use monopiles or tripods as foundations, which are feasible in shallow waters up to a depth of 50 m. Such shallow areas are rare and already exploited to a large extend [3] often being nature reserves or protected landscapes for breeding wildlife. Furthermore, some countries lack shallow water areas in their surroundings [3], making the possibilities of using tripods and monopiles very limited or impossible. Therefore, the application of offshore wind turbines also in deep water is of great interest and solutions have to be found to utilize wind energy more flexible, overcoming current areal limitations due to space and water depth.
For reliable operation and power prediction of wind farms the interaction of wind turbines via wakes is of particular interest and shows the need of a deeper knowledge of the wake development. Wind turbines set up on floating platforms possess additional degrees of freedom when compared to bottom fixed turbines. Additional motions of a floating wind turbine impact its operational conditions and the wake development, thus the inflow of further turbines within a wind farm. For deep water areas, several concepts have been developed for floating offshore wind turbines. A detailed understanding of the influence of the degrees of freedom such as pitch, sway and heave on the aerodynamic performance of the rotor and its wake characteristics are important to determine the design space for floating wind turbines. Knowledge about the inflow conditions allow for finding an optimized design space for floating wind turbines by facilitating proper load and fatigue calculations. Therewith, the cost of energy of single floating wind turbines and floating wind farms can be optimized [2, 5].

In addition, proper modeling of wake development plays an important role in

order to maximize power output of the turbine ensemble [1]. A small amount of field and experimental data about the operational conditions of floating wind turbines is available. Experimental data is needed to validate the performance of computational models.
This thesis aims to increase the insight into wake dynamics introduced by turbines with additional degrees of freedom, with an emphasis on pitch motion. As often the case for wind tunnel experiments, the found effects are not expected to directly scale up to full size wind turbines. All used methods - experimental and analytical - are in parallel applied to a classical bottom fixed model wind turbine, where extensive work was done to get insights into aerodynamic effects and how those can be transferred to full scale turbines. This allows for comparative studies of floating wind turbines in model scale and for derived general conclusions for full scale experiments and theoretical models. Investigations to cover the effects of a model floating wind turbine were performed in the diploma thesis of Rockel [4], where a small scale floating turbine was used in wind tunnel experiments set up in a water basin. The motion and corresponding power output of the turbine in comparison to a fixed turbine was investigated. The results from wind tunnel experiments of the diploma thesis suggest a strong simplification of the setup and a systematic separation of the degrees of freedom in order to isolate the effects of each degree of freedom.

1.2 Outline of this thesis

This thesis is structured in three major investigations, that provide detailed insights into the wake development of floating wind turbines subject to free pitch motion introduced by varying inflow conditions. A comprehensive literature review precedes each chapter to embed the work in a broader context.

In the first part, wake measurements were performed using the optical measurement method *particle image velocimetry (PIV)*, which allows for non-invasive flow measurements, with high spatial resolution but a low temporal resolution. The mean influence of oscillatory motion on the development of the wake at downstream positions from $x/D = 1$ to $x/D = 7$ is investigated. For each measurement plane, 2500 images of the flow were taken and statistically evaluated. All measurements were performed in a comparative form, i.e. the measurements were taken for a classical bottom fixed turbine and under unchanged operational conditions for an oscillating turbine. Hence, effects caused by the motion of the turbine on the wake dynamics are isolated. The provided results allow for deriving averaged statistics for wake dynamics. The discussed quantities contain averaged mean flows and turbulent characteristics of the flow, such as Reynolds stresses. The experimental results are compared to several

analytical wake models revealing discrepancies between measured and predicted wake shapes. The results provide insight on how the wake characteristics transition from near wake to far wake and characterize varying inflow conditions of a downwind turbine, depending on the fixed or floating wind turbine.

The second part deals with wake effects between turbines, which is a relevant problem for wind power utilization in wind farms and is also crucial for turbine placement. Wind tunnel experiments with two model wind turbines in streamwise displacement, subjected to turbulent inflow, were performed. Again, the measurements were performed under identical conditions for bottom fixed and oscillating wind turbine models. The inflow and the far wake of the first turbine as well as the near wake of the second turbine in the wake of the first were measured using PIV. The inflow turbulence of the first and the second turbine were characterized and compared using eddy viscosity and mixing length obtained from the measurement data. These quantities reveal further induced differences in the turbulence of the wakes and inflows between the fixed and floating case, but also between the first and second turbine. The calibrated parameters eddy viscosities and mixing lengths obtained from experimental data provide a local profile rather than a fixed constant, which is usually used for simplified wake models. The introduced differences in the inflow are discussed in the context of the influence on averaged statistical quantities describing the wake dynamics.

The third part covers the influence of differing turbulent inflow conditions on the wake's structure of a floating wind turbine. Highly time-resolved measurements were taken using 16 hot-wire probes simultaneously in a rack at multiple downstream planes parallel to the rotor at x/D = 1-7. Two different inflow conditions, featuring high and low turbulence levels, were generated using an active grid. Changing inflows and wake patterns were characterized by means of averaged time statistics, distributions of fluctuations and analyses in spectral domain. Spatial analyses were performed by calculations of correlations between measurements of the 16 hot-wire probes. A low-dimensional representation of the flow using proper orthogonal decomposition was calculated, providing insights to the complexity of the wake structure and introduced changes due to the differing inflow conditions and oscillations of a floating wind turbine.

This work is then finalized by a short summary and suggested future work.

Literaturverzeichnis

[1] R. J. Barthelmie, S. C. Pryor, S. T. Frandsen, K. S. Hansen, J. G. Schepers, K. Rados, W. Schlez, A. Neubert, L. E. Jensen, and S. Neckelmann. Quantifying the Impact of Wind Turbine Wakes on Power Output at Offshore Wind Farms. *Journal of Atmospheric and Oceanic Technology*, 27(8):1302–1317, August 2010.

[2] CP Butterfield, W Musial, and J Jonkman. *Engineering challenges for floating offshore wind turbines*. 2007.

[3] AR Henderson, D Witcher, and CA Morgan. Floating support structures enabling new markets for offshore wind energy. *Proceedings of the EWEC*, 2009.

[4] S. Rockel. Dynamische Eigenschaften einer schwimmenden Modell-Windenergieanlage. *Diplomarbeit*, Oldenburg, 2011.

[5] Thomas Sebastian and Matthew Lackner. Analysis of the Induction and Wake Evolution of an Offshore Floating Wind Turbine. *Energies*, 5(12):968–1000, April 2012.

[6] A Zervos and C Kjaer. Pure power: wind energy scenarios up to 2030. 2008.

2 Experimental study on influence of pitch motion on the wake of a floating wind turbine model

Wind tunnel experiments were performed, where the development of the wake of a model wind turbine was measured using stereo Particle Image Velocimetry to observe the influence of platform pitch motion. The wakes of a classical bottom fixed turbine and a streamwise oscillating turbine are compared. Results indicate that platform pitch creates an upward shift in all components of the flow and their fluctuations. The vertical flow created by the pitch motion as well as the reduced entrainment of kinetic energy from undisturbed flows above the turbine result in potentially higher loads and less available kinetic energy for a downwind turbine. Experimental results are compared with four wake models. The wake models employed are consistent with experimental results in describing the shapes and magnitudes of the streamwise velocity component of the wake for a fixed turbine. Inconsistencies between the model predictions and experimental results arise in the floating case particularly the vertical displacement. Furthermore, it is found that the additional degrees of freedom of a floating wind turbine add to the complexity of the wake aerodynamics and improved wake models are needed, considering vertical flows and displacements due to pitch motion.

2.1 Introduction

Wind energy has become a major contributor to energy from renewable sources and is still projected to increase its portion to the overall energy supply. Offshore wind energy was found to have the highest potential to fulfill these demands, due to sustained winds which are unaffected by complex terrain [42]. Offshore wind turbines, which have been installed recently, use monopiles or tripods as foundations, which are feasible in shallow water up to a depth of 50 m. Such shallow areas are rare and are often already exploited [12], so solutions have to be found to produce wind energy in deeper water areas. Floating support structures for offshore wind turbines are possible alternatives to current bottom fixed foundations. A small amount of field and experimental data about the operational conditions of floating wind turbines is available.

The additional degrees of freedom of a floating platform will cause different operational conditions compared to fixed foundations. A detailed understanding of the influence of the degrees of freedom on aerodynamic performance, fatigue loads and finally the costs of floating wind turbines would allow an optimized design of

floating wind turbines [5].

The influence of various motions such as pitch, sway and heave on the aerodynamics of the rotor and the wake characteristics are important in determining the design space for proper load and fatigue calculations [34]. Most wind turbines are operated in arrays so proper modeling of wake development plays an important role in order to reduce fatigue loads of turbines positioned downstream and maximize power output of the turbine ensemble [2]. Experimental data is needed to validate the performance of computational models.

Feasibility studies have been performed to define the constraints for floating turbines installations [25]. The critical constraints as outlined are to establish a design basis for offshore turbines, reliable offshore substructures as well as low cost anchors and moorings. Simulations of the structural response have been performed by Jonkman *et al.* [14, 15]. The approach was expanding the FAST code for classical turbines with hydrodynamic wave-body interaction programs such as WAMIT, that covers hydrodynamic damping and wave excitation of the platform. A comparison of three concepts of floating platforms with land-based turbines showed an overall increase of loadings on all turbine components due to the floating platform, so a mechanically more robust design is required [16]. Further combinations of platform and turbine design have to be tested and economic aspects have to be considered in order determine an optimal design.

Matsukama *et al.* [23] performed motion analysis of a spar floating wind turbine under steady wind conditions. The effect of rotor rotation on the response of the floating platform was taken into account using blade element momentum theory and multibody dynamics theory, thus splitting the turbine into rotor, nacelle, tower and platform. It was found that motions like sway, roll and yaw are influenced by the gyroscopic moment of the rotor and that these motions drive variations in loads and power output of a turbine. A 9° static pitch of the platform was calculated for the rated wind speed of the turbine. The dynamic pitch of the platform was found to be the same on average, but oscillating around this value. Yaw and roll movement were estimated as well and found to drive the loads on the turbine and changes in variation in the power output.

Experimental investigations have been done on the structural response of floating support structures by Utsunomiya *et al.* [37]. The equation as posed by Morison, which accounts for inertia and drag force on a body in a flow, was used to determine the wave force on a spar body and to estimate response amplitudes of a spar bouy. Qualitative agreement was found between estimates from the equation and experiments performed in a wave basin but the need for further improvements was

stressed. A review of current literature on floating wind turbines is given in [39].

A preliminary study using the time averaged Unsteady Reynolds Averaged Navier-Stokes (URANS) method to simulate aerodynamic interaction of flow and pitch platform motion was performed by Matha *et al.* [22]. The effects of the mooring system dynamics on the turbine wake was explored for a case where the turbine pitched upwind and downwind in a uniform flow. Findings indicated that the wake of the floating turbine is susceptible to the floating conditions and the dynamics of the surrounding waves. Furthermore, results showed a stronger expansion of the wake and that vortices shed from the blade led to a rippled boundary layer in the upper wake.

Sebastian and Lackner [33] found current analysis methods based on blade element momentum theory did not capture the unsteady flow generated at the blades by strong variations in angle of attack. Large angle of attack changes were due to the additional motion of the floating platforms. These aerodynamic analysis methods use *ad hoc* formulations to cover the unsteadiness due to tip losses, high tip speed ratios and yawed flows. Motion induced unsteadiness violates assumptions of standard blade element momentum theory and will lead to incorrect predictions of unsteady aerodynamic loads. Spectral analysis of kinematic behavior of various types of floating platforms were performed and the pitch aerodynamics was found to dominate unsteady flow effects and structural loading. It was shown that pitching motions of the wind turbine cause the turbine to change from the windmill state, where the turbine extracts energy from the flow, and propeller state, where the turbine drops energy into the flow [34]. The state of the turbine can be determined by observing the bound vorticity of the blades, where high vorticity represents a windmill state and low, negative vorticity represents a propeller state. It was found that vorticity change follows pitch motions of the platform and the variation in bound vorticity will lead to varying loads and fatigue on the rotor.

Jonkman *et al.* performed simulations of fully coupled aero-hydro-servo-elastic responses of the floating platform concepts and compared the results in special cases with other simulation frequency-domain analysis methods to test their reliability [14]. None of the simulation results were validated against experimental data since no such data was freely available.

Wake measurements of offshore wind turbines were performed and compared with six different wake models [3]. The results showed a wide spread of predicted wake deficits.

The objective of this paper is to investigate the influence of pitch motion on the wake of a model wind turbine. Wake measurements have been performed in a wind

tunnel using stereoscopic particle image velocimetry (SPIV). The flow field, including mean and fluctuating components of the flow, are analyzed for a fixed *versus* an oscillating turbine under the same inflow. These results are then compared with existing wake models to observe their ability to capture such pitch motion effects.

2.2 Theory and models

Mean momentum and Kinetic Energy equations

For steady, incompressible and inviscid flows the Reynolds-averaged Navier-Stokes (RANS) equations are given by

$$U_j \frac{\partial U_i}{\partial x_j} = -\frac{1}{\rho}\frac{\partial P}{\partial x_i} - \frac{\partial \overline{u_i u_j}}{\partial x_j} - F_{x_i} \ , \tag{1}$$

where x_i is the coordinate in the streamwise, wall-normal or spanwise direction, x, y, z, respectively, and U_i is the velocity vector, represented by its components U, V, W in streamwise, wall-normal or spanwise (orthogonal to x and y) direction. The mean pressure is represented by P while u_i represents the fluctuating velocity component and ρ is the fluid density. The components of the thrust force of the wind turbine on the flow are represented by F_{x_i}. The overbar denotes time average. Unsteady and viscous terms are omitted here, as the flow is considered to be steady and far from solid boundaries, where the viscosity plays an important role [6, 7]. The momentum equation (26) yields a balance between the inertial terms, pressure gradient, Reynolds stress and the thrust force.

Multiplication of Eq. 26 by the mean velocity U_i results in the mean kinetic energy equation

$$U_j \frac{\partial \frac{1}{2}U_i^2}{\partial x_j} = -\frac{1}{\rho}U_i\frac{\partial P}{\partial x_i} + \overline{u_i u_j}\frac{\partial U_i}{\partial x_j} - \frac{\partial \overline{u_i u_j}U_i}{\partial x_j} - U_i F_{x_i} \ , \tag{2}$$

where the sum of $\frac{1}{2}U_i^2$ describes the mean kinetic energy in the flow. Eq. (27) shows that the convection of mean kinetic energy equals a sum of the mean pressure gradient in the flow, the production of mean kinetic energy, the gradient of the kinetic energy flux and power extracted by the wind turbine, respectively.

Several terms of the momentum equation (26) and the mechanical energy equation (27) will be analyzed and related to the extraction of power, as it has been found that their balance yields the power production [6, 7]. For further details on the derivation, see [6].

Wake models

Both the mean momentum equation (26) and the mean kinetic energy equation (27) contain the Reynolds stress tensor $\overline{u_i u_j}$. As a consequence of the dynamic equation that can be derived for this quantity, the Reynolds stress tensor is not fully determined by the averaged velocity U_i and pressure P alone [9]. In addition, information about the average over products of three velocity fluctuation components $\overline{u_i u_j u_k}$ in the Reynolds stress equation is needed, otherwise called the triple correlation. The fact that this problem repeats for all moments of the velocity fluctuation is the closure problem of turbulence. This issue is circumvented by the application of a turbulence model which imposes a closed expression for $\overline{u_i u_j}$ in terms of U_i, P and possibly additional variables. These additional variables are often governed by partial differential equations similar to Eq. (26) in that such equations balance convection with source, sink and stress terms.

Wake models that solve systems of partial differential equations are often summarised as field models. While the numerical solution of the continuity and momentum equations in three dimensions with a turbulence model and viscosity effects is obtained in computational fluid dynamics (CFD), also systems of reduced complexity are often considered. The model by Ainslie [1] is often employed, which imposes axial symmetry and an eddy viscosity model for turbulence closure. Consequently, this allows the formulation of a closed, two dimensional system of partial differential equations describing the far wake behind a single wind turbine.

Further simplified descriptions are given by analytical wake models. These follow from momentum balance considerations in a specific control volume, together with model-specific assumptions. One widely used example is the model by Jensen [13], which relies on the restriction to one velocity component and linear wake expansion. Often such models include parameters that are determined empirically. Note that if enough data is available, it is also possible to build wake models that are entirely empirical [26].

Herein, short summaries of the Jensen model, the Larsen model, the Ainslie model and a CFD actuator disk model are provided, before comparing the results to data obtained from wind tunnel experiments. The governing equations of the wake models can be found in Appendix 2.6.

For the calculation of the wake models, *flapFOAM* [31] is used. This follows a similar approach as the wind farm layout program FLaP [18], but is fully embedded into the framework of OpenFOAM [27], thus extending the modeling capabilities. The resulting velocity deficits were added to the measured inflow profile, which was extended for low and high vertical coordinates by fitting standard log-profiles,

$$U(y) = \frac{u_\star}{\kappa} \ln\left(\frac{y + y_0}{y_0}\right), \tag{3}$$

where y denotes the wall-normal coordinate, $\kappa = 0.41$ the Karman constant, $u_\star$ the friction velocity and y_0 the roughness length.

Jensen model The Jensen model wake is characterised by linear wake expansion as a function of the downstream distance from the rotor plane [13], with a proportionality constant usually chosen in the range of $k = 0.04 - 0.07$. Only the axial velocity deficit is modeled, with the magnitude obtained by momentum conservation. The deficit profile is hat-shaped in that it is constant in the radial direction within the wake and abruptly drops to zero at its boundary.

Larsen model The Larsen model [19] assumes an axisymmetric wake, reducing the RANS equations to two dimensions. For the Reynolds stresses, Prandtl's mixing length theory is used to model the eddy viscosity [36]. Model constants are determined empirically using measurements at $9.5D$ behind an isolated turbine. The wake radius is given as an explicit non-linear function of the downwind coordinate in this model. Descriptions of the horizontal and radial velocity components are given, which possess dependencies on the downstream and radial coordinates. The wake expansion and decay are determined by the thrust coefficient and the ambient turbulence intensity. The Larsen model has analytical solutions at first and second order with respect to an expansion in the axial velocity deficit.

Ainslie model Like the Larsen model, the Ainslie model [1] is based on the assumption of an axisymmetric wake. Viscous effects are taken into account using an eddy-viscosity model to obtain turbulence closure. Up to $2D$ downwind distance from the rotor the wake is prescribed using to a Gaussian profile, before it starts evolving according to the two coupled partial differential equations in the radial and downwind coordinates. Chosen parameters are the thrust coefficient and ambient turbulence, the latter entering the eddy viscosity components. The solutions for the axial and radial velocity components are obtained numerically on a two-dimensional grid.

Actuator disk rotor model Discretized versions of the RANS equations can be solved on a three-dimensional mesh with methods from computational fluid dynamics. The simplest representation of the rotor is the actuator disk approach with uniform

forcing [21]. For turbulence modeling, i.e. modeling the eddy viscosity to estimate Reynolds stresses, the $k - \varepsilon$ model with increased dissipation near the rotor is applied [10]. The inflow boundary condition for the velocity is described in Section 2.2. Likewise, the measured inflow profile for the turbulent kinetic energy TKE is extrapolated linearly for low and high vertical coordinates. The inflow turbulent dissipation ε could not be measured with sufficient accuracy, therefore it is interpolated using the Richards-Hoxey solution [30], which corresponds to the local log-profile approximation. In the simulations, all effects due to laboratory walls, apart from the ground, were ignored. The latter is represented by wall functions with roughness length $z_0 = 0.0046$ m.

2.3 Methods

Wind tunnel facility

The experiments were performed in the wind tunnel at Portland State University. The test section of this closed-circuit tunnel is 5 m in length with a height $\times$ width of 0.8 m x 1.2 m. The free stream velocity can be set between 2 m/s and 40 m/s with low turbulence intensity. Figure 34 shows a schematic view of the wind tunnel and setup used during the experiments. The inflow conditions were modified by a passive grid to generate a mean turbulence intensity level of 9%. Behind the grid vertical strakes made of plexiglas were placed, shaped in such way, that the velocity profile resembles atmospheric-like conditions. For more details on the wind tunnel see [11].

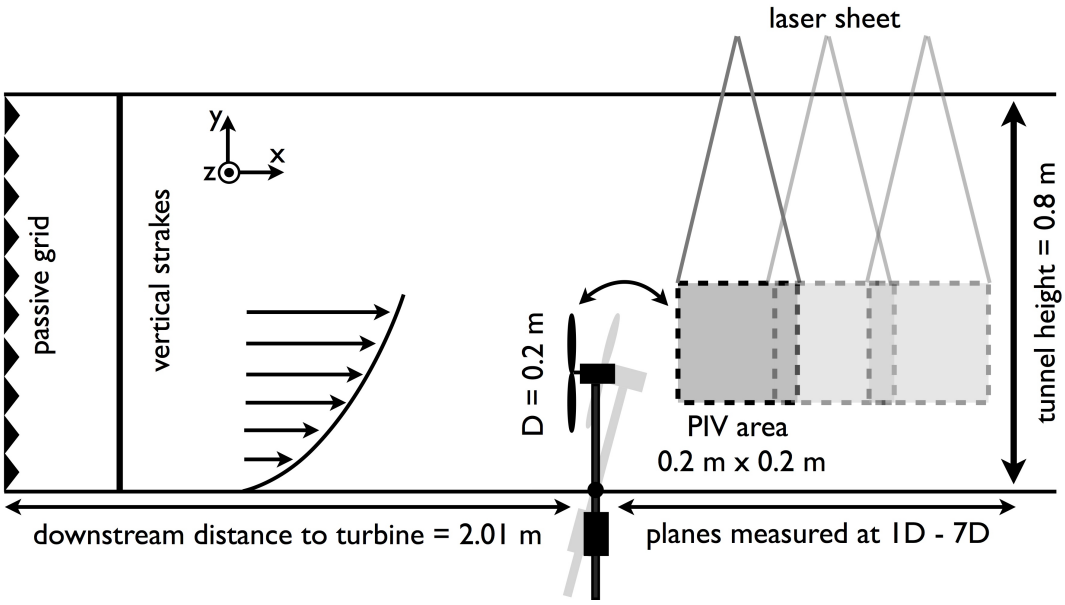

Abbildung 1: Wind tunnel setup. The scales are changed for visual clarification.

The hub height of the turbine was 25 cm. The wind tunnel speed was set to 6.05 m/s at hub height of the turbine and the model wind turbine was placed 2.01 m downstream of the passive grid.

Model wind turbine

The model wind turbine shown in Figure 2 is a 1:400 scale model of a typical horizontal axis wind turbine with a 80 m rotor diameter. The model turbine consists of an aluminum tower with a diameter of 16 mm and a nacelle with a diameter of 28 mm. The rotor has a diameter D of 200 mm and is produced with a rapid prototyping method. The blockage ratio of rotor area to wind tunnel cross-section is below 3.3% so blockage effects can be neglected [35]. The blades are designed using Blade Element Momentum theory to perform efficiently at low wind speeds and therefore at low Reynolds numbers. The design tip speed ratio λ is approximately 6 which corresponds to common tip speed ratios of full scale turbines. The blades had a twist of 31° from root to tip and a pitch angle of 6° set at blade tip with respect to rotor plane. The hub height of the turbine is at $1.25D$ from the floor of the test section. Inside of the nacelle, a small DC motor (*Faulhaber 1331T006SR*) is mounted, which is operated as a generator. The power output of the turbine was measured mechanically, therefore the tuorque T is measured by a sensor based on strain gauges with a design following the concept of the torque sensor of Kang *et al.* [17]. The rotational frequency ω is given by a magnetic encoder which is attached to the motor

(*Faulhaber IE2-400*). The output of the encoder are 400 pulses per revolution. The measurements are performed using a National Instruments A/D converter of model *NI USB 6211* and an in-house software written in *LabView*. The turbine was loaded by resistors to operate at its highest efficiency. The turbine is mounted in an gimbal support which allows oscillations in streamwise direction. The turbine is stabilized by a cylindrical weight of 650 g below the gimbal. The pitch motion was characterized using video analysis. The analysis consisted of 300 s video recorded at 30 Hz of the floating turbine. The nacelle of the turbine was marked with a dot of high contrast and a video tracking tool was used to create a time series of the nacelle movement. The resulting mean pitch angle for the floating case is 17.6° with a standard deviation of 0.4°. The range of oscillations was between 16° and 19°. A Fourier transformation of the time series indicates that the dominant frequencies of the oscillation are in the range of 1.2 – 1.8 Hz. A range for the frequency has to be given since the oscillations of the turbine are not controlled and are induced by the inflow of the turbine. In part due to the lower rotor frontal area in the inclined turbine position, the power coefficient, c_p, in the floating case was 0.26 whereas a higher c_p of 0.29 was observed for the fixed case. Thrust coefficients, c_T, were estimated from the induction factor and found to be 0.89 and 0.85 for the fixed and floating cases, respectively. Induction factors were, in turn, calculated from the corresponding power coefficients [4]. Motion of the model was restricted to one-dimensional pitching oscillations, which is indeed the dominant motion in real conditions. Therefore, it is recognized that some aspects of the wake may differ to that of full-scale as sway and heave are not considered. Furthermore, in studies capturing the structural response of floating bodies to wave excitations as in offshore structures, the Froude number is taken into consideration [31]. In this study, given that the movement of the mast is restricted to pitch, Froude number is not considered. Scaled parameters for the model wind turbine that are taken into account are the tip speed ratio, thrust and power coefficient. The gimbal can be blocked at a straight position, so the turbine is operated as classic non floating turbine and the performance of the turbine and surrounding flow conditions can be compared between fixed and floating with minor changes in the setup. Measurements were taken first for the fixed case, followed directly by measurements for the floating case.

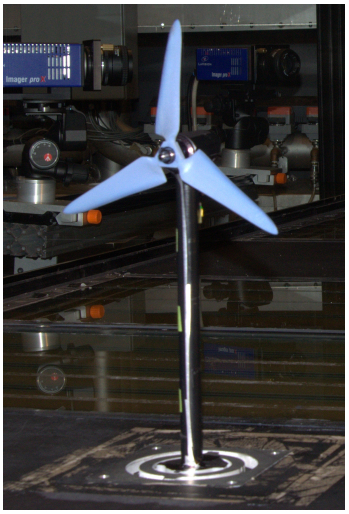

Abbildung 2: Wind turbine model with gimbal support. The gimbal is blocked for fixed case measurements. Scale 1:400, with $D = 0.2\,\mathrm{m}$. Power coefficient $c_p = 0.29$ for fixed case and 0.26 for floating case. Tip speed ratio $\lambda \approx 6$. Thrust coefficient $c_T \approx 0.89$ for the fixed and 0.85 for the floating case. Black coverage is to avoid laser beam reflections.

Stereoscopic Particle Image Velocimetry

The Stereoscopic Particle Image Velocimetry (SPIV) setup consisted of a *LaVision* system with a Nd:YAG (532 nm, 1200 mJ, 4 ns duration) double pulsed laser and two 2k x 2k pixel CCD cameras. The time delay between exposures of the cameras was 150 μs. The seeding fluid was neutrally buoyant in air atomized diethylhexyl sebecate. To allow consistent resolution, the seeding density was kept constant during the measurements and seeding particles were well mixed within the wind tunnel. The thickness of the laser sheet was approximately 1 mm throughout the measurement plane. Before each experiment, the cameras were calibrated using a standard *LaVision* two-plane measurement plate with known geometries which are recognized by the *DaVis* measurement software. The resulting measurement plane was approximately 0.2 m $\times$ 0.2 m with a vector resolution of approximately 1.5 mm. To estimate the vector fields from the raw images a multi-pass FFT based correlation algorithm was used. Interrogation windows of 64 $\times$ 64 pixels was used twice and a 32 $\times$ 32 window was used once, each with an overlap of 50%.

The freestream inflow conditions without the turbine present were measured using SPIV $1.5D$ to $0.5D$ upstream of the turbine position at a height of -$0.5D$ to $0.4D$ with $0D$ being hub height. For the wake measurements, the SPIV data was collected directly downstream of the centerline of the turbine. The height of the planes was

positioned from -0.25D to 0.75D, so the averaged development of blade tip vortices was captured. The planes were taken at distances of 0.7D, 1.6D, 2.5D, 4.3D and 6D. The first three planes were obtained with an overlap of approximately 0.1D to ensure a continuous plane throughout the near wake. SPIV allows for measurements of three velocity components in a 2 dimensional plane, where U is streamwise wind speed in the x direction, V the wall normal wind speed in the y direction and W is the spanwise wind speed in the z direction, as denoted in Figure 34.

For each measurement plane, 2500 samples were taken for fixed and floating case. A convergence test was carried out by calculating ensemble averages of 500, 1500 and 2500 samples. The results between 1500 and 2500 samples match very well so statistical convergence of means and higher order moments is assured. Spurious vectors were excluded from statistical calculation using a normalized median test according to [40]. For all planes, the percentage of spurious vectors for U and V were below 1% and below 1.2% for W.

This work compares the wake development of the fixed case and the floating case. The fixed case represents the wake of a classical bottom-fixed turbine. The floating case represents the same turbine which has the freedom to incline in streamwise direction (pitch motion). Due to the mean inflow velocity and its fluctuations, the turbine pitches downstream and oscillates, as described earlier in this work. Therefore, only the influence of dynamic pitch on the wake is discussed.

For the fixed turbine, the sampling frequency for the SPIV system of 1 Hz was used. In the floating case, the image acquisition was triggered to a fixed amplitude of oscillations in downstream direction to ensure the same influence of the oscillation on wake structures for each image. Therefore, a reflective strip was placed on the tower of the oscillating turbine. A *Monarch* optical tracker was positioned in such way, that every time the turbine reached a fixed pitch angle the SPIV system was triggered for data collection. The angle was chosen to be close to maximum pitch angle ($\sim 18.5°$).

2.4 Results

Measurements of the flow field obtained via SPIV for the fixed and floating turbine cases are compared. Contour plots are presented pairwise where the upper plot (a) shows results of the fixed turbine and the lower plot (b) results of the floating turbine. The planes from 0.6D to 3.3D were taken with an geometrical overlap so the results of these planes are merged using a linear weight function. Thereafter, average profiles for the mean velocity, Reynolds stresses and terms in the mean kinetic energy equation are analyzed. Profile plots, which represent intersections of the wake at different

downstream distances, will be presented to emphasize the quantitative differences in the development of the wake.

Mean flow

Figure 3 shows contour plots of the averaged streamwise velocity component U normalized by the inflow wind speed at hub height $U_{hh} = 6\,\mathrm{m/s}$. The velocity ranges are similar in both cases. In Figure 3a, U/U_{hh} behind the fixed turbine is plotted for a range encompassing both the near and far wake. Similarly, this is done in figure 3b for the floating turbine, where the SPIV system is locked to a fixed pitch angle of the turbine. This angle represents a strong downstream pitching of the turbine due to its oscillations.

Figure 3a shows the wake of the fixed turbine which has the typical shape of a wake of a classical horizontal axis wind turbine [8,38]. The shape of the deficit is symmetric around hub height. From -0.2D to 0.25D in the y/D dimension, a strong velocity deficit ($\sim$ 30% of U_{hh}) is observed due to the blockage of the nacelle. The deficit is pronounced mainly up to 3D and recovers up to 75% of U_{hh} at 7D downstream. These results correspond to the findings of Chamorro *et al.* for a single turbine in an neutral boundary layer [8].

Figure 3b shows that, for the floating case, the the deficit is no longer symmetric about the hub height in the wall normal direction, y/D.. This is in direct contrast with the symmetry observed in the fixed case. The deficit is shifted down by 0.1D, due to the pitch angle of the turbine. The area with the strongest deficit (below $0.5\,U_{hh}$) is by 25% smaller in the floating case compared to the fixed case. The wake pattern of the floating turbine is skewed upward by approximately 3° due to the pitch motion of the turbine. Similar wake deflections, due to non-axial momentum extraction of the turbine, were observed for turbines in yaw conditions, but in the spanwise direction [24, 28]. The flow pattern in the shear layer above blade tip is more compact in the floating case than in the fixed case. At 6.5-7D downstream, the low speed area (blue/green) is shifted up by approximately 0.25D towards the top tip. In addition Fig. 3b shows, due to the overall upward shift of the wake, that the mean streamwise wind speed between the hub height and blade tip is 10% lower with $0.7\,U_{hh}$ in the floating case by 6.5-7D.

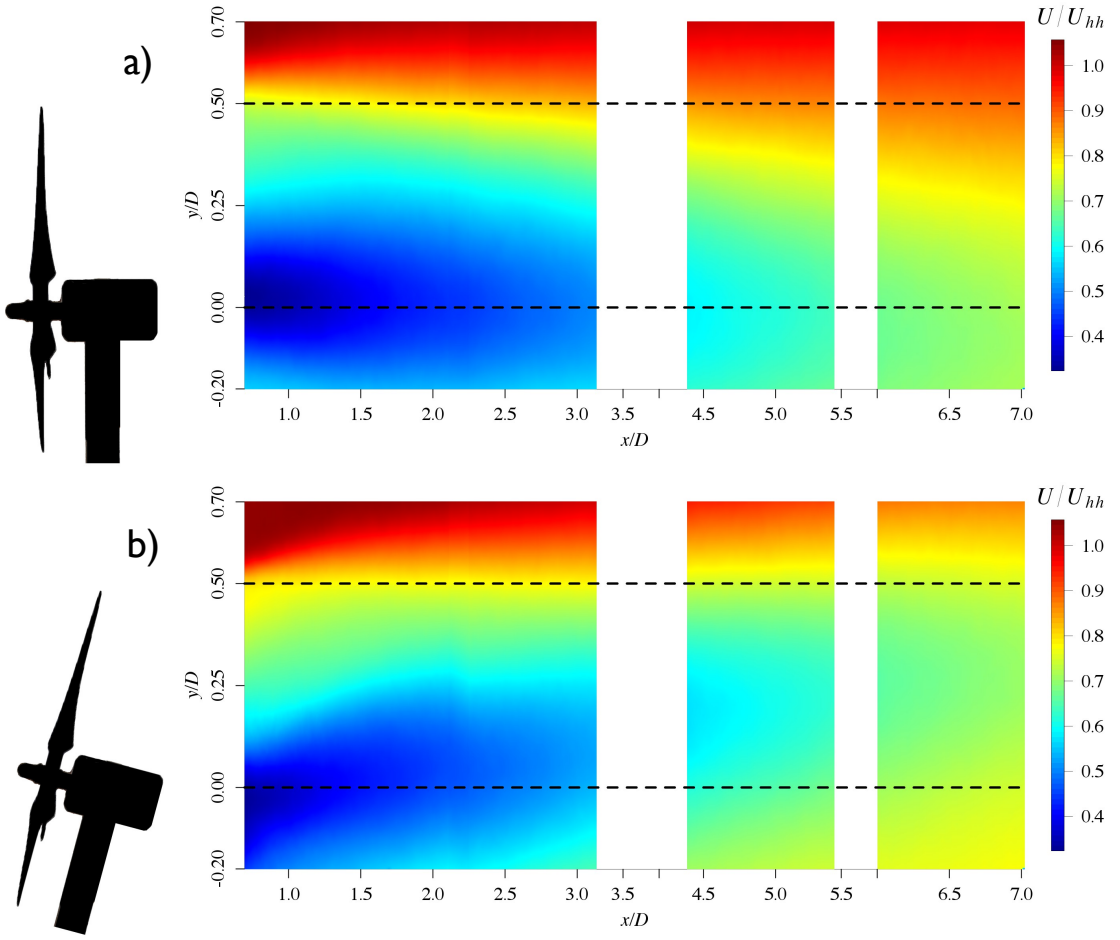

Abbildung 3: Normalized streamwise velocity component U/U_{hh} of the wake for fixed and floating cases. U/U_{hh} in the fixed case has a typical symmetric shape around hub height. In the floating case it has a pronounced upwards trend with increasing x/D. Hub height ($y/D = 0$) and top blade tip ($y/D = 0.5$) are indicated by dashed horizontal lines.

Figure 4 provides vertical profiles of U/U_{hh} at downstream distances x/D of $0.75D$, $1.5D$ and $3D$ for both the fixed and floating cases in order to allow a more detailed comparison. A logarithmic fit to the inflow profile is added to visualize the effect of the turbines on the flow. The fit extends the measured inflow profile to $y/D =$ 0.7, since the measurement plane for the inflow was set to y/D -0.5D to 0.5D. At x/D of $0.75D$, the shift of the deficit in the floating case is very pronounced. At x/D of $1.5D$, the profiles for both cases have similar shapes, but the wind speed is lower in the fixed case. At x/D of $3D$, a strong upwards shift by $0.1D$ in the y/D dimension is observed in the profile for the fixed case. In addition, the deficit is again weaker in the floating case than the fixed case. Comparing the fixed and floating cases, two main differences exist in the location of the inflection points and profile

crossings near the top tip. First, the inflection point and crossings near the top tip are shifted vertically away from the tunnel floor for the fixed case with profile crossings located at $y/D = 0.57D$ for the fixed case and at $y/D = 0.55D$ for the floating case. Second, the magnitude of the deficit at which the profile crossing is located is smaller in the fixed case. The profiles for the fixed turbine tend to intersect at the lowest point whereas this does not occur for the floating turbine. This is attributed to the movement induced via the pitch motion of the turbine.

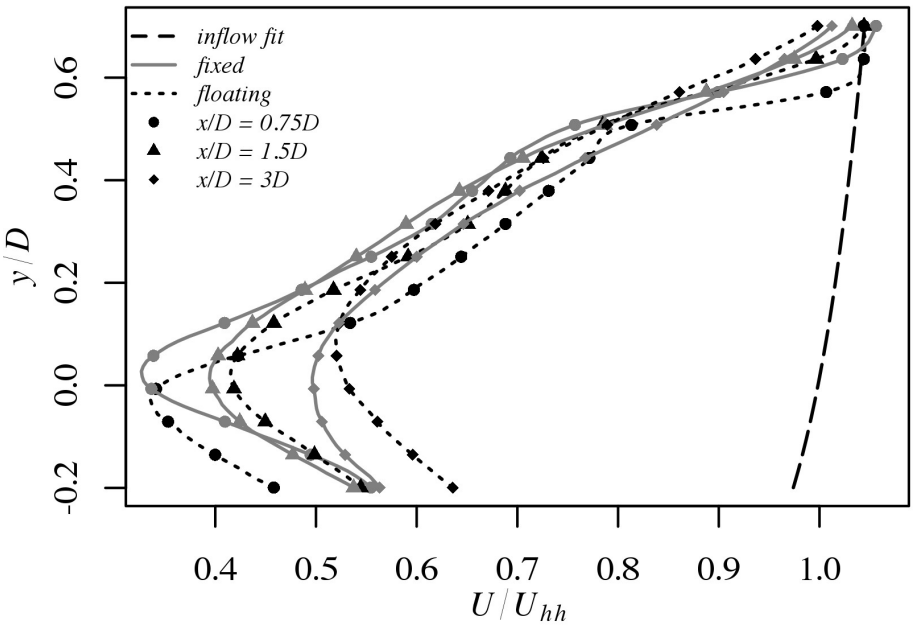

Abbildung 4: Profile of a logarithmic fit to inflow and near wake profiles of U/U_{hh} for fixed and floating case at downstream distances $0.75D$, $1.5D$ and $3D$.

Figure 5 shows profiles at 4.5D, 6.1D and 7D downstream positions. The streamwise velocity component at blade tip height and above is smaller by 5-15% for the fixed and by 10-25% for the floating case as compared with U_{hh}, which is due the mast of the turbine being rigid and, consequently, further enhances mixing and recovery particularly in the shear layer of the wake. In the fixed case, the flow is recovering at hub height gradually, but has not fully recovered by $5D$-$7D$, which compares well to [8, 41]. The profiles of the floating case are shifted up by 0.2-0.3D. In order to quantify the differences between the fixed and floating cases, the resultant thrust force ($thrustforce \sim U^2$) from y/D = -0.2D to 0.5D was calculated. In the floating case, the thrust force on a downwind turbine is reduced 9-10% compared to the fixed case. Also, the available power at downstream distances $x/D = 4.5D$, $6.1D$ and $7D$

is compared, by integrating the cubed velocity profiles from y/D = -0.2D to 0.5D. The available power to be extracted in the floating case is 14 - 16% lower compared to the fixed case.

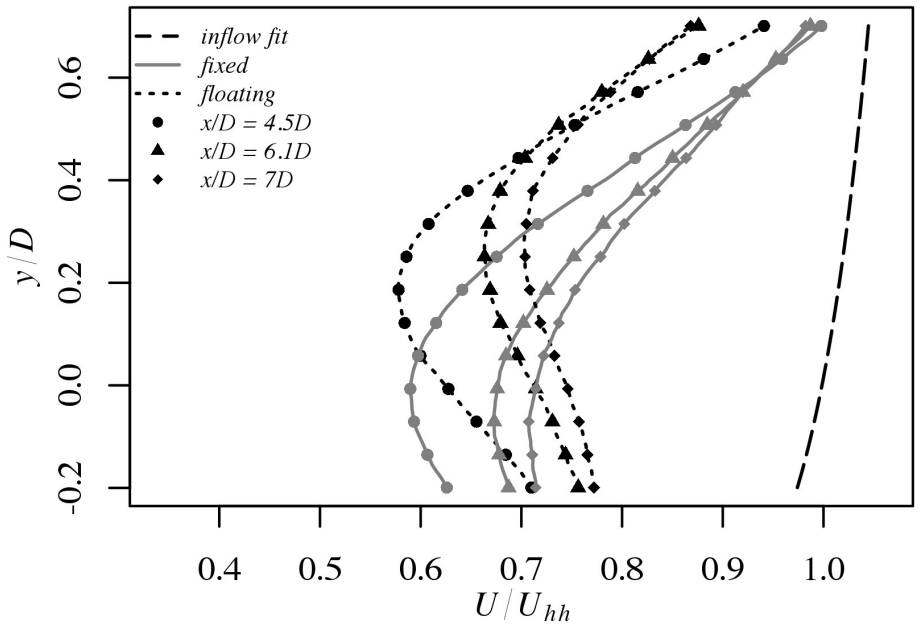

Abbildung 5: Profile of a logarithmic fit to inflow and far wake profiles of U/U_{hh} for fixed and floating case at downstream distances 4.5D, 6.1D and 7D.

Figure 6 presents contours of mean wall normal velocity V/U_{hh} for both cases. In the fixed case (Fig. 6a), the average wind speed hovers around 0 m/s, except directly behind the nacelle at hub height and below, where an area with -0.04 U_{hh} is present, thus entraining fluid downwards on the downstream range of 1-3D. As expected, the flow becomes increasingly homogeneous as x/D increases.

In the floating case (Fig. 6b), the average wall normal velocity of the whole field is 0.035 U_{hh}. A small enclosed deficit area behind the nacelle with negative wind speed is present up to 1D downstream. A positive wind speed up to 0.08 U_{hh} is shown from y/D = 0.25 and upwards toward the blade top-tip. With increasing downstream distance, the wall normal velocity increases to an average of 0.04 U_{hh} in the region from 6.1D to 7D. Notably, a wall normal velocity of 0.04 U_{hh} for the floating case represents 980% of V/U_{hh} for the same location in the fixed case.

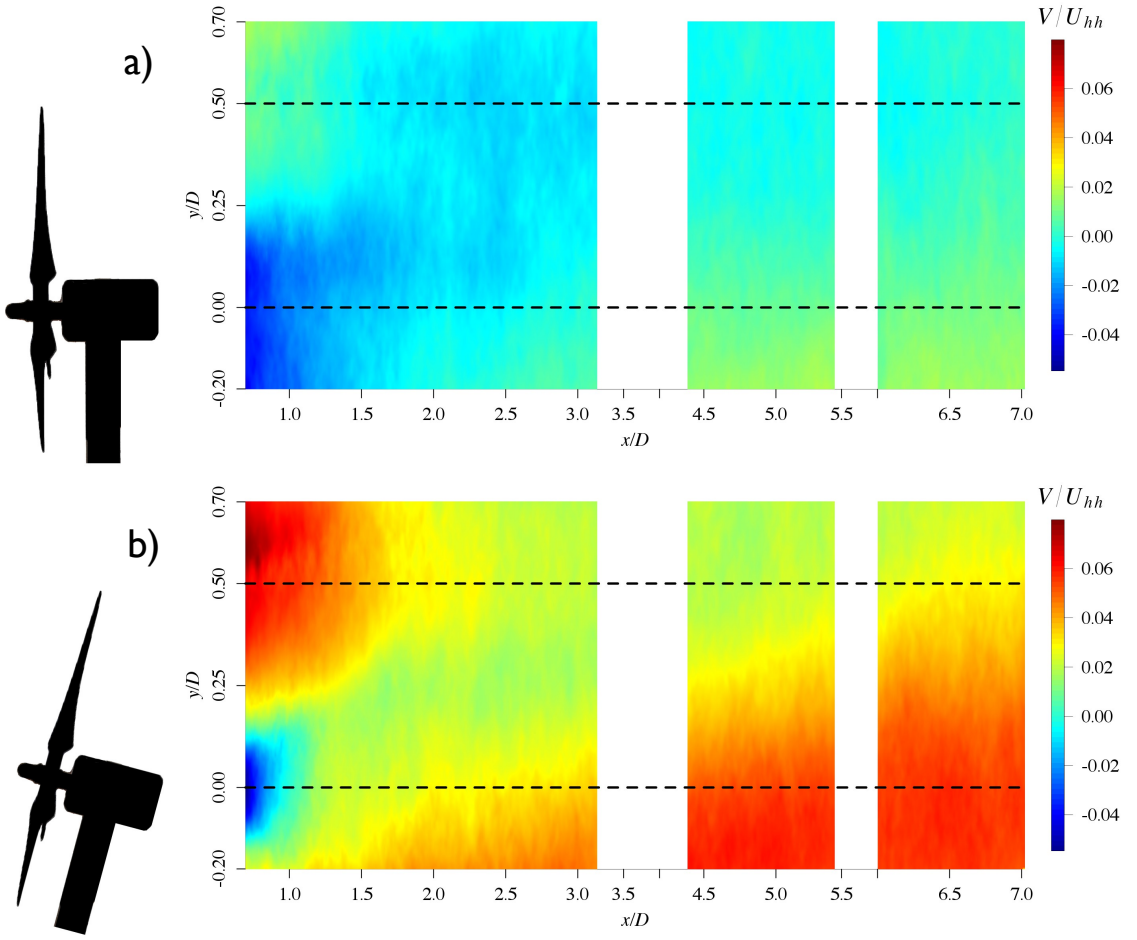

Abbildung 6: Normalized wall normal velocity component V/U_{hh} of the wake for fixed and floating cases. In the fixed case, V/U_{hh} is close to zero. In the floating case, V/U_{hh} increases with increasing x/D. Hub height ($y/D = 0$) and top blade tip ($y/D = 0.5$) are indicated by dashed horizontal lines.

Profiles of V/U_{hh} at downstream distances x/D of $0.75D$, $1.5D$ and $3D$ are shown in Figure 7 for both cases. Above hub height, the profile shapes at x/D of 0.75D are similar for the two cases but the absolute velocities are much higher for the floating case. A well defined area of reversed flow behind the nacelle at hub height is evident in the wall normal velocity profile at $x/D = 0.75D$ for the floating case. In contrast, the area of reversed flow in the corresponding location is more diffused in the fixed case. A faster recovery is observed in the floating case than the fixed case.

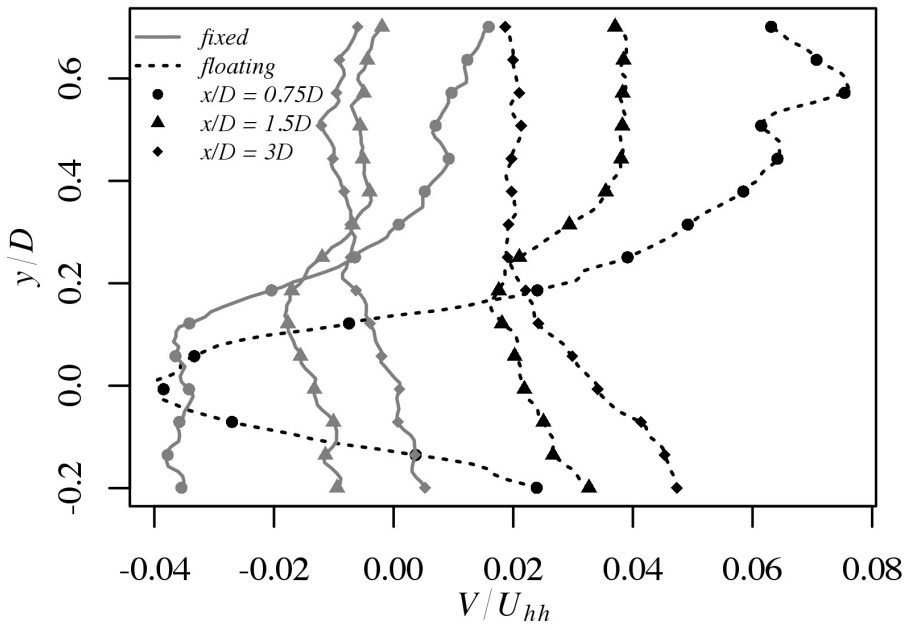

Abbildung 7: Near wake profiles of V/U_{hh} for fixed and floating cases at downstream distances $0.75D$, $1.5D$ and $3D$.

Figure 8 presents far wake profiles for the wall normal velocity component at x/D of $4.5D$, $6.1D$ and $7D$ downstream. For the fixed case, not only are the trends in the velocity profiles at all three streamwise positions similar, but the absolute velocities observed are comparable. As observed in the wall normal velocity contour plots, the overall velocity is increased in the floating case.

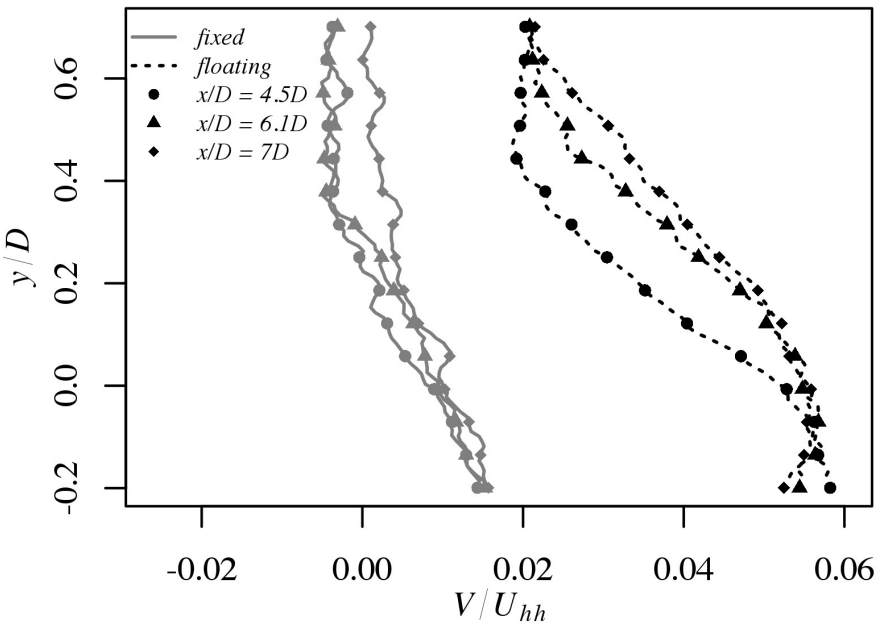

Abbildung 8: Far wake profiles of V/U_{hh} for fixed and floating cases at downstream distances $4.5D$, $6.1D$ and $7D$.

Figure 9 presents contours of the mean spanwise velocity W/U_{hh}. The velocity ranges of both contours are comparable in magnitude although the shape of the contours differ from one another. In both cases, there is a clear visible divide between positive and negative spanwise velocity at hub height, which is due to the clockwise rotation of the blades. In the floating case, this point is shifted upwards by $0.03D$ due to the inclined turbine as a consequence of the oscillatory motion of the mast. In the fixed case, the area with negative velocity is cone-shaped and extends to $3D$ downstream of the rotor. In the fixed case, the line dividing areas of positive and negative velocities is roughly horizontal while the line dividing positive and negative velocities shows a positive slope with increasing downstream distance in the floating case.

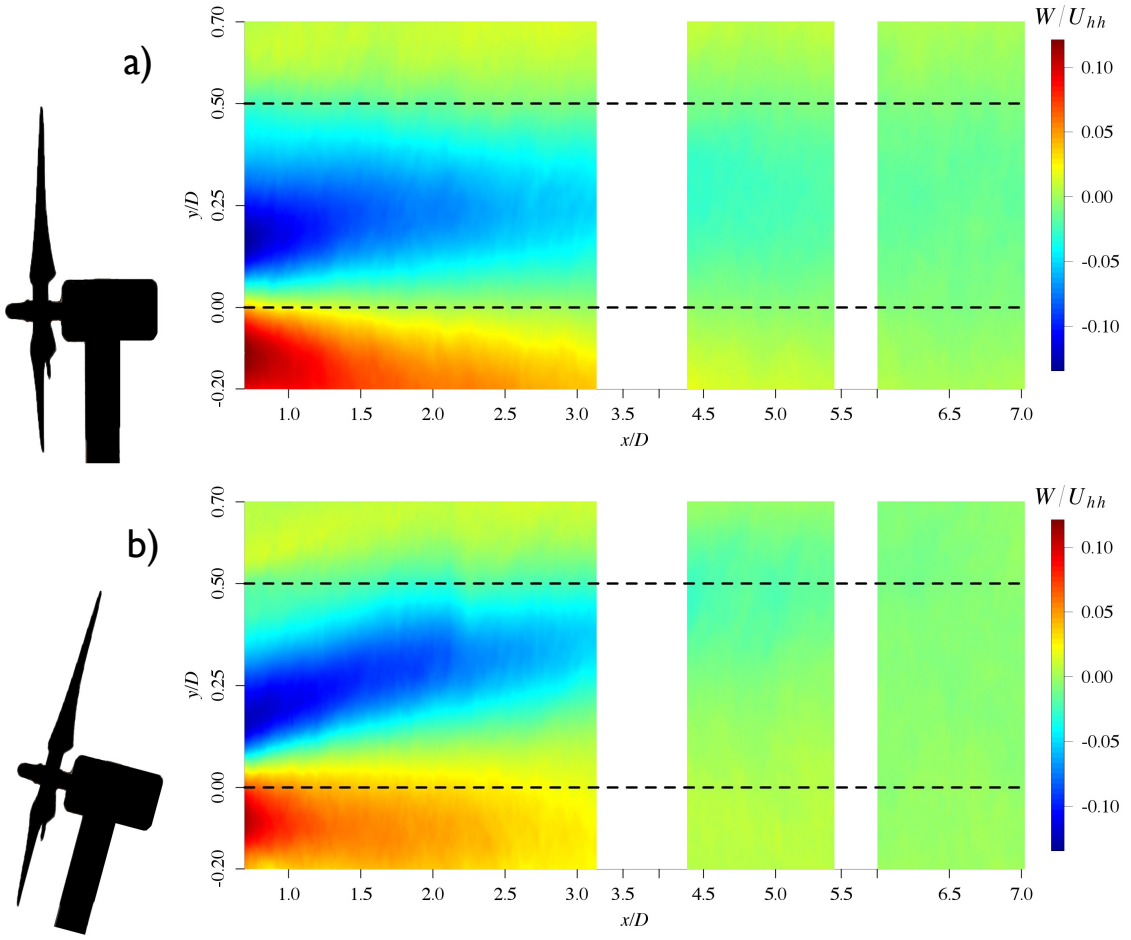

Abbildung 9: Normalized spanwise velocity component W/U_{hh} of the wake for fixed and floating cases. In the fixed case, W/U_{hh} has a symmetric divide of positive and negative velocities. In the floating case, the negative shape moves upwards with increasing x/D, while the shape of contours of positive velocity stays at a constant height. Hub height ($y/D = 0$) and top blade tip ($y/D = 0.5$) are indicated by dashed horizontal lines.

Near wake profiles of spanwise velocity are presented in Figure 10. The profiles at $x/D = 0.75D$ have a similar shape for both cases, but the profiles develop differently with increasing distance. At $x/D = 1.5D$ and $3D$, the shift of the peak negative speed in the floating case to higher wall normal position becomes evident. At $1.5D$, the velocity magnitudes are shifted towards negative speeds in the floating case. The shape of the fixed profiles is symmetric, while the profiles in the floating case smear out with distance due to the oscillation of the turbine.

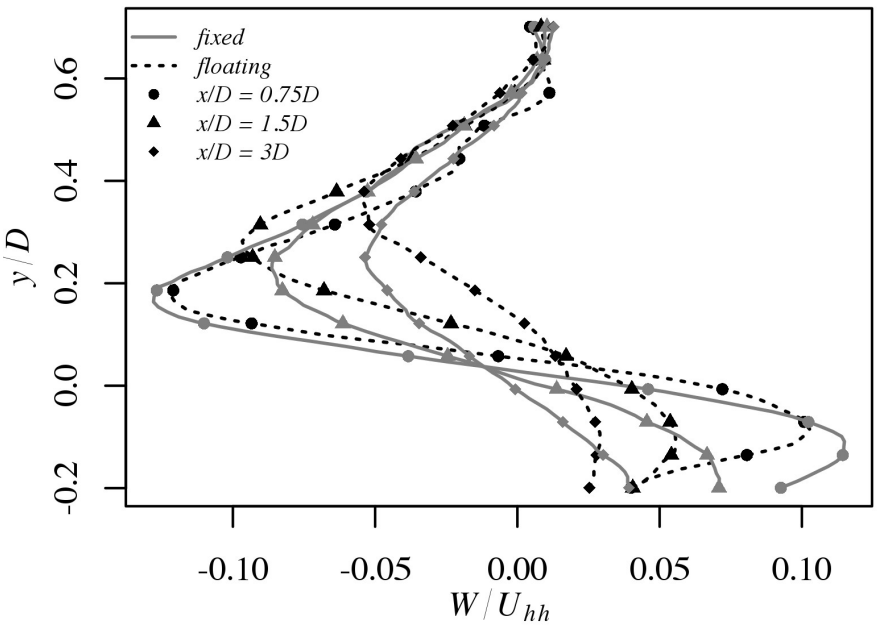

Abbildung 10: Near wake profiles of W/U_{hh} for fixed and floating cases at downstream distances $0.75D$, $1.5D$ and $3D$.

Figure 11 shows the far wake profiles of W/U_{hh}. The minimum spanwise velocity occurs at $4.5D$ in the wall normal dimension for the fixed case whereas the minimum is shifted upward $0.2D$ in the wall normal dimension for the floating case. At $x/D =$ 6-7D, the flow in the floating case is homogeneous and closer to zero, whereas in the fixed case the flow is negative from hub height to the tip of the blades and positive below hub height and above the tip. Such observations at $x/D =$ 6-7D suggest that the flow shedding due to the rotation of the blades is persisting further downstream in the fixed case even at $7D$ downstream.

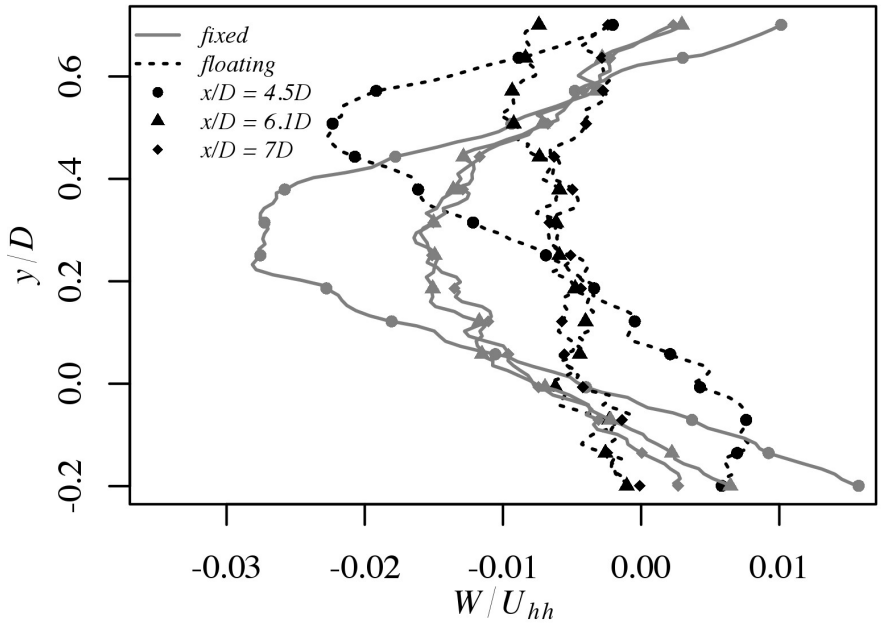

Abbildung 11: Far wake profiles of W/U_{hh} for fixed and floating cases at downstream distances $4.5D$, $6.1D$ and $7D$.

Reynolds stresses and flux of mean kinetic energy

Figure 12 shows the contours of the normalized normal component $\overline{uu}/U_{hh}^2$ of the Reynolds stress tensor. Overall, the average stress over the measurement area is 8% smaller in the floating case compared to the fixed case. In the fixed case, the largest magnitude of $\overline{uu}/U_{hh}^2$ is produced in the shear layer above the top tip. Directly behind the hub at hub height, roughly "v-shaped"regions with elevated magnitudes of $\overline{uu}/U_{hh}^2$ are evident for both cases. However, smaller magnitudes of the Reynolds stress are found in the "v-shaped"region in the fixed case. Furthermore, in the non-moving turbine, these features diminish after $x/D = 1.5$-$2D$. In the case for the oscillating turbine, the presence of a higher stress behind and above hub height is advected towards the shear layer and at this wall-normal location with a downstream distance of $x/D \approx 3$, it merges. In the near wake of the floating case, the magnitudes of $\overline{uu}/U_{hh}^2$ in the shear layer as well as behind the hub are comparable.

Above the top tip, $\overline{uu}/U_{hh}^2$ in the shear layer is 20% higher in the fixed case for downstream distances up to $x/D \approx 3.1D$ and in the far wake the stress in the upper segment ($y/D > 0.5$) is 26% higher in the floating case. The maximum amplitude of $\overline{uu}/U_{hh}^2 = 0.023$ is at $y/D \approx 0.57D$ in the fixed case. In the floating case, the peak above top tip is lower with $\overline{uu}/U_{hh}^2 = 0.019$ at $y/D \approx 0.54D$ whereas the peak below

hub height is the highest streamwise Reynolds normal stress with $\overline{uu}/U_{hh}^2 = 0.025$ at $y/D \approx$ -0.18D.

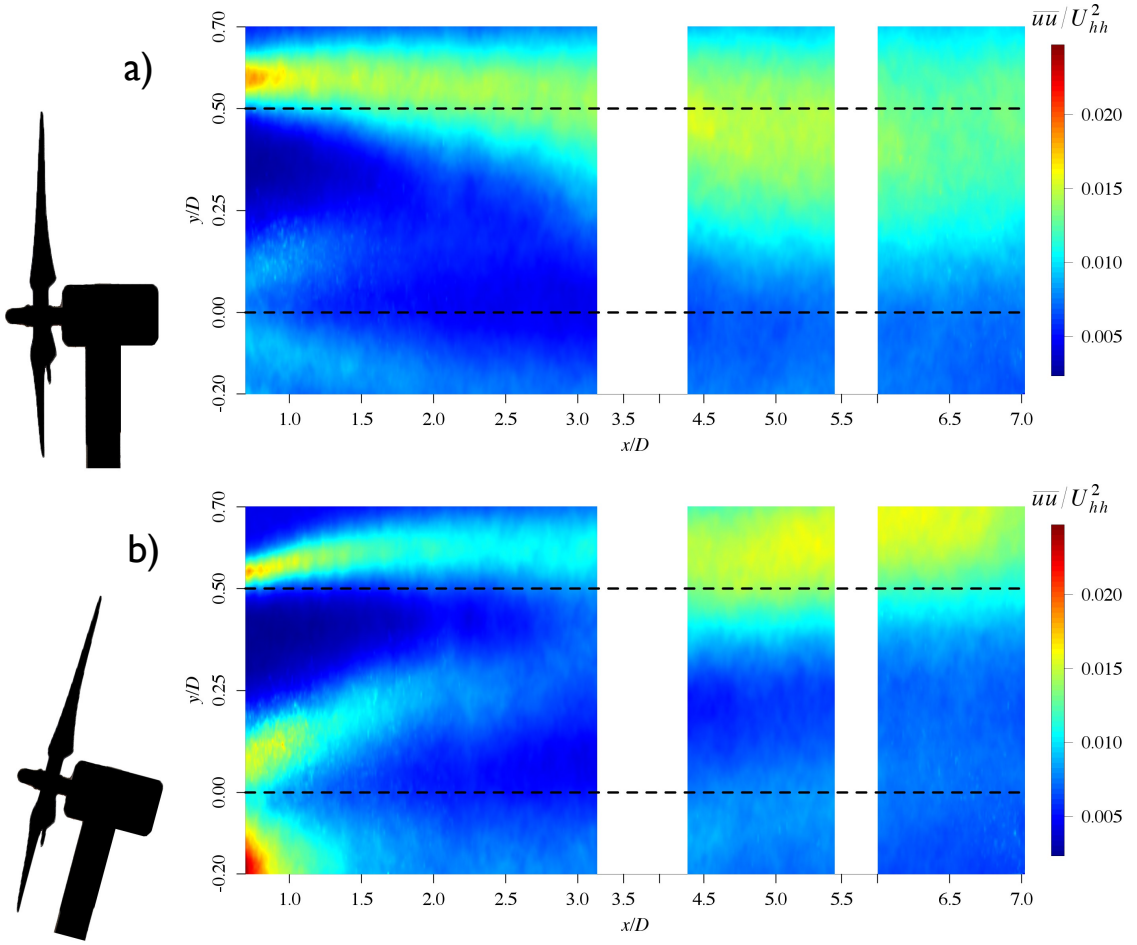

Abbildung 12: Contour of the normalized $\overline{uu}/U_{hh}^2$ Reynolds stress term for the fixed and floating cases. In the fixed case, most of the stress is created above blade tip and extends downward with increasing x/D. In the floating case, high $\overline{uu}/U_{hh}^2$ is created behind the hub and above tip top. Hub height ($y/D = 0$) and top blade tip ($y/D = 0.5$) are indicated by dashed horizontal lines.

In Figure 13, the Reynolds shear stress, $\overline{uv}/U_{hh}^2$, is presented, which indicates momentum transport. The development of $\overline{uv}/U_{hh}^2$ is of high interest as it is responsible for the energy being extracted from the turbine [6]. In both cases, the ranges of turbulent shear stress are close in magnitudes. The range and shape of the contours in the fixed case is comparable to the results found by Chamorro *et al.* [8]. A large negative turbulent stress above hub height and a positive turbulent stress below hub height is present, which is attributed to mixing effects of the wake.

In the fixed case, positive $\overline{uv}/U_{hh}^2$ is mostly present below hub height. In the floating case, the oscillations of the turbine cause a stronger positive shear stress in the far wake. Positive shear stress becomes less significant in the far wake region, $x/D \approx 6.1D$-$7D$, in the fixed case. In the floating case, positive shear stress dominates in this same far wake region. Furthermore, the Reynolds shear stress tends to remain below hub height and constant with x/D in terms of magnitude for the fixed case whereas in the floating turbine the features tend to shift upwards. The pitch motion of the turbine causes a higher variation of the shear stress in the floating case, therefore stronger changes in the momentum flux are observed.

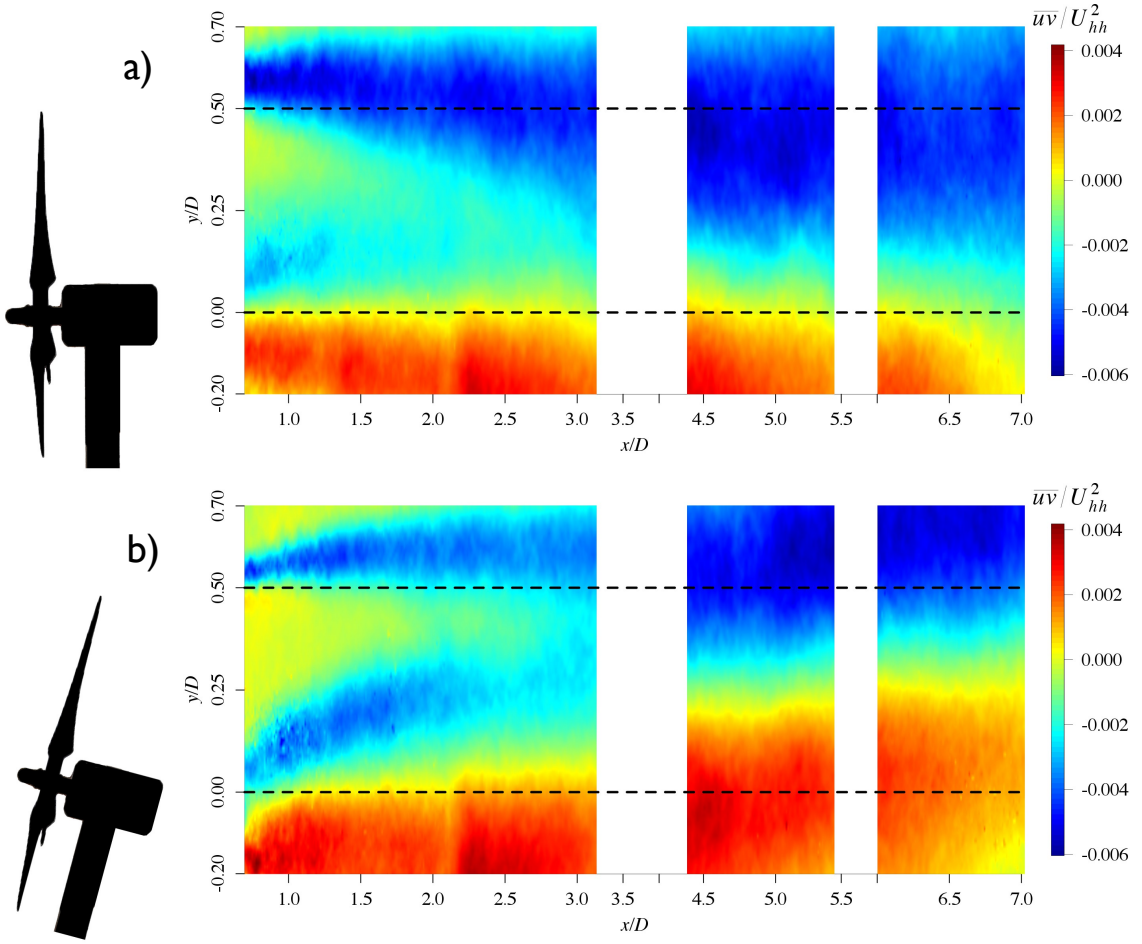

Abbildung 13: Contours of Reynolds shear stress $\overline{uv}/U_{hh}^2$ for the fixed and floating cases. Hub height ($y/D = 0$) and top blade tip ($y/D = 0.5$) are indicated by dashed horizontal lines.

Figure 14 shows the near wake profiles of the Reynolds shear stress $\overline{uv}/U_{hh}^2$. For the fixed case, the profiles cross just above the hub height whereas in the floating case they tend to monotonically increase with downstream position. Right behind

the rotor ($x/D = 0.75$), the Reynolds shear stress magnitudes are also greater for the fixed turbine.

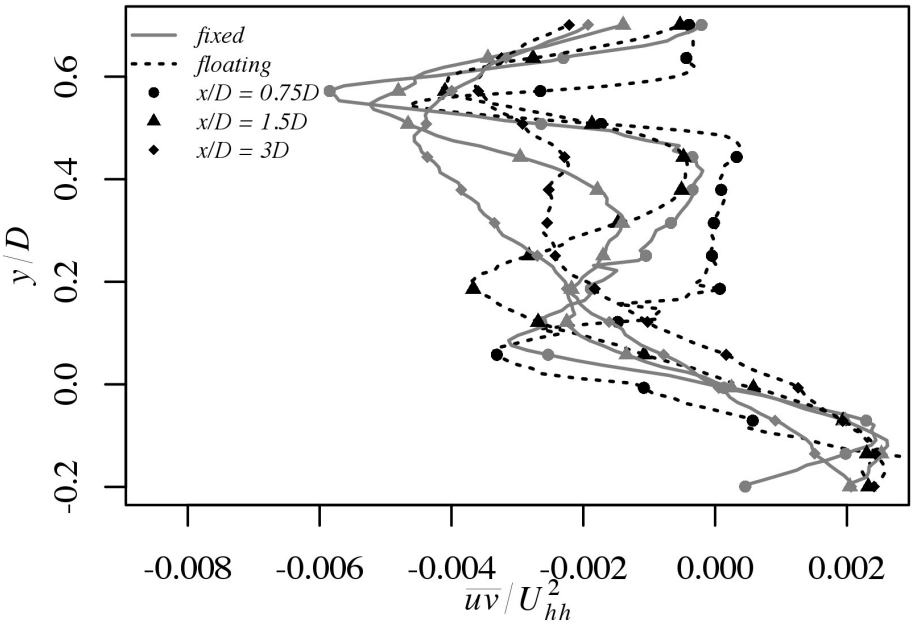

Abbildung 14: Near wake profiles of $\overline{uv}/U_{hh}^2$ for fixed and floating cases at downstream distances $0.75D$, $1.5D$ and $3D$.

Figure 15 shows far wake profiles of $\overline{uv}/U_{hh}^2$ for fixed and floating cases. Although the shapes of the profiles for both case evolve similarly with increasing distance downstream, there is a systematic upward shift in the profiles for the floating case. The negative peaks of the stress at $6.1D$ and $7D$ are similar in magnitude in both cases.

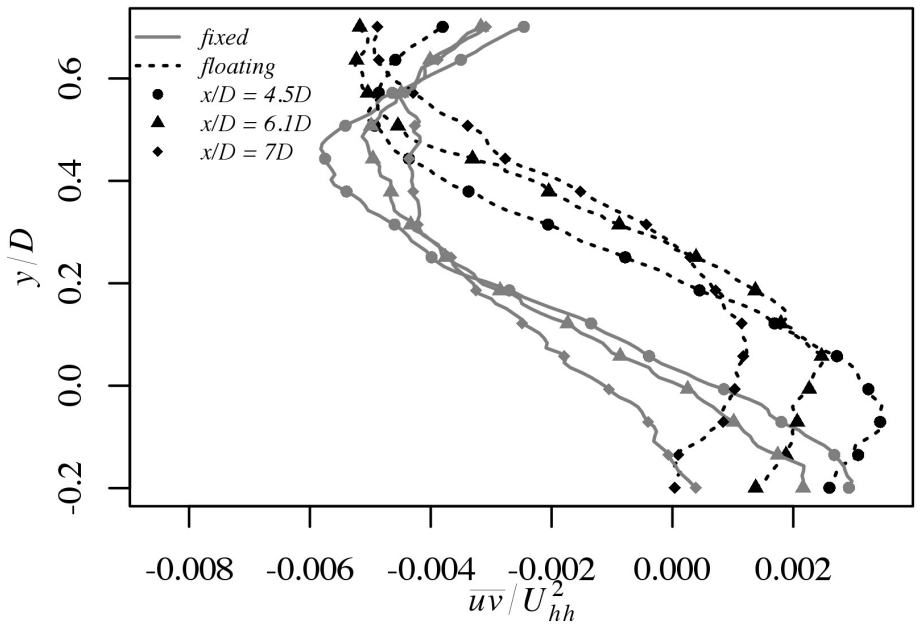

Abbildung 15: Far wake profiles of $\overline{uv}/U_{hh}^2$ for fixed and floating cases at downstream distances $4.5D$, $6.1D$ and $7D$.

Figure 16 shows the contours of turbulent kinetic energy (TKE), which shapes develop similar to the normal stress component $\overline{uu}/U_{hh}^2$ in Figure 12. This quantity is important since for the first turbine, the convective terms in the turbulent kinetic energy equation are significant. For both cases, turbulent kinetic energy is high above top tip and and behind the hub. The maximum magnitudes in the floating case are higher, especially behind the hub, where TKE has its maximum with 1.4 m^2/s^2, while for the fixed case, the highest TKE is in the shear layer with 0.7 m^2/s^2. For the fixed case, the turbulent kinetic energy from above tip top spreads and moves downward with increasing x/D with decaying magnitude in the near wake and an increase from $4.5 < x/D < 5.5$. In the floating case, the magnitude of TKE behind the hub decreases quickly with increasing downstream distance x/D = 0.7 - 2.2. The TKE above hub height spreads slightly with increasing x/D, but the structure remains close to the top tip height and moves upwards in the far wake.

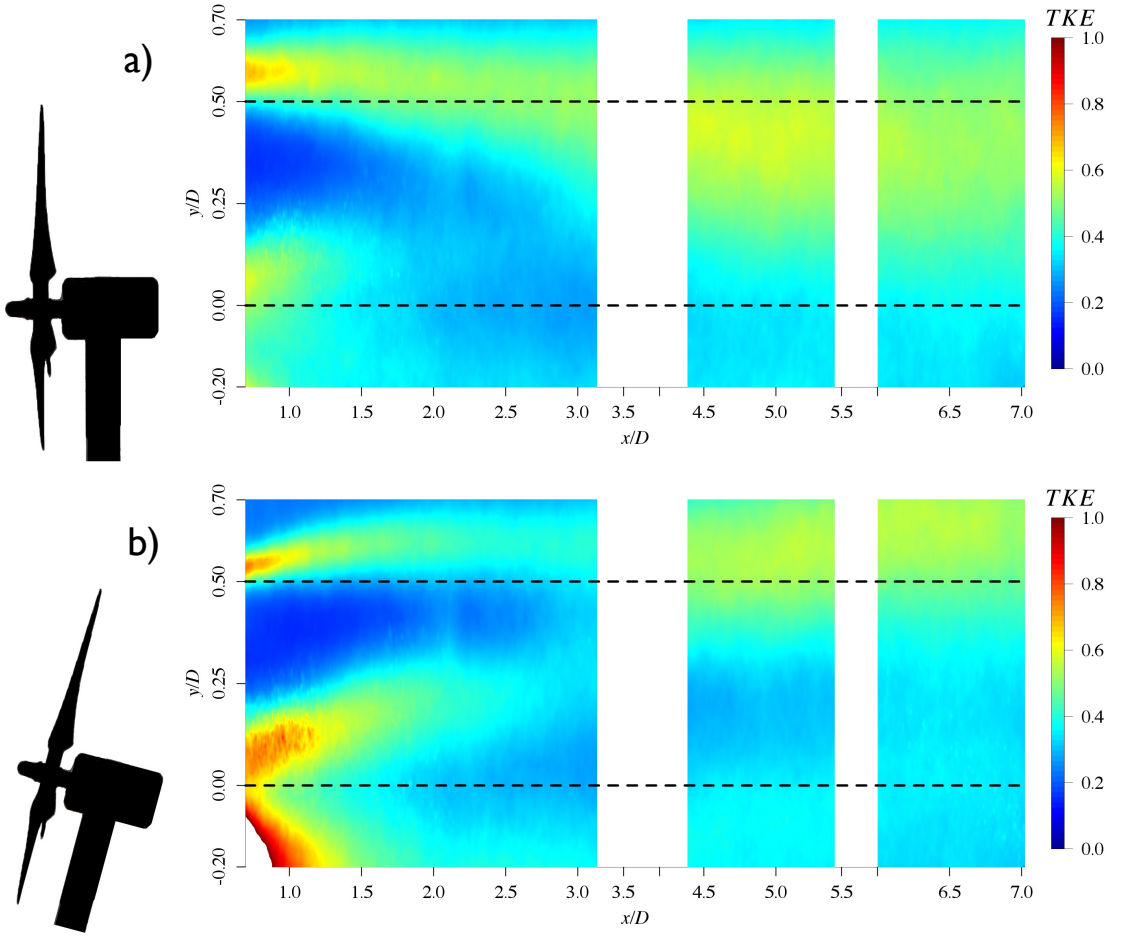

Abbildung 16: Contours of turbulent kinetic energy $TKE = \frac{1}{2}(\overline{uu} + \overline{vv} + \overline{ww})$ for fixed (a) and floating (b) case. The shapes develop analog to $\overline{uu}/U_{hh}^2$. Hub height ($y/D = 0$) and top blade tip ($y/D = 0.5$) are indicated by dashed horizontal lines.

Figure 17 shows the development of the flux of the Reynolds shear stress $-\overline{uv}U$, which has been found to be important for the energy being extracted by the turbine [6]. For $y/D < 0$ $-\overline{uv}U$ is negative for both cases, while in the floating case the negative flux shifts away from the wall with increasing downstream distance. In the fixed case, a positive flux is observed in the shear layer and the quantity grows over a larger area with increasing downstream distance. At the top tip of the rotor, the magnitude remains relatively constant at about 0.9 m^3/s^3. In contrast, in the floating case, the area of positive flux increases slower with increasing distance. In addition and still observing the top-tip of the rotor, the flux of mean kinetic energy increases in magnitude as the flow advects downstream for the floating case as well as moving away from the top-tip rotor location. The large negative blue area is restricted to $y/D < 0$ on the fixed case. This contrary to the floating case were the flux crosses

the $y/D < 0$ into the top half of the rotor and it is permanent even at $x/D = 7D$.

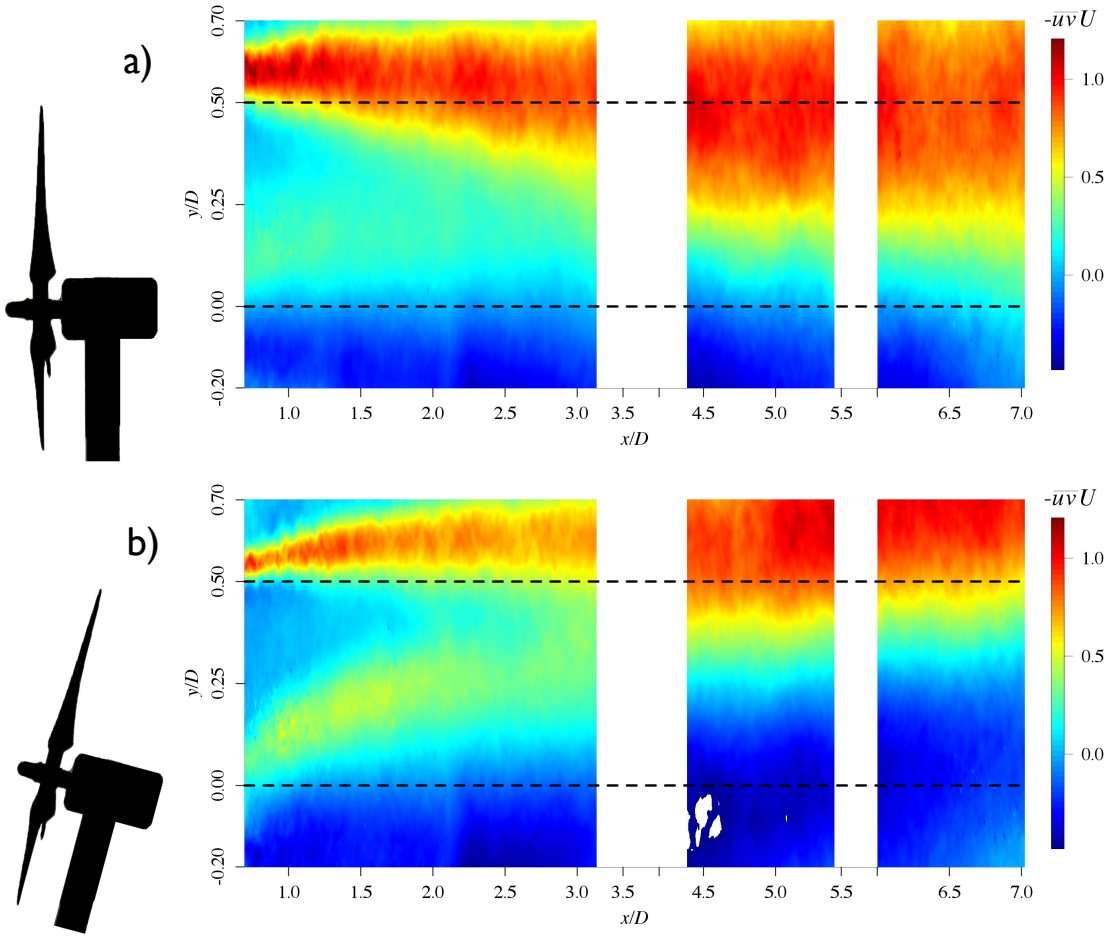

Abbildung 17: Contours for the flux of Reynolds shear stress $-\overline{uv}U$ for fixed (a) and floating (b) case. The flux of the shear stress represents the power that can be extracted. Hub height ($y/D = 0$) and top blade tip ($y/D = 0.5$) are indicated by dashed horizontal lines.

The contours of vertical flux of the normal Reynolds stress component $-\overline{vv}V$ for the fixed and floating cases in Figure 18 a and b, respectively. For the fixed case, the largest magnitudes of the mean vertical flux exist behind the hub, but the overall mean vertical flux of $-\overline{vv}V$ is close to zero with -0.004 m^3/s^3. For the floating case, $-\overline{vv}V$ is mostly positive with an average value of 0.04 m^3/s^3. Although these components are small compared to $-\overline{uv}U$, a remarkable difference exists between the two cases, which is consequently attributed to the oscillations of the turbine, thus contributing to enhanced transport due to the vertical fluctuations.

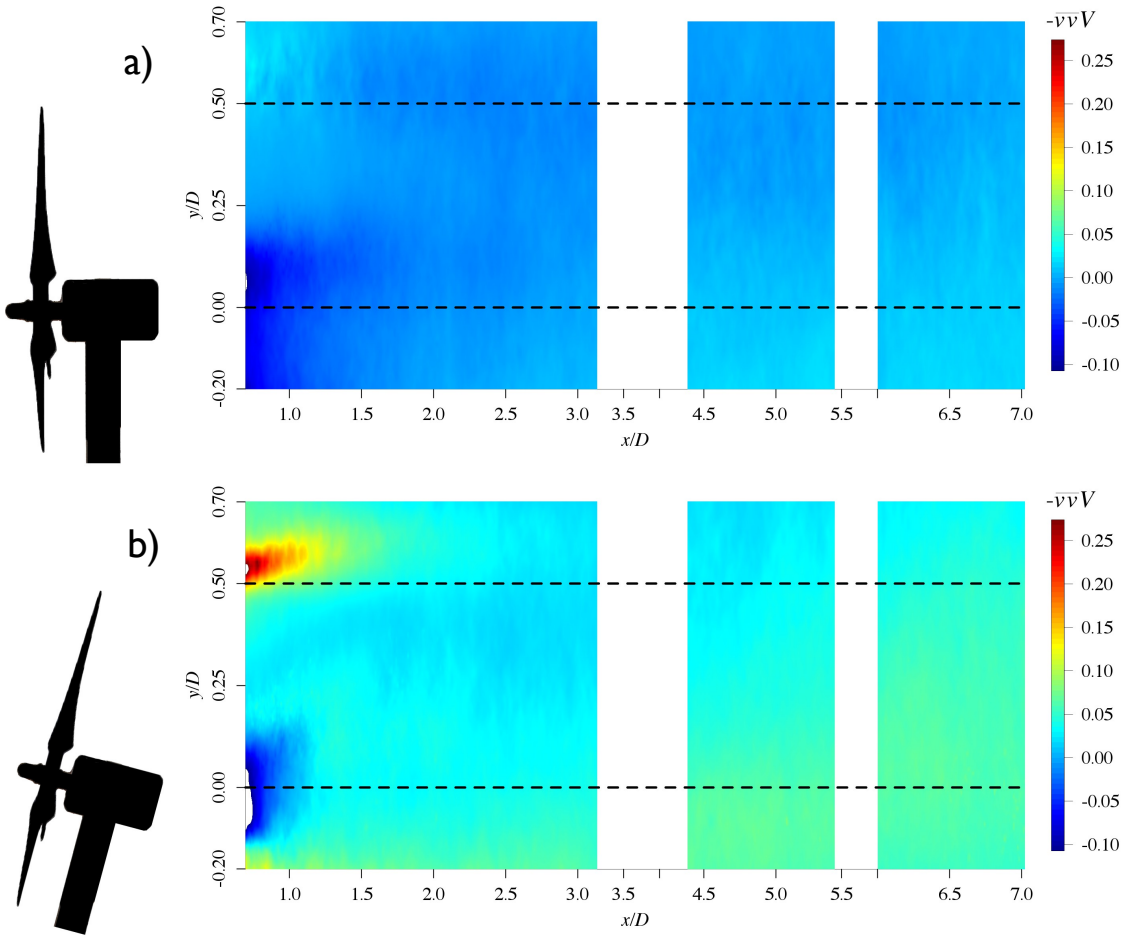

Abbildung 18: Turbulent kinetic flux in wall normal direction component $-\overline{vv}V$ of the wake for fixed and floating cases.

Comparison with models

Measured profiles of U/U_{hh} are compared to wake models as proposed by [1, 10, 13, 20, 21, 27, 30] at positions of $x/D = 1.5D$, $3D$, $4.5D$ and $7D$ and the models are described in § 2.2. These are shown in figures 19 and 20 for the fixed and floating turbine cases, respectively.

For the fixed case, all wake models with the exception of the Larsen model overestimate the wake expansion at $1.5D$. For the Jensen model, which has a hat-shaped profile, the output of the model does not match the experimental data. Since the prescription of the model is solely determined by k in the far wake behavior, the difference is expected. The Ainslie model is set to a constant Gaussian profile for distances less than $2D$, hence at $x/D = 1.5D$, the deficit is greater than the experimental data. The uniform actuator disk RANS model results in a wake

that is comparable to the diameter of the disk. It acts like a porous bluff body, and ignores aerodynamic details, like tip vortices, nacelle and tower effects, that causes, once again, the profile of the wake to be more affected by the rotor than the experimental data. At larger distances x/D of $4.5D$ and $7D$, maximum of the wake deficit coincides with the experimental data. Nevertheless, the rest of the profile does not collapse with the experimental data due to inherent shape of the profile, (i.e., top-hat shape). Furthermore, the Ainslie and RANS models improve considerably in comparison at these downstream distance although the maximum is slighly overpredicted. Taking into account all of the employed models, the RANS model best matches the experimental data as it takes into account additional terms compared with the other models. Of particular interest is the influence due to the wall, which observes the influence of the developing boundary layer. Noticeably, relatively increased velocity deficits reside in the prediction of the models compared with the acquired data. This is due to the assumption built into the Jensen, Larsen and Ainslie models that the total wake deficit is calculated based on the concept of superposition of the inflow profile in addition to the modeled deficit. It is well understood that the inflow profile is not constant as it advects downstream. On the other hand, the RANS simulation captures the changes in the development of the wake and more practically the shape of the velocity deficit. However, an offset at all measured distances is clearly present, which can be attributed to either the parameterization of the wall and/or the turbulence closure. The latter inherently leads to the use of an eddy viscosity in the wake region that tends to be a larger sink that otherwise prescribed.

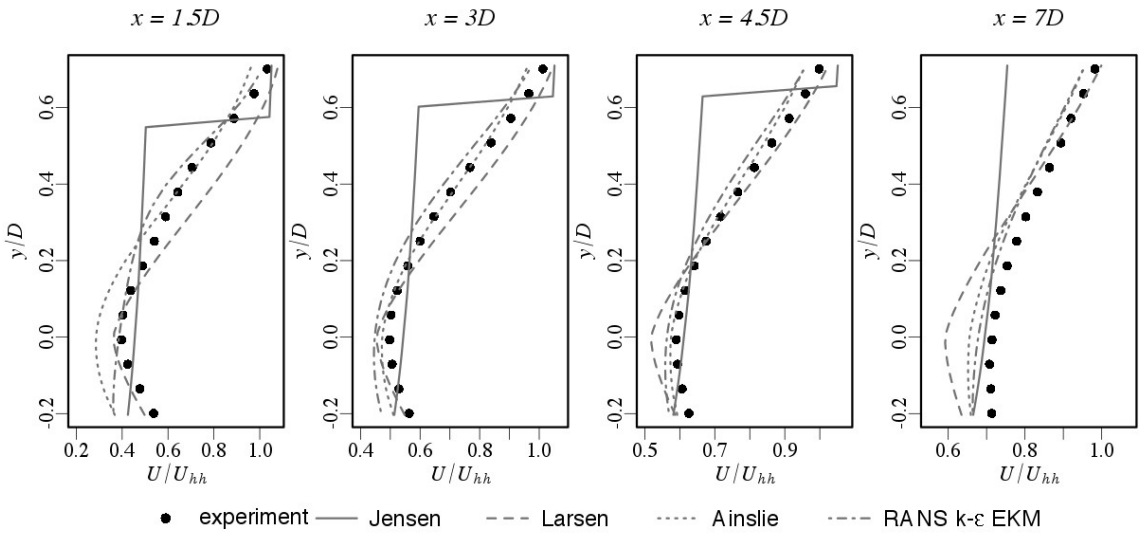

Abbildung 19: Comparison of measured mean profiles of U/U_{hh} with various wake models for the fixed case.

In stark contrast as observed in the floating case, the models do not manage to capture the shift of the measured wake deficits which reside at increased values of the normalized wall-normal coordinate, y/D as shown in Fig. 20. It is of no surprise that the velocity profiles generated via the Jensen, Larsen and Ainslie do not collapse with the experimental data as these have not been constructed to represent the conditions as undertaken in the experiment documented in this study; explicitly, a wind turbine with induced pitch due to the incoming flow. In fact, both the Jensen and Ainslie models assume an axial symmetry in the wake. As a result of the pitch motion not being well represented in the models, the wake is then directed towards the wall. Therefore, the overall effect is reduced to a change in both thrust and power coefficients. Different than the other models, the RANS model was tilted by 15° as well as the rotor position being shifted accordingly. Even though these changes are implemented, the RANS model still is not able to capture the behavior as that observed in the experimental data. This is then attributed to the turbulence model, which considers that the Reynolds stress tensor is inherently isotropic. Subsequently, it cannot capture the anisotropy as observed by the wake.

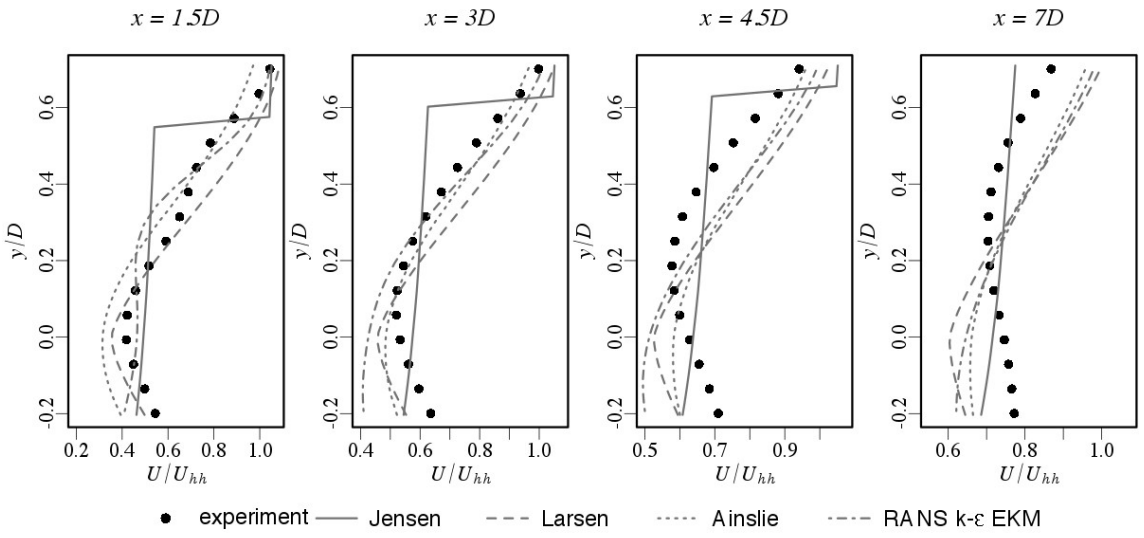

Abbildung 20: Comparison of measured mean profiles of U/U_{hh} with various wake models for the floating case.

2.5 Discussion

Platform pitch and streamwise oscillations have a strong impact on the mean shape of the wake as well as the magnitudes of all velocity components. Due to the oscillations in the floating case, the turbine experiences a variable shear flow. The pitch motion of the platform with an average inclination angle of 17.6° skews the mean streamwise velocity component in the wake with a positive slope, with an angle of approximately 3°. This observation is comparable to results observed in yawed turbines with a yaw misalignment of 20° [24, 28]. Taking the analogy to wake deflection of turbines under yaw condition, the average skew angle of the wake can partially be explained by momentum theory since the non-axial momentum extraction is due to the pitching effect of the turbine [4]. In order to capture other effects as generated by the oscillation of the platform, more complex descriptions are necessary as highlighted by Sebastian *et al.* [32]. The shift due to the pitch motion/oscillations results in a far wake which has not fully recovered and thus 14-16% less power is available for the downwind turbine. Furthermore, the 10% decrease in thrust force as observed in the floating turbine is due to the decrease in mean velocity and upward shift of the wake. It is also expected that a completely different load distribution on the rotor of a downwind turbine is observed compared to that of non-floating turbine.

The increase of the wall-normal mean velocity in the floating case is of importance, since vertical flow is often not considered in wake models. This is certainly true

considering the development of V/U_{hh} for the fixed case (Fig. 6b), which subsequently, leads to potential, unpredicted fatigue loads on downstream turbines in the floating case. The shape of the V/U_{hh} wake component is not changed by the oscillations (compare contours in 6 a and b), but the magnitudes are increased, resulting in high vertical wind speeds in the floating case. It can then be concluded that the vertical component of the flow field in the wake of an floating turbine can not be neglected and has to be considered for operating conditions of downstream turbines.

When evaluating the out of plane component that is the spanwise component of the mean velocity, W/U_{hh}, symmetry in this component between the top and bottom of the rotor (i.e., $y/D > 0$ and $y/D < 0$, respectively) for the fixed turbine is entirely disrupted when oscillations are taken into account as seen in the floating case; although as the flow develops downstream, the signatures due to the out of plane velocity are less pronounced in comparison to the fixed case.

Furthermore, the oscillations and inclination experienced by the turbine have a strong impact on the fluctuations of the flow and on the features of turbulent kinetic energy in the wake, where in the top tip of the fixed case, the features of $\overline{uu}$, $\overline{uv}$ and TKE seem to diffuse with increasing distance. These features become more and more pronounced with increasing downstream distance for the oscillating turbine. The evaluation of the turbulent kinetic energy for the turbine without induced motion is maximum at the top-tip of the blade and is shifted upwards in the oscillating case. The same quantity, now at hub height is extremely enhanced where its values nearly double again pointing towards the resulting effect of the pitch dynamics. This increase can be linked with the increase in the mean vertical velocity component.

From the point of view of a downwind turbine, the shear stress distribution in the fixed case leads to negative fluctuating shear forces above hub height and positive fluctuating shear forces below hub. Similarly, strong fluctuations are observed at the nacelle. In the floating case, most of a downwind rotor potentially experiences positive fluctuating shear forces, but have a strong transition from positive to negative shear force at the blade tips.

Turbulent kinetic energy is a measure for the amount of kinetic energy that is contained in the fluctuations. For the fixed case, the rotor of a downwind turbine would be exposed to strong fluctuations above hub height. In the floating case, the smaller TKE in the far wake results in a steadier inflow situation for a downstream turbine, which is positive from the point of view of loads on a turbine. The vertical shift of the turbulence quantities, on the other hand, affects the power production adversely. When considering the mean kinetic energy flux, $-\overline{uv}U$, the upwards shift as seen in the floating case results in a lower momentum entrainment from overhead

flow, thus resulting in less energy available in the downstream wind and therefore in less power available for a downstream turbine.

Almost no vertical transport of vertical fluctuations can be observed in the fixed case, which compares well to findings of [11], where $-\overline{vv}V$ is several orders of magnitudes smaller than the main contributor to the flux $-\overline{uv}U$. In the floating case, $-\overline{uv}U$ remains much bigger than $-\overline{vv}V$, but the pitch motion of the turbine creates high positive transport at the blade tips and a negative transport behind the hub. Due to the overall positive vertical flux, entrainment of kinetic energy from the free stream above the canopy is reduced in the floating case. This corresponds well to the flow in the mean streamwise direction, where the wake recovery is diminished as observed by the far wake, thus contains less kinetic energy for a downstream turbine.

The comparison with wake models shows that for the fixed case, the shape and magnitudes of the streamwise component of the wake in midrange distance (x = $3D$ - $7D$) can be approximated by the Ainslie, the Larsen and the actuator disk models, even though in the lower half of the wake the models overpredict the deficit. In the floating case, all models fail to capture the vertical displacement in the streamwise component, resulting in an inaccurate wake description, thus the inflow for a downwind turbine, which would lead to incorrect load and power predictions for a downwind turbine.

2.6 Conclusions

Wind tunnel experiments were performed to compare the wake development of a fixed and a streamwise oscillating wind turbine model using stereo PIV. Statistical analysis of wake development from $0.7D$ - $7D$ was performed and differences in their quantities were elaborated for both cases. The pitch motion of the turbine has a strong impact on the development of the mean components as well as on the turbulent quantities. The vertical shift of U/U_{hh} results in less available kinetic energy for a downwind turbine in offshore conditions, which could be due to the shifted turbulent kinetic flux $-\overline{uv}U$. The upwards shift of the turbulent kinetic energy reduces potential fatigue loads on a downwind turbine, but the increase in V/U_{hh} adds to such loads. Comparison of the measurements with wake models reveals minor discrepancies of the model predictions in the fixed case, but these models fail to describe the wake behind a wind turbine with induced dynamic pitch motion. Floating platforms for wind turbines provide the capability for allowing the production of energy offshore. Nevertheless, already the pitch motion of the turbine results in new challenges for wake modeling, thus providing the opportunity for furthering the modeling capabilities of a new scenario (i.e. offshore versus onshore). This certainly has great implications in the experienced

loads by the turbine as well as the power production capabilities. The article includes dynamic pitch motion of a wind turbine; it would also be relevant to discern the differences between the dynamic pitching with static pitch in the future.

Acknowledgments

The authors would like to thank Stefan Ivanell for providing the blade design, Carlos Peralta for providing the turbulence model implementation for the actuator disk model simulation. This work was supported in part by grants from the Federal Environmental Foundation (DBU), Germany.

Appendix - Wake Model Equations

Jensen Model

The wake diameter D_w in the Jensen model [13] increases linearly with the downstream distance x behind the rotor:

$$D_w(x) = D + 2kx \tag{4}$$

with rotor diameter D and coefficient k, where we adopted $k = 0.04$. Momentum conservation for the horizontal velocity component U yields:

$$U(x) = U_0 \left[1 - \left(1 - \sqrt{1 - c_T}\right) \left(\frac{D_w(x)}{D}\right)^{-2}\right] \tag{5}$$

with inflow velocity U_0 and thrust coefficient c_T.

Larsen Model

In the Larsen model [19], a two dimensional system of partial differential equations is solved analytically for the first two orders of an expansion in the axial velocity deficit. The resulting wake radius R_w as a function of downwind distance x is [29]:

$$R_w(x) = \left(\frac{105}{2\pi}\right)^{1/5} c_1^{2/5} \left[c_T A (x + x_0)\right]^{1/3} \tag{6}$$

where $A = \pi D^2/4$ is the rotor area and the parameters c_1 and x_0 follow from fits to measurement data at $9.5D$:

$$c_1 = \left(\frac{D_{\text{eff}}}{2}\right)^{5/2} \left(\frac{105}{2\pi}\right)^{-1/2} \left(c_T A x_0\right)^{-5/6} \tag{7}$$

$$x_0 = 9.5D \left[\left(\frac{2R_{9.5}}{D_{\text{eff}}}\right)^3 - 1\right]^{-1} \tag{8}$$

The effective wake diameter D_{eff} and wake radius $R_{9.5}$ at distance $9.5D$, corrected for finite hub height effects, are:

$$D_{\text{eff}} = D\sqrt{\frac{1 + \sqrt{1 - c_T}}{2\sqrt{1 - c_T}}} \tag{9}$$

$$R_{9.5} = 0.5\left[R_{\text{nb}} + \min\left(H, R_{\text{nb}}\right)\right] \tag{10}$$

The latter relation was found empirically, with hub height H and:

$$R_{\text{nb}} = \max\left[1.08D, 1.08D + 21.7D\left(I_a - 0.05\right)\right] \tag{11}$$

where I_a is the ambient turbulence intensity.

The solution for the wake deficit to second order is:

$$\Delta U(x,r) = \Delta U_1(x,r) + \Delta U_2(x,r) \tag{12}$$

where:

$$\Delta U_1(x,r) = -\frac{U_0}{9}\left(c_T A(x+x_0)^{-2}\right)^{1/3}\left[r^{3/2}\left(3c_1^2 c_T A(x+x_0)\right)^{-1/2} - \left(\frac{35}{2\pi}\right)^{3/10}\left(3c_1^2\right)^{-1/5}\right] \tag{13}$$

and:

$$\Delta U_2(x,r) = U_0\left(c_T A(x+x_0)^{-2}\right)^{2/3}\sum_{i=0}^{4} d_i z(x,r)^i \tag{14}$$

The second order solution contains a sum over functions:

$$z(x,r) = r^{3/2}\left(c_T A(x+x_0)\right)^{-1/2}\left(\frac{35}{2\pi}\right)^{-3/10}\left(3c_1^2\right)^{-3/10} \tag{15}$$

and parameters:

$$d_1 = \frac{1}{5}(4 - 12\ d_2)\xi_0^6, \quad d_2 = \frac{1}{4}(6 + 27\ d_3)\xi_0^6 \tag{16}$$

$$d_3 = \frac{1}{19}(-4 + 48\ d_4)\xi_0^6, \quad d_4 = \frac{1}{40}\xi_0^6 \tag{17}$$

$$\xi_0 = \left(\frac{35}{2\pi}\right)^{1/5}\left(3c_1^2\right)^{-2/15} \tag{18}$$

The solution of the radial velocity component was ignored in this work.

Ainslie Model

The Ainslie model flow has an axial component, denoted as $U(x,r)$, and a radial component $V(x,r)$. The two dimensional system of partial differential equations is

then [18]:

$$\frac{\partial U}{\partial x} + \frac{1}{r}\frac{\partial (rV)}{\partial r} = 0 \tag{19}$$

$$U\frac{\partial U}{\partial x} + V\frac{\partial U}{\partial r} = \frac{1}{r}\epsilon(x)\frac{\partial (r\partial U/\partial_r)}{\partial_r} \tag{20}$$

with eddy viscosity modelled as:

$$\epsilon(x) = k r_w \left(U_0 - U_c(x)\right) \tag{21}$$

where $U_c(x)$ denotes the velocity at the centre line. We ignore a contribution from ambient turbulence, stratification effects and the Ainslie filter function. The constant k was chosen as $k = 0.015$, and the wake radius is defined as:

$$r_w = D\sqrt{\frac{3.56\ c_t\ U_0}{4(U_0 - U_{c,0})(2 - (U_0 - U_{c,0})/U_0)}} \tag{22}$$

with initial velocity at the centre line:

$$U_{c,0} = U_0\left[1 - \left(c_T - \frac{5}{100} - \frac{I}{10}\left(16\ c_T - \frac{1}{2}\right)\right)\right] \tag{23}$$

where I denotes the ambient turbulence level.

The solution of Equations (19) and (20) is obtained as follows. First, an initial Gaussian profile is assumed at $x = 2D$:

$$U(2D, r) = U_0 - (U_0 - U_{c,0})\ \exp\left[-3.56\left(\frac{r}{r_w}\right)^2\right] \tag{24}$$

and the initial axial velocity for $x > 2D$ is estimated by:

$$U^{\text{initial}}(x, r) = U(2D, r) + [U_0 - U(2D, r)]\,\frac{x - 2D}{x_{\max} - 2D} \tag{25}$$

where the guessed maximal extension $x_{\max}$ does not influence the final wake size after convergence. The initial field $V^{\text{initial}}(x, r)$ then follows from Equation (19).

The momentum Equation (20) is solved by discretising it in a Crank-Nicholson scheme, and re-writing it as a tri-diagonal matrix problem. The centre line deficit and the radial velocity field are then updated using the continuity Equation (19), and the solution is iterated until convergence is obtained.

Literaturverzeichnis

[1] J. F. Ainslie. Development of an eddy viscosity model for wind turbine wakes. In *BWEA Wind Energy Conference*, Oxford, UK, 1983.

[2] R. J. Barthelmie, S. C. Pryor, S. T. Frandsen, K. S. Hansen, J. G. Schepers, K. Rados, W. Schlez, a. Neubert, L. E. Jensen, and S. Neckelmann. Quantifying the Impact of Wind Turbine Wakes on Power Output at Offshore Wind Farms. *Journal of Atmospheric and Oceanic Technology*, 27(8):1302–1317, August 2010.

[3] RJ J. Barthelmie, GC C. Larsen, S. T. Frandsen, L. Folkerts, K. Rados, S. C. Pryor, B. Lange, and G. Schepers. Comparison of Wake Model Simulations with Offshore Wind Turbine Wake Profiles Measured by Sodar. *Journal of Atmospheric and Oceanic Technology*, 23(7):888–901, July 2006.

[4] T Burton, N Jenkins, D Sharpe, and E Bossanyi. *Wind energy handbook*. 2011.

[5] CP Butterfield, W Musial, and J Jonkman. *Engineering challenges for floating offshore wind turbines*. 2007.

[6] Raúl Bayoán Cal, José Lebrón, Luciano Castillo, Hyung Suk Kang, and Charles Meneveau. Experimental study of the horizontally averaged flow structure in a model wind-turbine array boundary layer. *Journal of Renewable and Sustainable Energy*, 2(1):013106, 2010.

[7] Marc Calaf, Charles Meneveau, and Johan Meyers. Large eddy simulation study of fully developed wind-turbine array boundary layers. *Physics of Fluids*, 22(1):015110, 2010.

[8] Leonardo P. Chamorro and Fernando Porté-Agel. Effects of Thermal Stability and Incoming Boundary-Layer Flow Characteristics on Wind-Turbine Wakes: A Wind-Tunnel Study. *Boundary-Layer Meteorology*, 136(3):515–533, June 2010.

[9] P. A. Davidson. *Turbulence : an introduction for scientists and engineers*. Oxford, UK ; New York : Oxford University Press, 2004.

[10] A. El Kasmi and C. Masson. An extended model for turbulent flow through horizontal-axis wind turbines. *Journal of Wind Engineering and Industrial Aerodynamics*, 96(1):103–122, 2008.

[11] Nicholas Hamilton, Matthew Melius, and Raúl Bayoán Cal. Wind turbine boundary layer arrays for cartesian and staggered configurations : Part I , flow field and power measurements. *Wind Energy*, pages 1–20.

[12] AR Henderson, D Witcher, and CA Morgan. Floating support structures enabling new markets for offshore wind energy. *Proceedings of the EWEC*, 2009.

[13] J. O. Jensen. A note on wind generator interaction. Technical Report Risø-M-2411, Risø National Laboratory, 1983.

[14] JM Jonkman. Dynamics of offshore floating wind turbines—model development and verification. *Wind Energy*, (June):459–492, 2009.

[15] JM Jonkman and D Matha. *A quantitative comparison of the responses of three floating platforms*. Number March. 2010.

[16] JM Jonkman and D Matha. Dynamics of offshore floating wind turbines—analysis of three concepts. *Wind Energy*, (January):557–569, 2011.

[17] Hyung Suk Kang and Charles Meneveau. Direct mechanical torque sensor for model wind turbines. *Measurement Science and Technology*, 21(10):105206, October 2010.

[18] B. Lange, H. P. Waldl, A. G. Guerrero, D. Heinemann, and R. J. Barthelmie. Modelling of offshore wind turbine wakes with the wind farm program flap. *Wind Energy*, 6(1):87–104, 2003.

[19] G. C. Larsen. A simple wake calculation procedure. Technical Report Riso-M-2760, Risø National Laboratory, 1988.

[20] G. C. Larsen. A simple stationary semi-analytical wake model. Technical Report Risø-R-1713, Risø National Laboratory, 2009.

[21] J. F. Manwell, J. G. McGowan, and A. L. Rogers. *Wind Energy Explained*. Wiley and Sons, UK, 2009.

[22] D Matha, M Schlipf, A Cordle, R Pereira, and J Jonkman. *Challenges in Simulation of Aerodynamics, Hydrodynamics, and Mooring-Line Dynamics of Floating Offshore Wind Turbines*. Number October. 2011.

[23] Hidekazu Matsukuma and Tomoaki Utsunomiya. Motion analysis of a floating offshore wind turbine considering rotor-rotation. *The IES Journal Part A: Civil & Structural Engineering*, 1(4):268–279, November 2008.

[24] Davide Medici. *Experimental Studies of Wind Turbine Wakes Power Optimisation and Meandering*. PhD thesis, KTH, 2005.

[25] Walt Musial, Sandy Butterfield, and National Renewable. Energy from Offshore Wind. 18355, 2006.

[26] N. G. Nygaard. Construction and validation of a new offshore wake model. ICOWES conference, Lyngby, Danmark, 2013.

[27] OpenFOAM. http://www.openfoam.org, 2013. [Online; accessed 05-November-2013].

[28] P Parkin, Richard Holm, and Davide Medici. The application of piv to the wake of a wind turbine in yaw. In *DLR-Mitteilung*, pages 155–162, 2001.

[29] D. J. Renkema. *Validation of wind turbine wake models*. PhD thesis, Delft University of Technology, 2007.

[30] P. J Richards and R. P. Hoxey. Appropriate boundary conditions for computational wind engineering models using the $k - \epsilon$ turbulence model. *Journal of Wind Engineering and Industrial Aerodynamics*, 46-47(0):145–153, 1993. Proceedings of the 1st International on Computational Wind Engineering.

[31] J. Schmidt and B. Stoevesandt. Wind farm layout optimisation using wakes from computational fluid dynamics simulations. Submitted at EWEA 2014 conference.

[32] T Sebastian and M A Lackner. Development of a free vortex wake method code for offshore floating wind turbines. *Renewable Energy*, 46:269–275, 2012.

[33] T Sebastian and MA Lackner. Characterization of the unsteady aerodynamics of offshore floating wind turbines. *Wind Energy*, (March 2012):339–352, 2012.

[34] Thomas Sebastian and Matthew Lackner. Analysis of the Induction and Wake Evolution of an Offshore Floating Wind Turbine. *Energies*, 5(12):968–1000, April 2012.

[35] DA Simms, S Schreck, M Hand, and LJ Fingersh. *NREL unsteady aerodynamics experiment in the NASA-Ames wind tunnel: A comparison of predictions to measurements*. Number June. 2001.

[36] L. M. Swain. On the turbulent wake behind a body of revolution. *Proc. Roy. Soc. Lond. A*, 125:647–659, 1929.

[37] Tomoaki Utsunomiya, Hidekazu Matsukuma, and Shintaro Minoura. On sea experiment of a hybrid spar for floating offshore wind turbine using 1/10 scale model. In *ASME 2010*, number 2006, pages 1–8, 2010.

[38] LJ Vermeer, JN Sø rensen, and A Crespo. Wind turbine wake aerodynamics. *Progress in aerospace sciences*, 39:467–510, 2003.

[39] C. M. Wang, T. Utsunomiya, S. C. Wee, and Y. S. Choo. Research on floating wind turbines: a literature survey. *The IES Journal Part A: Civil & Structural Engineering*, 3(4):267–277, November 2010.

[40] Jerry Westerweel and Fulvio Scarano. Universal outlier detection for PIV data. *Experiments in Fluids*, 39(6):1096–1100, August 2005.

[41] Yu-Ting Wu and Fernando Porté-Agel. Large-Eddy Simulation of Wind-Turbine Wakes: Evaluation of Turbine Parametrisations. *Boundary-Layer Meteorology*, 138(3):345–366, December 2010.

[42] A Zervos and C Kjaer. Pure power: wind energy scenarios up to 2030. 2008.

3 Wake to wake interaction of floating wind turbine models in free pitch motion: An eddy viscosity and mixing length approach

Experiments were performed using two model wind turbines operated in tandem with a bottom-fixed configuration and a floating configuration with both turbines allowed to freely oscillate in the streamwise direction. Wakes of both turbines were measured using stereoscopic Particle Image Velocimetry. Turbulent characteristics of the far wake of the first turbine acting as the inflow for the downwind turbine were characterized calculating the eddy viscosity and mixing length profiles from the obtained data. The influence of the far wake on the statistical properties of the near wake of the second turbine are compared between the fixed and oscillating configurations. The incoming mixing length clearly influences the Reynolds stresses and turbulence production of the near wake in the shear layer. Below, the connection between incoming mixing length and the near wake is less evident, due to the impact of the nacelle and rotation of the rotor. For the oscillating turbine, the Reynolds stresses and turbulence production in the near wake of the downwind turbine are damped. Vertical fluctuations were found to decrease though an increase in the mean vertical component. New challenges arise in the design of a floating offshore wind farms, in terms of farm layout and load estimations.

3.1 Introduction

Wind energy is a major contributor to the renewable energies. To fulfill the increasing demand of power, wind turbines are operated in farms. The implementation of wind farms onshore is limited due to space constraints, therefore application of offshore wind turbines also in deep water is of interest [1]. For areas where no shallow water (< 50m) is available, several concepts have been developed for floating offshore wind turbines. Floating constructions add degrees of freedom to the system in comparison to onshore wind turbines.

In particular the interaction of wind turbines via wakes shows the need of a deeper knowledge of the wake development of wind farms for reliable operation and power prediction. Experimental studies were performed using model wind turbines operated in wind tunnels, where the influence of turbulent inflow conditions as well as atmospheric boundary layer stability on the performance of the turbines and on the wake development were investigated [2–9]. Generally, higher turbulence levels in the wake were found to increase momentum transport from undisturbed surrounding

flow and enhance wake recovering. Hancock [10] and Zhang [11] found convection in the boundary layer to facilitate the recovering of the wake due to enhanced moment transport. Investigation on the influence of tip speed ratios of the model wind turbine on the near wakes vortex structures were performed [6]. The evolution of the tip vortex structures and their interaction under uniform inflow were found to drive the mixing process in the wake, thus the recovery of the wake [12]. Incoming turbulence intensities on loads of a model turbine and the development of the near wakes turbulent structures have shown that higher incoming turbulence intensity results in higher turbulent kinetic energy and stresses in the wake, which enables faster recovering of the wake flow [13]. Zhang et al. [14] analyzed the near wake of a model wind turbine under different stratifications of the boundary layer using stereoscopic particle image velocimetry. Khosravi et al. [15] performed comparative wind tunnel experiments to investigate the effect of platform surge motion. They found a slight increase in power production of the moving turbine when compared to a stationary and also a decrease in Reynolds shear stress, with the conclusion of a weaker recovering of the wake in the floating case. Experimental and numerical [16,17] investigations of floating turbines in surge motion have shown an increase of thrust and power variations with increasing tip speed ratios of the turbines, with good agreement of experimental and numerical results for rated tip speed ratios and below. Sebastian et al. [18] performed numerical investigations on unsteady aerodynamics of floating wind turbines and found the pitch motion of a floating platform being one major contributor to unsteady flow effects. This paper deals with the case of floating wind turbines and the impact of the platform pitch motion on the wake.

In assuming a steady, incompressible and inviscid flow in a wind turbine array, the momentum balance for such flow is given by the Reynolds-averaged Navier-Stokes (RANS) equation as,

$$U_j \frac{\partial U_i}{\partial x_j} = -\frac{1}{\rho}\frac{\partial P}{\partial x_i} - \frac{\partial \overline{u_i u_j}}{\partial x_j} - F_{x_i}, \tag{26}$$

with U_i being the mean velocity components and u_i its fluctuations. Where the overbar denotes ensemble averages, $x_1 = x$ the streamwise, $x_2 =$ y the vertical and $x_3 = z$ the spanwise directions. The air density is given by ρ, the mean pressure by P and F_{x_i} is the thrust force by the turbine, which mainly acts in the streamwise direction [3, 9, 19, 20].

The vertical transport of kinetic energy in the wake region is connected to the Reynolds shear stress by the mean kinetic energy equation, which is given by,

$$U_j \frac{\partial \frac{1}{2} U_i^2}{\partial x_j} = -\frac{1}{\rho} U_i \frac{\partial P}{\partial x_i} + \overline{u_i u_j} \frac{\partial U_i}{\partial x_j} - \frac{\partial \overline{u_i u_j} U_i}{\partial x_j} - U_i F_{x_i}. \tag{27}$$

This closes the energy budget by balancing the convection of the mean kinetic energy of the flow to the mean pressure gradient, the production of turbulence kinetic energy, the gradient of kinetic energy flux and the power extracted by the turbine, respectively. Here we denote U_i as U, V, W and u_i as u, v, w respectively.

Averaging of the Navier-Stokes equation yields the Reynolds stress, which may be modeled to solve the RANS equation. This can be achieved using the Boussinesq hypothesis [21], which is stated as,

$$\overline{uv} = -\nu_t \left(\frac{\partial U}{\partial y} + \frac{\partial V}{\partial x} \right), \tag{28}$$

with ν_t being the eddy viscosity. A classical generalized model for the eddy viscosity on the basis of the mean strain rate tensor is given by the relation:

$$\nu_t = l_m^2 \sqrt{\frac{1}{2} \left(\frac{\partial U}{\partial y} + \frac{\partial V}{\partial x} \right)^2} = l_m^2 \cdot S, \tag{29}$$

using a mixing length l_m and the characteristic strain rate S [21]. Based on equations (28) and (29), ν_t and l_m can be obtained from $\partial U_j / \partial x_i$ and $\overline{uv}$; the latter two being measurable quantities. The model is widely used in meteorological descriptions like for canopy flows, e.g. to describe turbulent processes in the boundary layer above forested terrains [22, 23]. The concept was used by Bai et al. to characterize the development of the wake flow behind a fractal tree and was found to be suitable in the description of transverse momentum fluxes [24]. The approach of describing the Reynolds stress using the eddy viscosity is also applied in the context of wind energy application, where it is in part used in the *Dynamic Wake Meandering Model (DWD)*, which is a computationally inexpensive tool to describe wake effects [25].

Herein, the eddy viscosity and mixing length are calculated from data measured in wind tunnel experiments. These characteristic quantities are used to describe the turbulence in the far wake of a fixed and an oscillating turbine and its influence on the near wake of a second turbine positioned downwind as these act as an inflow condition. In the following, the experimental setup, the measurement planes as well as the SPIV settings will be described. Then, a characterization of the inflow conditions of the downwind turbine for the fixed and floating case in comparison to the free stream inflow is given. This is done by calculating the eddy viscosity and profiles of the mixing length from the measured SPIV data. Finally, conclusions on the mixing length and on implications for offshore floating wind farms are drawn.

3.2 Setup

In this section an overview of the facilities, the model wind turbines and used SPIV setup will be given.

Wind tunnel and model wind turbines

Experiments were performed in the closed-circuit wind tunnel at Portland State University, which has a cross section of 0.8m $\times$ 1.2m and a test section of 5m in length. The inflow conditions can be varied from 2 m/s to 40 m/s at a low turbulence level (cf. [7]). An image of the setup is provided in Figure 21 as well as a schematic view of the wind tunnel as well as the experimental setup is presented in Figure 34. In order to achieve atmospheric-like conditions, a passive grid was used to introduce a turbulence level of 9% and vertical strakes were used to shape the inflow velocity profile. Further details on the inflow characteristics can be found in [20], where measurements were performed to observe the differences in the wake of a fixed *versus* a pitching single wind turbine; these results were then compared to various wake models. Here, a second wind turbine was positioned in the wake of the upwind turbine at a distance of 7.5D. The turbines have a rotor diameter of 0.2 m, a nacelle with a diameter of 28 mm and a cylindric tower with a diameter of 16 mm. Hub height of both turbines was set to $hh = 0.24$ m. The turbines are mounted in gimbal supports which allow oscillations in streamwise direction and are stabilized by cylindrical weights. The position of the weight of the first turbine was chosen in such way that the turbine is allowed to oscillate with respect to the incoming flow. As a consequence of the inflow, the oscillation of the first turbine is around 16°-19° with a frequency range of 1.2-1.8 Hz [20]. Same setting for the stabilizing weight was chosen for the downstream turbine, which resulted in a reduced range of angles of 3°-5° for the oscillations and a frequency range of 0.7-0.9 Hz due to lower wind speed in the wake. The turbines in free pitch motion will be referred to as the floating case from hereon.

Abbildung 21: Photography of experimental facility and model wind turbines (downwind view).

Measured fields

The flow field was obtained using stereoscopic particle image velocimetry (SPIV) with all measurement planes being at the centerline of the turbine parallel to the main flow direction. The freestream inflow velocity at hub height of the upwind turbine T1 was set to $U_{hh} = 6.05$ m/s for all measurements. We select three measurement planes I, II, III (see Fig. 34) positioned at the centerline with respect to the turbines to characterize the inflow, the far wake of T1 and the near wake of T2. Setting the towers front edge of turbine T1 as $x/D = 0$ and hub height as $y/D = 0$, plane I was measured at x = -1.4 - -0.6 upstream of $x/D = 0$ and at a height from y/D = -0.5 - 0.5 without T1 being present to observe the inflow condition as seen by the first turbine. Measurements at plane II show the far wake of T1 for the fixed and floating cases at x/D = 6 - 7 downstream, which is equal to 1.5 - 0.5 upstream of T2. The measurements at plane III at x/D = 8.5 - 9.5 where performed with both turbines installed for the cases with both turbines being fixed and both being floating. Measurement planes II and III were shifted upwards to y/D = -0.25 - 0.75 to capture the average development of the dynamics at the top tip.

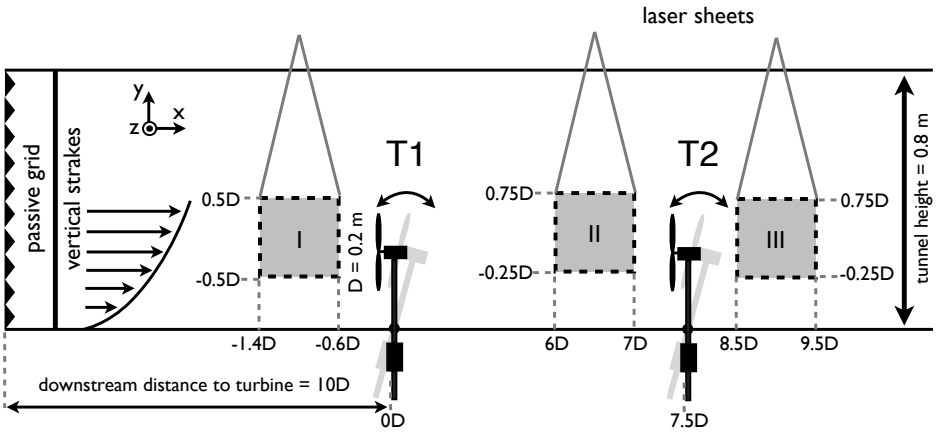

Abbildung 22: Wind tunnel setup with two model turbines. Inflow conditioning devices are represented as well as the measurement planes. *Schematic not to scale.*

Stereoscopic PIV

The SPIV setup consisted of a *LaVision* system with a Nd:YAG double pulsed laser, with two 2 k × 2 k pixel CCD cameras and a set time delay of 150 μs between exposures of the cameras, cf. [20]. The seeding fluid was neutrally buoyant in air atomized diethylhexyl sebecate. The thickness of the laser sheet was approximately 1 mm throughout the measurement plane. A standard *LaVision* two-plane measurement plate was used for calibration before each experiment. The resulting measurement plane was approximately 0.2 m × 0.2 m with a vector resolution of approximately 1.5 mm. For vector identification from the raw images, a multi-pass FFT based correlation algorithm was used, with decreasing size of interrogation windows of twice at 64x64 pixels, once at 32x32 pixels, each with 50% overlap. SPIV allows for measurements of three velocity components (U,V,W) in a two dimensional plane.

A sampling frequency of 1 Hz was used for the fixed case. In the floating case, the image acquisition was triggered to a fixed amplitude ($\approx 18.5°$) of oscillations of turbine T1 in the downstream direction to ensure the same influence of the oscillation on wake structures for each image. Therefore, a reflective strip was placed on the tower of the oscillating turbine. A *Monarch* optical tracker was positioned in such way, that every time the turbine reached a fixed pitch angle the SPIV system was triggered for data collection.

At each measurement plane, 2500 samples were taken. To calculate statistical quantities, an ensemble averaging was performed per plane, where U, V, W represent the mean velocity components and $\overline{u_i u_j}$ products of its averaged fluctuations. Spurious vectors were excluded from statistical calculations using a normalized median test

according to [26]. For all planes, the percentage of spurious vectors for U and V were below 1% and below 1.2% for W. To estimate the error of the statistical quantities a method called dependent circular block bootstrapping was used, which is described in detail in [27]. For this purpose, a new *bootstrap* series of 2500 samples was created for each measurement point by randomly sampling the data with replacement. For each bootstrap series the means and fluctuations were calculated. Repeating this procedure 3000 times allows for the estimation of confidence interval for the given statistic. For all calculated cases, the plane-averaged error with 95% confidence in the mean velocities was below 0.5% of the freestream velocity and in the fluctuations below 0.08% of the freestream velocity squared.

3.3 Characterization of the inflow

Inflow conditions for T1 and T2 are described via the eddy viscosity and mixing length. These are calculated from the obtained data in plane I and II. Profiles of the incoming mean streamwise component and stresses are shown in Figure 23. Information on statistical quantities of the far wake characteristics of T1 are given in [20]. The mean streamwise component of the inflow follows a logarithmic profile shaped by the strakes at the outlet of the wind tunnel. The normal stress $\langle\overline{vv}\rangle/U_{hh}$ shows a negative linear trend with increasing height while $\langle\overline{uu}\rangle/U_{hh}$ decreases strongly with increasing height up to $y/D = 0$ and stays constant above hub height. A more detailed discussion on the shear stress is provided in the following section. The freestream inflow is taken as reference to determine changes introduced by the presence of the turbine.

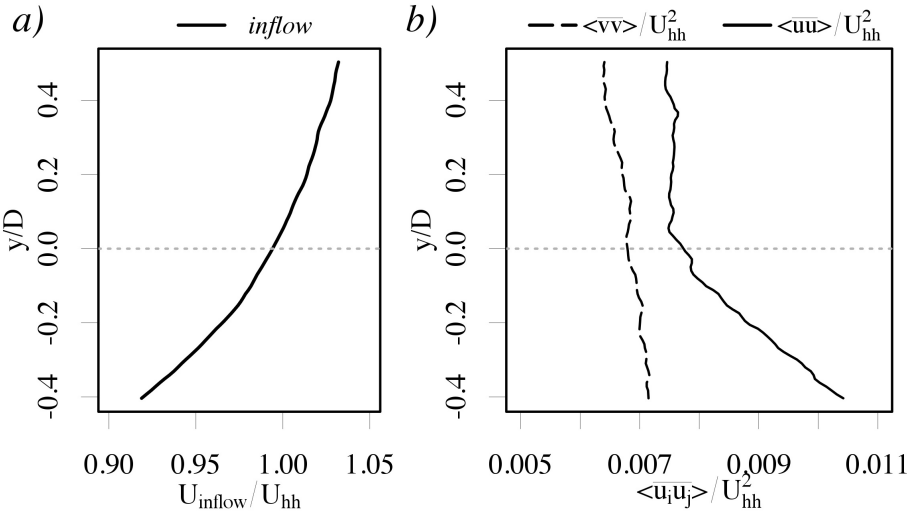

Abbildung 23: Vertical profiles of normalized mean streamwise component (a) and the stresses (b) for freestream inflow.

Calculation of eddy viscosity and mixing length

The mixing length is calculated for planes I and II using equations (28) and (29). Provided that the data is obtained from planar measurements, the spatial averaging scheme proposed by Raupach *et al.* is applied. Averages in the streamwise direction are denoted by $\langle\ \rangle$ [22, 28]. The averaging technique has been employed in [22, 29–31]. The averaging reduces the complexity of the three-dimensional airflow to lower dimensions, to allow simplified descriptions.

Figure 24 shows vertical profiles of $\langle\overline{uv}\rangle$ and the gradient $\langle\partial U/\partial y\ +\ \partial V/\partial x\rangle$ as a function of wall-normal distance for three cases. The freestream inflow obtained from plane I, the far wake as measured from plane II for the fixed and floating turbine. In Figure 24 a), the Reynolds shear stress shows a monotonic increase in the incoming flow as opposed to the wakes of the fixed and floating turbines. For the fixed case, the shear stress is positive below hub height and becomes negative above hub height. For the floating case, $\langle\overline{uv}\rangle$ shows slightly higher magnitudes through the profile and is shifted upwards due to the oscillations of the turbine when compared with the fixed turbine. It increases to 0.06 m^2/s^2 and inflects towards negative values crossing 0 m^2/s^2 at $y/D = 0.29$.

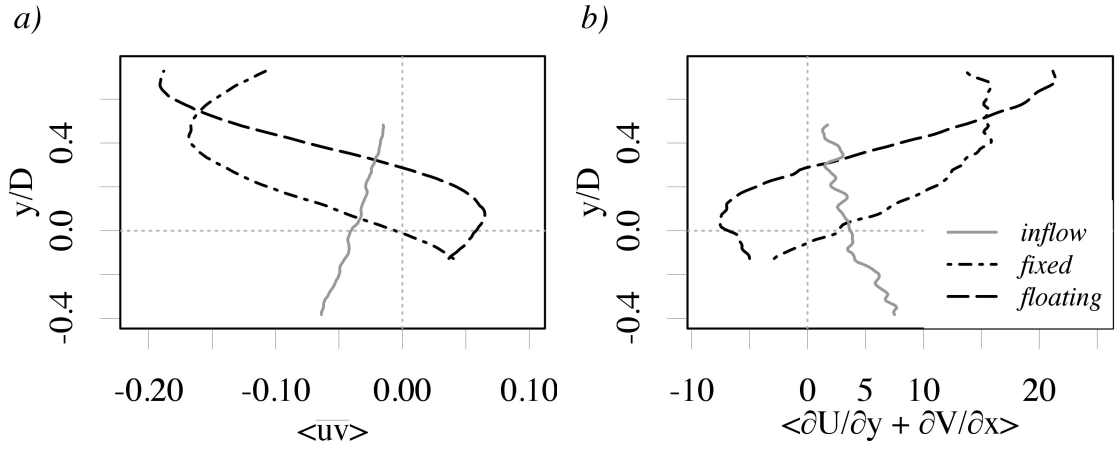

Abbildung 24: Vertical profiles of y/D over $\langle\overline{uv}\rangle$ (a) and $\langle\partial U/\partial y + \partial V/\partial x\rangle$ (b) for freestream inflow and far wake of fixed and floating turbine.

Figure 24 b) shows the mean velocity gradients for all three cases. The quantity for the freestream case decreases with increasing height. For the fixed and floating case, there is a significant gradient with positive slope occurring from around hub height to top tip. For the fixed case, the gradient is negative below hub height and becomes positive above hub height, which is the opposing behavior to the shear stress (Fig. 24 a)). For the floating case, the gradient is, once again, shifted upwards due to the

oscillations of the turbine, but, in contrast to $\langle\overline{uv}\rangle$, it decreases to its minimum of -7.6 s^{-1} and changes its slope to positive with increasing height. Similar to $\langle\overline{uv}\rangle$, it shows a wider range than for the fixed case and the gradient crosses zero at $y/D = 0.29$. Therefore both profiles are dominated by the upwards shift of the wake in the floating case.

Results

In Figure 25 a), the functional dependence of the averaged Reynolds shear stress $\langle\overline{uv}\rangle$ and $\langle\partial U/\partial y + \partial V/\partial x\rangle$ is plotted for the freestream inflow plane and the far wake plane of the first turbine for the fixed and floating case. The ranges of $\langle\overline{uv}\rangle$ and $\langle\partial U/\partial y + \partial V/\partial x\rangle$ (see Fig. 24 b) for the freestream inflow are approximately 80% smaller than for the floating case, indicating an increased homogeneity in the inflow for T1 than for T2. All three profiles exhibit a linear trend. A linear regression is performed, shown in Figure 25 b) to calculate the turbulence viscosity ν_t, as utilized by Bai *et al.* [24]. The resulting eddy viscosity is presented in table 3.3.

	inflow	fixed	floating
ν_t	0.0076 m^2s^{-1}	0.0112 m^2s^{-1}	0.0091 m^2s^{-1}

Tabelle 1: Calculated eddy viscosities for the freestream inflow as well as for the far wake in the fixed and floating case.

The lowest eddy viscosity is found for the inflow. The presence of the turbines causes an increase in ν_t and the highest value is found for the fixed case, where the turbine causes higher drag on the flow than in the floating case.

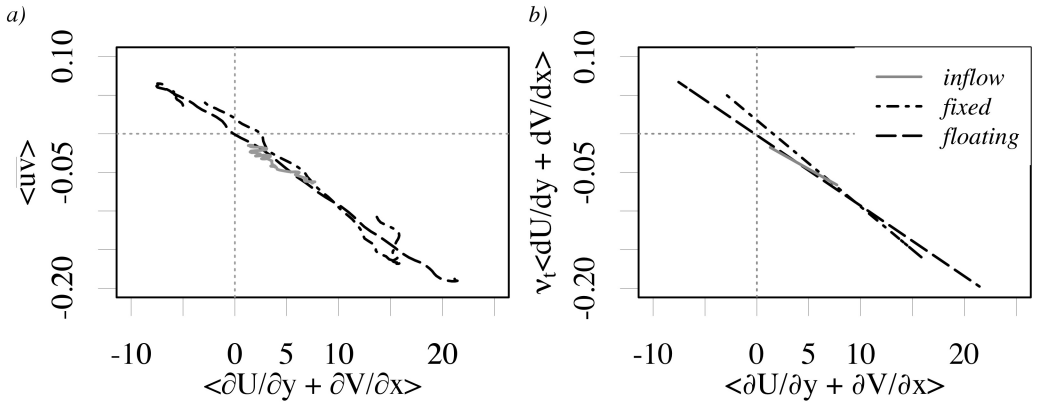

Abbildung 25: Profiles of $\langle\overline{uv}\rangle$ over $\langle\partial U/\partial y + \partial V/\partial x\rangle$ (a) and linear regression (b) for freestream inflow and far wake of fixed and floating turbine.

Knowing the eddy viscosity, the mixing length is then calculated by rearranging equation (29) and is

$$l_m = \sqrt{\frac{\nu_t}{\langle S \rangle}} \tag{30}$$

using the spatial averaged characteristic strain rate.

Figure 26 shows vertical profiles of l_m normalized by the hub height for the three cases. For the inflow, the mixing length becomes longer with increasing height. Above $y/D = 0.15$, the mixing length fluctuates in the range of $l_m/hh = 0.23$ - 0.36. For the fixed turbine, the mixing length increases for $y/D >$ -0.15 showing a maximum at $y/D =$ -0.06 and decreases rapidly with increasing y/D. Above $y/D = 0.4$, l_m/hh is approximately constant with a value of 0.13. For the floating case, the mixing length decreases below hub height from $l_m/hh = 0.21$ to $l_m/hh = 0.18$ and inflects towards higher values with its maximum of $l_{m_{max}} = 0.48$ at $y/D = 0.29$. For increasing y/D, it decreases dramatically and is smaller than for the fixed case for $y/D > 0.48$.

Table 3.3 shows that the vertical positions of the peaks in l_m/hh for the fixed and floating case correspond well to the zero crossings of the stain rate tensor in Figure 24 b). For the floating turbine, this is also the case for the zero crossing of $\langle \overline{uv} \rangle$, while for the fixed case the vertical position of $\langle \overline{uv} \rangle = 0$ is shifted upwards (see Fig. 24 a)).

	y/D-fixed	y/D-floating
$l_{m_{max}}$	-0.06	0.29
$\langle S \rangle = 0$	-0.06	0.29
$\langle \overline{uv} \rangle = 0$	-0.01	0.29

Tabelle 2: Vertical positions of maximum mixing length, zero crossings of the averaged strain rate tensor and the averaged shear stress for the fixed and floating case.

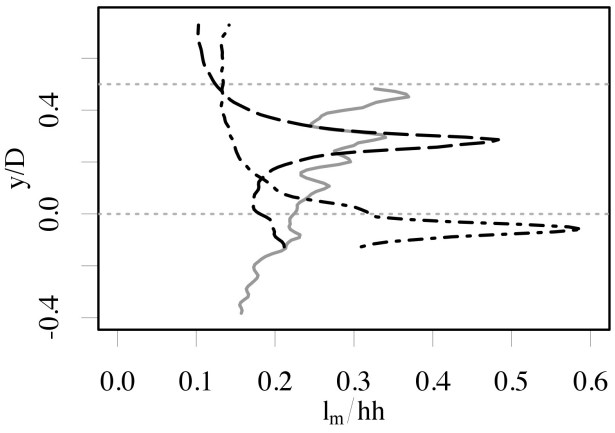

Abbildung 26: Vertical profiles of l_m/hh for the freestream, fixed and floating case. Dashed horizontal lines indicate hub height and top tip of the turbines.

Discussion

Although the values of ν_t are close in magnitude for the three cases, their differences coincide well with the opposing force acting on the incoming flow. It is biggest for the fixed turbine, because of its stiffness, becomes smaller for the floating turbine, due to its ability to move with the flow and is least for the inflow, where no force is applied on the flow. In the presence of a turbine, the increased ν_t also indicates an increased turbulent transport of momentum which is an important mechanism for the recovering of the wake [3, 9, 13]. The highest value for ν_t for the classical bottom fixed turbine is in good agreement with the results of [15, 20], where the wake for the fixed turbine was found to recover faster.

In contrast to ν_t, the profiles of $\langle\overline{uv}\rangle$ and $\langle\partial U/\partial y + \partial V/\partial x\rangle$ reveal marked differences between the inflow and when the turbine is present (cf. Fig. 24) Therefor, l_m/hh behaves completely different with and without the turbines, due to the contribution of the gradient profiles to the strain rate, $\langle S\rangle$, thus to the mixing length (cf. equation 30). The mixing length changes gradually in both cases with the turbine present, but contains the peaks due to the zero crossing of the strain rate tensor. In the freestream case, l_m/hh has an overall linear trend with height, but with local fluctuations. The overall mixing length is higher for the fixed case than for the floating, depicting stronger turbulent mixing in the far wake which is in agreement with higher ν_t and results presented in [20].

3.4 Impact on the near wake

Next, spatial details of the near wake of the second turbine measured at plane III will be presented. Contour plots of the ensemble averaged statistical quantities for the fixed (a) and floating (b) case are presented in order to compare the wake to wake interactions and to understand its relationship to the inflow. For each case, the calculated profile of l_m/hh is added to relate its changes to the mean flows, Reynolds stresses as well as production and fluxes of mean kinetic energy. Because of the discontinuities in l_m/hh, the x-axes of the mixing length plots are reduced to allow a better comparison of the differences in their development with height.

Mean flow

The contours of the mean streamwise and vertical flow are shown in Figure 27 and 28, respectively. The averaged streamwise velocity is normalized by the undisturbed incoming wind speed at hub height. The speed range in the fixed case varies from 0.28 U_{hh} at $y/D = 0.10$ behind the hub to 0.97 U_{hh} above top tip. In the floating case, an overall reduced velocity is observed with a range of 0.29 U_{hh} at $y/D = 0.11$ behind the hub and 0.85 U_{hh} above top tip. As in the case of T1, the deficit in the floating case is shifted upwards as well, but the deflection is less pronounced, due to the reduced amplitude of oscillations of T2 [20].

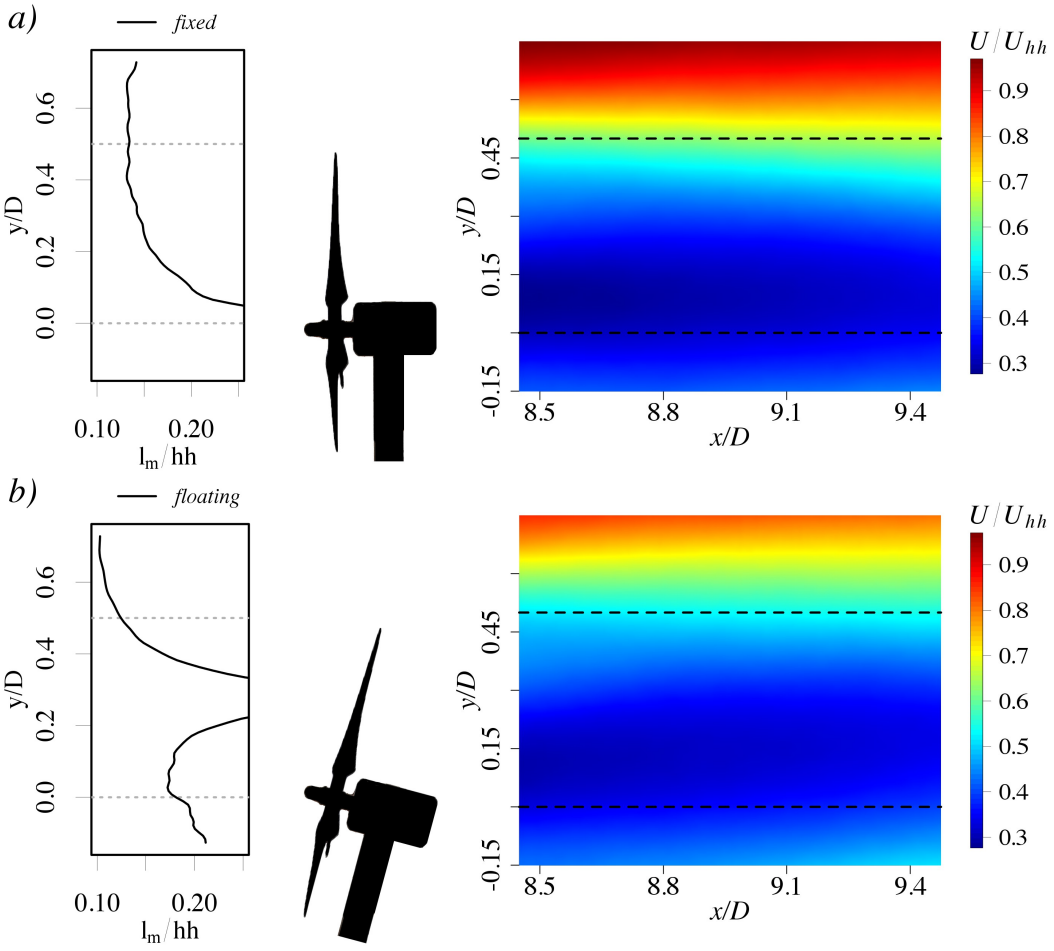

Abbildung 27: Contours of normalized mean streamwise component U/U_{hh} for near wakes of turbine T2 for the fixed (a) and floating (b) case.

Figure 28 shows the normalized wall-normal component V/U_{hh}. For the fixed case, we see that the velocity V/U_{hh} is close zero as expected. For the floating case, an overall increased vertical flow upwards is observed as was found for T1 in [20], with the only negative contribution found in an isolated area behind hub. The largest values of the vertical component are found in regions above top tip and below hub height. The same trend was found for T1 in [20], with similar velocity range, even though T2 shows a reduced inclination and oscillation.

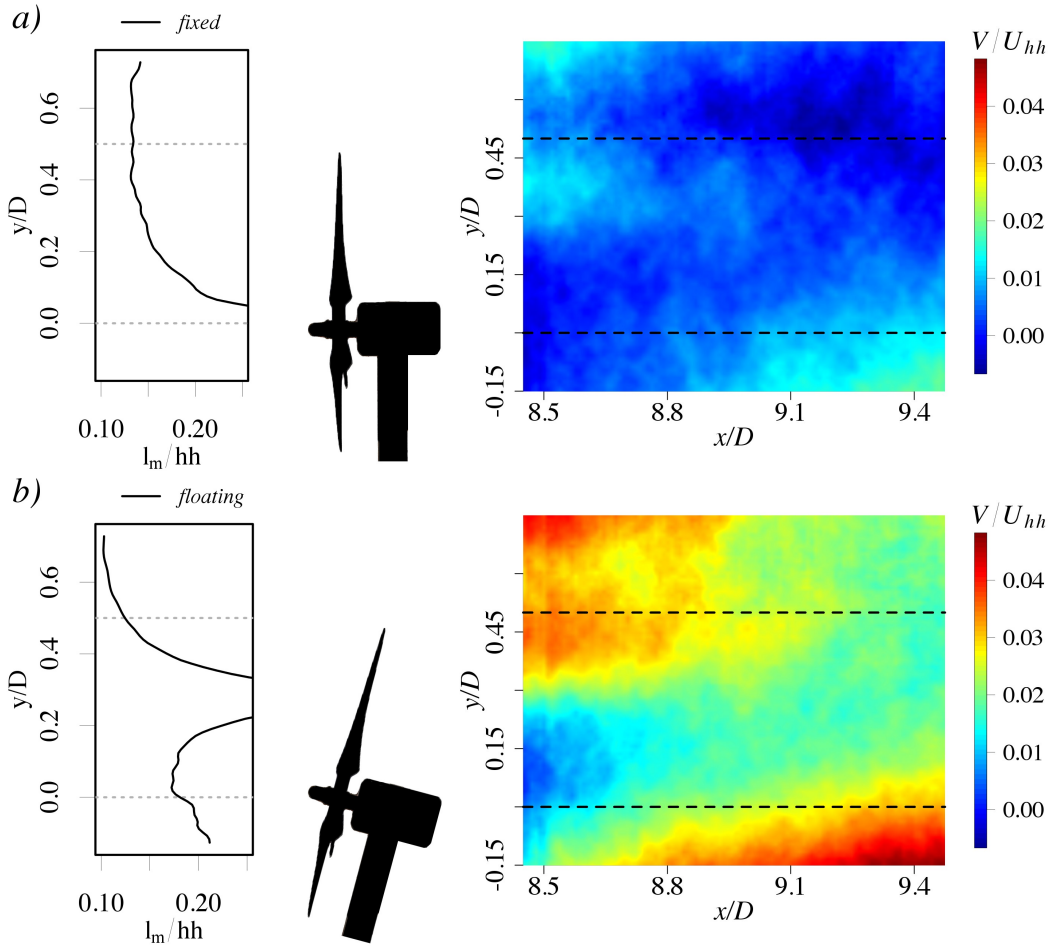

Abbildung 28: Contours of normalized mean wall-normal component V/U_{hh} for near wakes of turbine T2 for the fixed (a) and floating (b) case.

The higher mixing length of the inflow in the fixed case results in a stronger mixing thus a faster wake recovery compared to the floating case which is shown due to attaining a higher wind speed in the fixed case at top tip of the turbines. The upwards shift of the wake of T1 in the floating case causes a reduced mixing length and a less recovered wake, which is also represented in a lower eddy viscosity (cf. 3.3).

The incoming mixing length is not affecting the behavior of V/U_{hh}, even though its gradient is embedded in the calculation of l_m. This is due to its small contribution to the strain rate as was also found in [24].

Due to the slower recovering of the wake, the distance between floating turbines should be larger in a wind farm configuration to gain the same power. In addition, loads due to the increased vertical flow have to be considered in the estimation of fatigue loads.

Fluctuations

Resulting Reynolds stress tensor $\overline{u_i u_j}$ in the near wake of T2 is shown in Figures 29 to 31.

The normal Reynolds stress $\overline{uu}/U_{hh}^2$ for the near wake of the fixed and floating case is shown in Figure 29. In both cases, there is an extended region below top tip were $\overline{uu}/U_{hh}^2$ is close to zero. In the floating case, the stress is significantly reduced in the shear layer above top tip. Also, a slight increase in $\overline{uu}/U_{hh}^2$ is present at $y/D \approx 0.13$ - 0.3, corresponding well to the peak in l_m/hh.

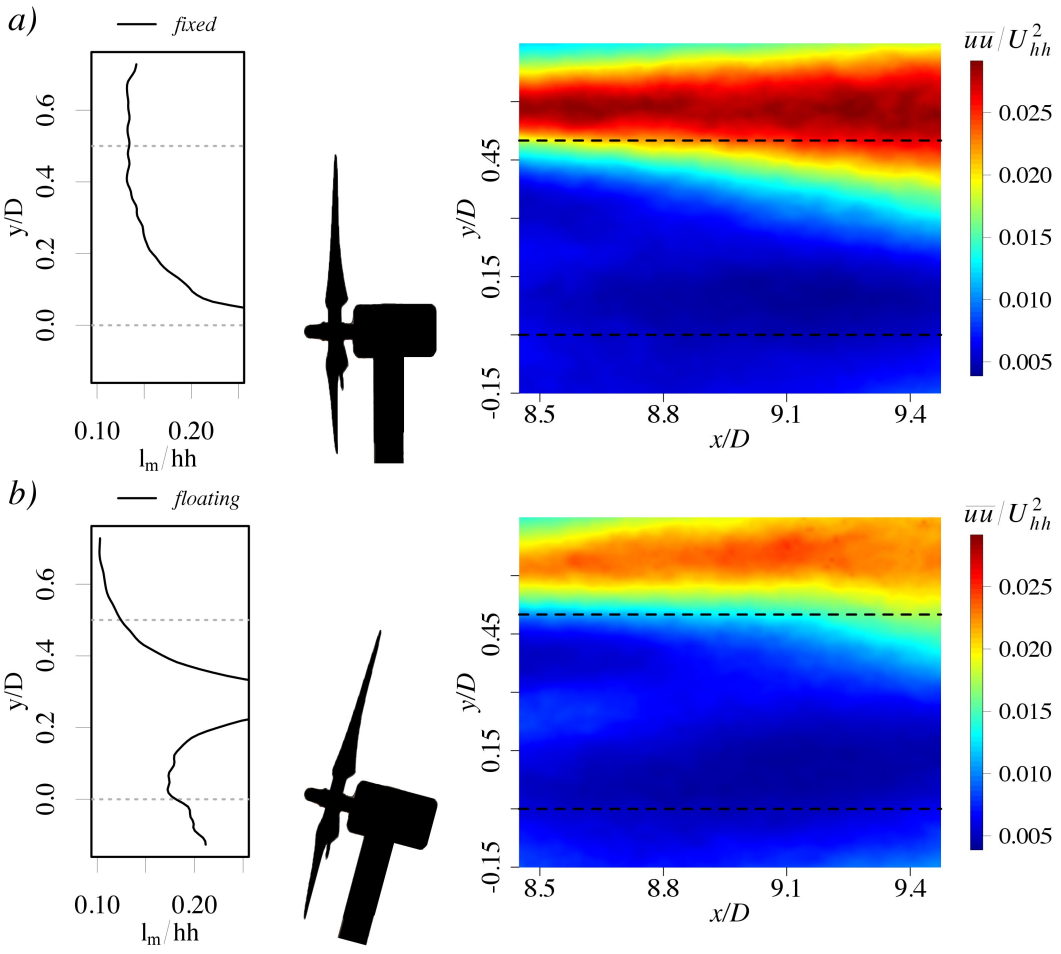

Abbildung 29: Contours of $\overline{uu}/U_{hh}^2$ for near wakes of turbine T2 for the fixed (a) and floating (b) case.

In Figure 30, the wall-normal Reynolds stress component $\overline{vv}/U_{hh}^2$ is shown. In the fixed case, $\overline{vv}/U_{hh}^2$ increases with downstream distance to a maximum of 0.045 $m^2 s^{-1}$ in the shear layer and depicts 20-40% higher values at the top tip compared to floating case, which coincides with the differences in l_m/hh in the inflow.

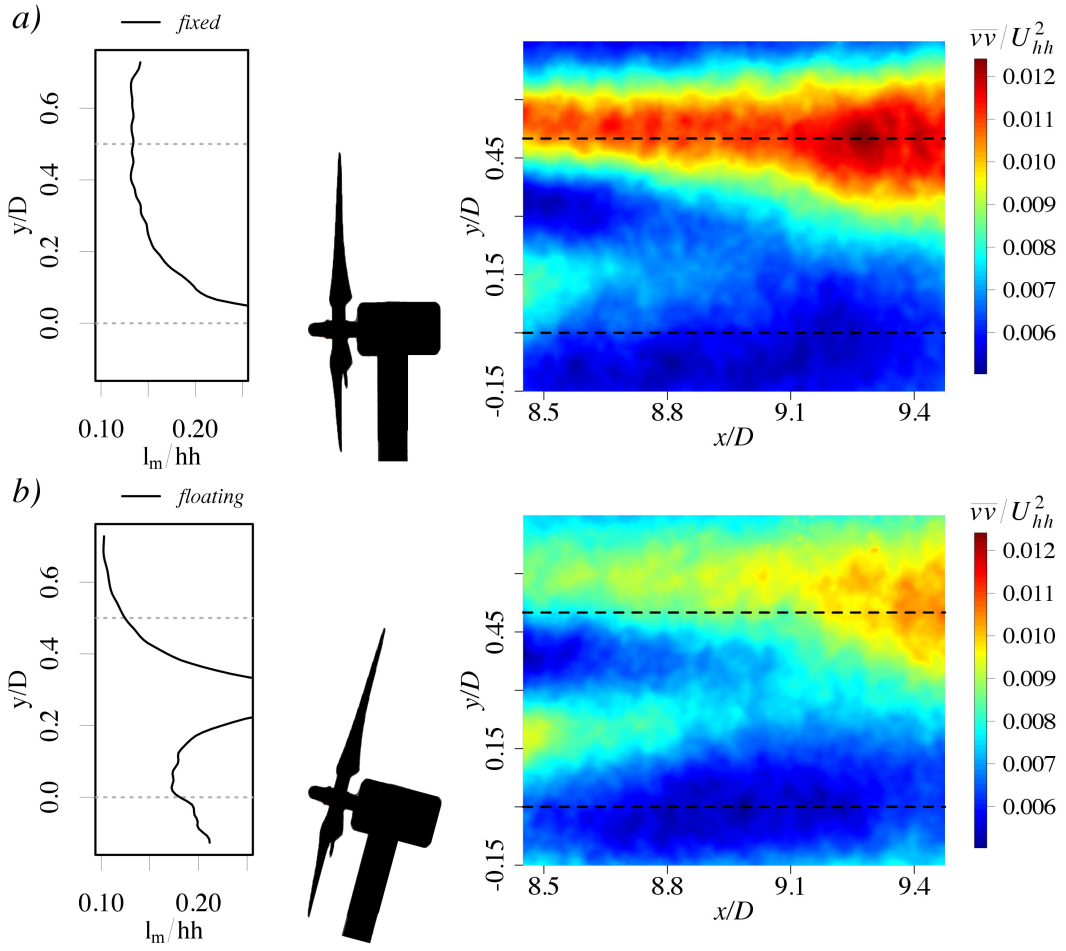

Abbildung 30: Contours of $\overline{vv}/U_{hh}^2$ for near wakes of turbine T2 for the fixed (a) and floating (b) case.

In Figure 31, contours of the normalized Reynolds shear stress $\overline{uv}/U_{hh}^2$ are presented, which is the quantity connected to ν_t and l_m. For the fixed case, the highest negative values of $\overline{uv}/U_{hh}^2$ are found at a height around top tip with a peak of -0.010 at a distance of $x/D = 9.25$ in the wake of T2. From $y/D = 0.15$ - 0.45, a jet-like section of lower $\overline{uv}/U_{hh}^2$ is present. In general, $\overline{uv}/U_{hh}^2$ increases with decreasing height and becomes positive below $y/D = 0.075$. In the floating case, the shear stress has a lowered contribution in magnitude at top tip compared to the fixed case. The stress is shifted upwards due to the pitch motion of the turbine and takes positive values for $y/D < 0.125$.

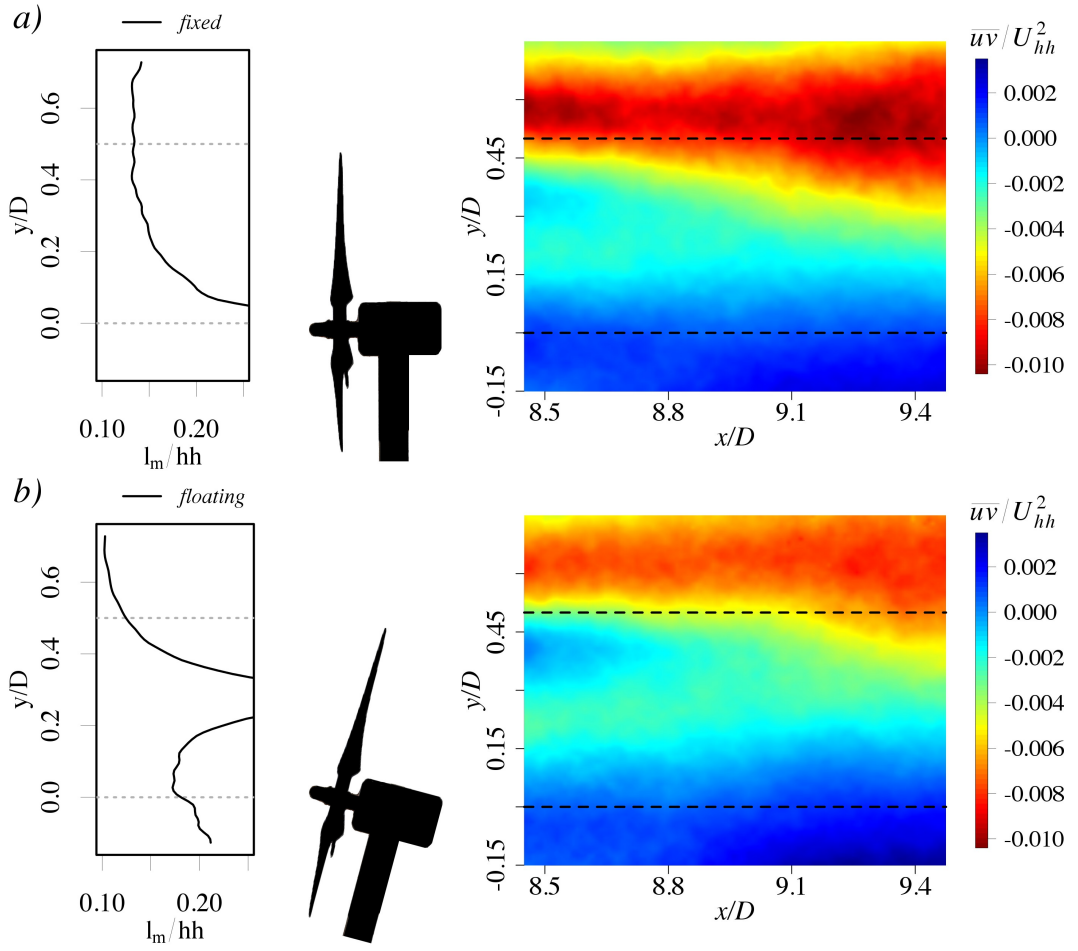

Abbildung 31: Contours of $\overline{uv}/U_{hh}^2$ for near wakes of turbine T2 for the fixed (a) and floating (b) case.

The differences in fluctuations in streamwise and vertical direction between the fixed and floating case are pronounced. As in U/U_{hh} the Reynolds stress $\overline{uu}/U_{hh}^2$ is attenuated, indicating that the oscillatory motion of the turbine is damping the fluctuations. This is also the case for the vertical fluctuations, even though V/U_{hh} is strongly increased, when compared to the fixed case. The lower incoming mixing length in the floating case reduces $\overline{vv}/U_{hh}^2$ in the shear layer, which is up to 40% lower than for the fixed case and is also represented in the differences to l_m in the fixed case. The peak in the mixing length for the floating case is weakly represented in increased normal stresses at $y/D = 0.13$ - 0.3 behind the hub. But the increase is much smaller when compared to the increase of l_m/hh in the floating case.

Above top tip, the ratio of l_m for the fixed and floating case coincides with the ratio of the shear stress in the shear layer, indicating that l_m captures its behavior. Also, l_m increases with decreasing height and has its maximum at the location where the stress changes sign to positive values. Overall, a relation between increasing

mixing length in the inflow and a trend of the shear stress towards zero or positive values is observed below top tip, which is the opposite relation above top tip.

In general, the ability of the turbine to follow the flow reduces fluctuations in the floating case. This potentially leads to reduced fatigue loads in a wind farm configuration, when compared to classical bottom fixed wind turbines.

Flux and production

Results for the turbulence production and mean kinetic energy flux are shown in Figures 32 and 33. These quantities were shown to be important for the recovery of the wake [9]. Figure 32 shows contours of the turbulence production term P_{12} = -$\overline{uv}\frac{\partial U}{\partial y}$. For the fixed case, the production is up to three times higher at top tip and above when compared to the floating case. The production drops drastically below top tip for both cases and its development in the floating case has an upwards tendency when compared to the fixed case. The overall higher production for the fixed case coincides well with the overall higher mixing length and the highest eddy viscosity.

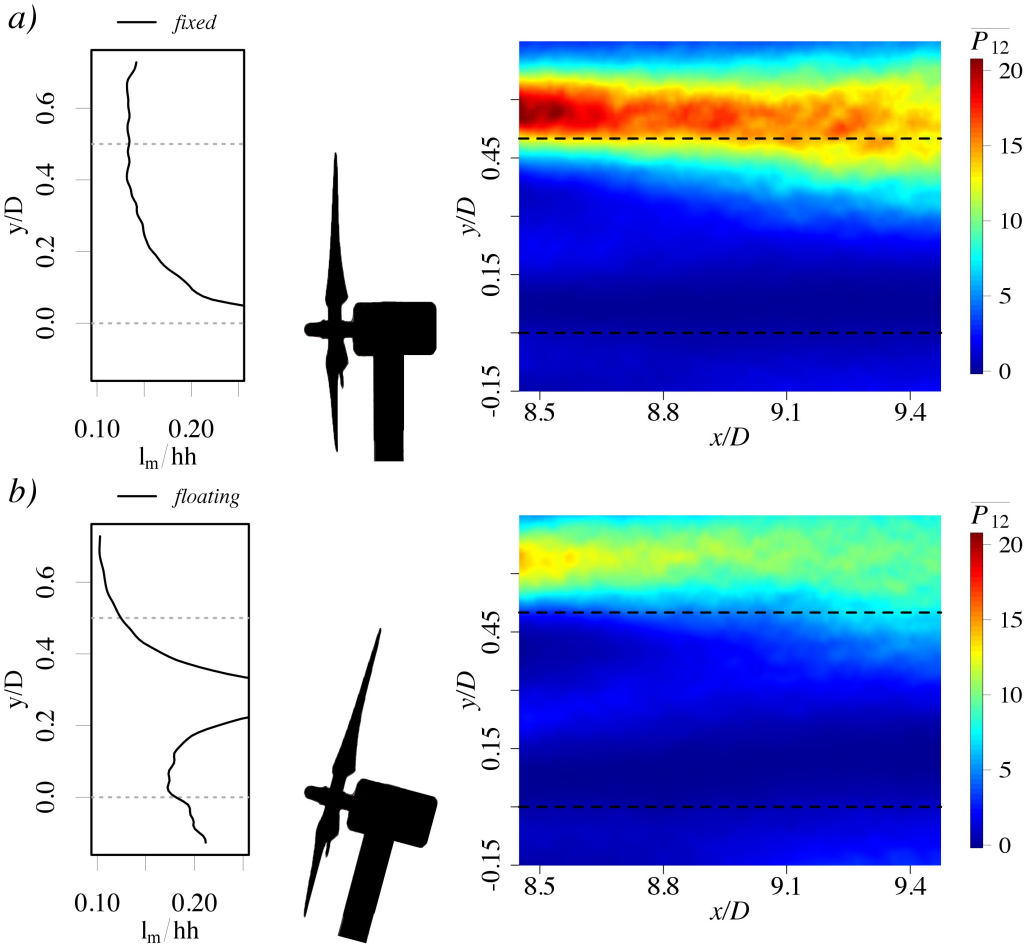

Abbildung 32: Contours of $P_{12} = -\overline{uv}\frac{\partial U}{\partial y}$ for near wakes of turbine T2 for the fixed (a) and floating (b) case.

In figure 33, near wake contours of the mean kinetic energy flux for the fixed and floating case are presented. For the fixed case, the flux is highest in the shear layer above top tip. The high vertical flux above top tip close to the turbine evolves to higher flux with increasing downstream distance. Below $y/D = 0.4$-0.3 the flux drops to zero and becomes in part even negative below hub height.

For the floating case, the flux is also highest above top tip, but the flux is up to 40% smaller when compared to the fixed case. In addition, the flux is shifted upwards due to the motion of the turbine in the floating case. Below the shear layer, the flux develops towards zero and a higher contribution of negative flux is observed below hub height.

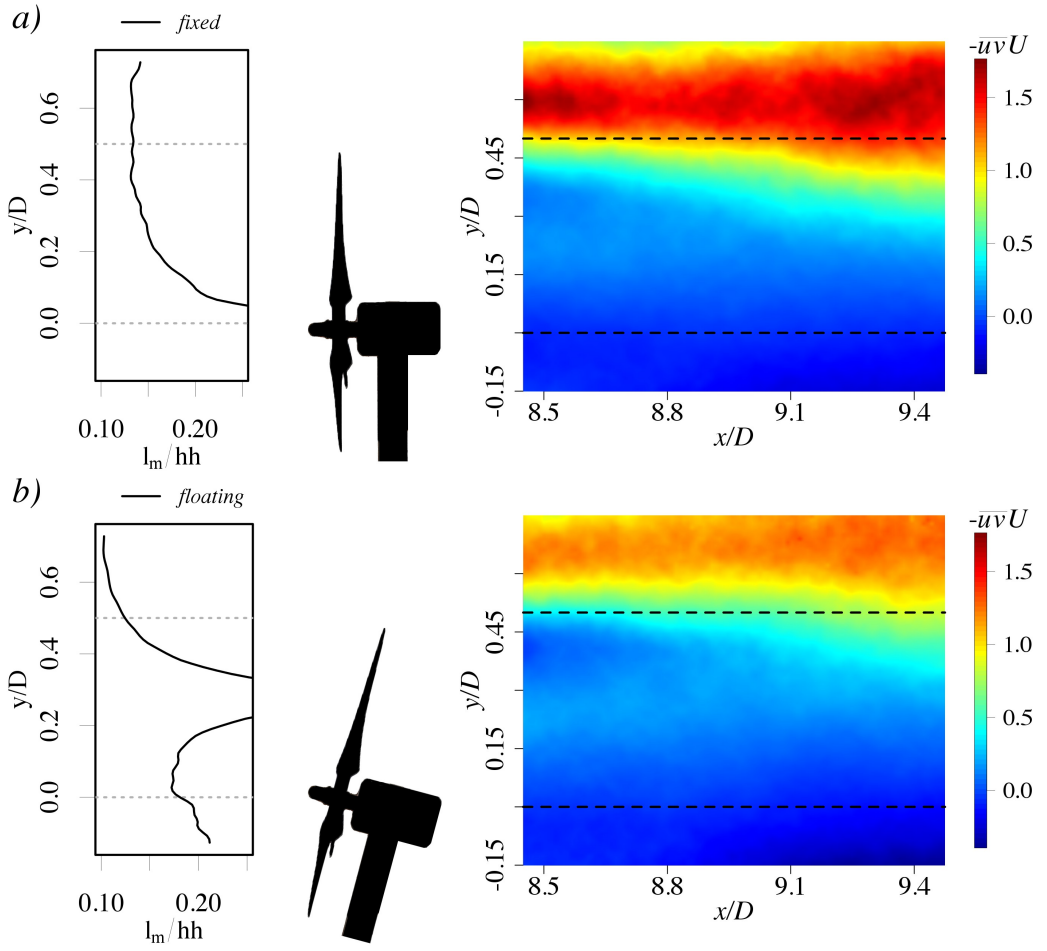

Abbildung 33: Contours of the flux $-\overline{uv}U$ for near wakes of turbine T2 for the fixed (a) and floating (b) case.

The change in mixing length in the shear layer results in a strong change of the production and flux in the shear layer of the near wake. The strong mixing in the inflow for both cases represented by the peaks in l_m/hh do not cause a strong change in the production and flux. This is due the presence of the turbines nacelle and rotating blades, which dominate the flow characteristics in the near wake. The reduced turbulence production and kinetic energy flux in the floating case indicates a lower entrainment of kinetic energy from above, which is seen in the reduced streamwise velocity component.

3.5 Conclusions

Wind tunnel experiments were performed to characterize the far wake of a fixed and oscillating model wind turbine as the inflow for the downwind turbine. Furthermore, its influence on the flow characteristics in the near wake. Wake to wake interactions

were described calculating eddy viscosity and mixing length for the inflow of a downwind turbine and statistical quantities for its wake.

Eddy viscosity was computed using the linear relation between the Reynolds shear stress and strain rate tensor. A clear trend for the eddy viscosity was found with decreasing ν_t for decreasing opposing force on the flow, i.e. when compared to the fixed turbine, eddy viscosity becomes smaller for the deflecting wind turbine and even smaller for the freestream inflow.

Vertical profiles of the mixing length were calculated from measured data, where more evident differences were found, since l_m is strongly dominated by the strain rate. The fixed turbine causes an increase in turbulent mixing by having an increased drag on the flow due to its rigidity. This effect is reduced for the floating turbine due the additional degree of freedom and hence its ability to follow fluctuations in the flow.

The influence of l_m on the near wakes Reynolds stresses and turbulence production is clearly visible in the shear layer above top tip of the turbine, where the fluctuations decreased in magnitude as the mixing length decreased. This connection is less evident below the shear layer, since the near wake characteristics are driven by a combination of the incoming turbulent flow, effects imposed by the nacelle, rotation of the rotor and the oscillatory motion of the turbine in the floating case.

The ability of the turbine to move with the flow absorbs turbulent fluctuations as seen in the Reynolds stresses. The oscillatory motion of the turbine is damping the vertical fluctuations even though the mean vertical component V/U_{hh} is significantly increased, when compared to the fixed case. Moreover, it attenuates the vertical mean kinetic energy flux and turbulence production, which is a combined effect of damped shear stress and shifted vertical gradient of the streamwise velocity. This suggests a suppressed entrainment of kinetic energy, which results in a reduced mean streamwise velocity as it is observed in the experiment.

The oscillatory motion of T2 is reduced when compared to the oscillation of T1, which would reduce the fatigue loads introduced by the dynamics. In addition to the deflected wake fluctuations, the loads of the floating turbine T2 will be reduced than for the fixed T2.

In total, the pitching motion of the turbine leads to the need of longer distances between floating turbines in a farm, to allow for a better recovery of the wake to achieve the same power production, as for bottom fixed turbines. But due to its ability to damp fluctuations, floating turbines are expected to benefit in terms of fatigue loads. Therefore, the oscillatory motion of the floating turbine leads to an optimization problem, where the stiffness of the turbine and the arrangement of the

farm has to be such that the loads are minimized while the power is maximized.

Literaturverzeichnis

[1] A. Henderson, D. Witcher, C. Morgan, Floating support structures enabling new markets for offshore wind energy, Proceedings of the EWEC.

[2] N. Hamilton, R. B. Cal, Anisotropy of the Reynolds stress tensor in the wakes of wind turbine arrays in Cartesian arrangements with counter-rotating rotors, Physics of Fluids 27 (1) (2015) 015102. doi:10.1063/1.4903968.

[3] N. Hamilton,M. Melius, R. Cal, Wind turbine boundary layer arrays for Cartesian and staggered configuration-Part I, flow field and power measurements, Wind Energy 18 (2) (2014) 277–295. doi:10.1002/we.1697.

[4] N. Hamilton, M. Tutkun, R. Cal, Wind turbine boundary layer arrays for Cartesian and staggered configuration-Part II, low-dimensional representations via the proper orthogonal decomposition, Wind Energydoi:10.1002/we.

[5] P. E. Hancock, F. Pascheke, Wind-Tunnel Simulation of the Wake of a Large Wind Turbine in a Stable Boundary Layer: Part 2, the Wake Flow, Boundary-Layer Meteorology 151 (1) (2014) 23–37. doi:10.1007/s10546-013-9887-x.

[6] H. Hu, Z. Yang, P. Sarkar, Dynamic wind loads and wake characteristics of a wind turbine model in an atmospheric boundary layer wind, Experiments in Fluids 52 (5) (2012) 1277–1294. doi:10.1007/s00348-011-1253-5.

[7] N. Hamilton, H. Suk Kang, C. Meneveau, R. Bayoán Cal, Statistical analysis of kinetic energy entrainment in a model wind turbine array boundary layer, Journal of Renewable and Sustainable Energy 4 (6) (2012) 063105. doi:10.1063/1.4761921.

[8] L. P. Chamorro, F. Porté-Agel, Turbulent Flow Inside and Above a Wind Farm: A Wind-Tunnel Study, Energies 4 (12) (2011) 1916–1936. doi:10.3390/en4111916.

[9] R. B. Cal, J. Lebrón, L. Castillo, H. S. Kang, C. Meneveau, Experimental study of the horizontally averaged flow structure in a model wind-turbine array

boundary layer, Journal of Renewable and Sustainable Energy 2 (1) (2010) 013106. doi:10.1063/1.3289735.

[10] P. E. Hancock, F. Pascheke, S. Zhang, Wind Tunnel Simulation ofWind Turbine Wakes in Neutral, Stable and Unstable Offshore Atmospheric Boundary Layers, Vol. 2 of Research Topics in Wind Energy, Springer Berlin Heidelberg, Berlin, Heidelberg, 2014. doi:10.1007/978-3-642-54696-9.

[11] W. Zhang, C. D. Markfort, F. Porté-Agel, Wind-Turbine Wakes in a Convective Boundary Layer: A Wind-Tunnel Study, Boundary-Layer Meteorology 146 (2) (2013) 161–179. doi:10.1007/s10546-012-9751-4.

[12] L. Lignarolo, D. Ragni, C. Krishnaswami, Q. Chen, C. Simão Ferreira, G. van Bussel, Experimental analysis of the wake of a horizontal-axis wind-turbine model, Renewable Energy 70 (2014) 31–46. doi:10.1016/j.renene.2014.01.020.

[13] W. Tian, A. Ozbay, H. Hu, Effects of incoming surface wind conditions on the wake characteristics and dynamic wind loads acting on a wind turbine model, Physics of Fluids 26 (12) (2014) 125108. doi:10.1063/1.4904375.

[14] W. Zhang, C. D. Markfort, F. Porté-Agel, Near-wake flow structure downwind of a wind turbine in a turbulent boundary layer, Experiments in Fluids 52 (5) (2011) 1219–1235. doi:10.1007/s00348-011-1250-8.

[15] M. Khosravi, P. Sarkar, H. Hu, An Experimental Investigation on the Performance and the Wake Characteristics of a Wind Turbine Subjected to Surge Motion, 33rd Wind Energy Symposium (June) (2015) 1–18. doi:10.2514/6.2015-1207.

[16] T. Sant, D. Bonnici, R. Farrugia, D. Micallef, Measurements and modelling of the power performance of a model floating wind turbine under controlled conditions, Wind Energy 18 (5) (2015) 811–834. doi:10.1002/we.1730.

[17] D. Micallef, T. Sant, Loading effects on floating offshore horizontal axis wind turbines in surge motion, Renewable Energy 83 (2015) 737–748. doi:10.1016/j.renene.2015.05.016.

[18] T. Sebastian, M. Lackner, Characterization of the unsteady aerodynamics of offshore floating wind turbines, Wind Energy (March 2012) (2012) 339–352. doi:10.1002/we.

[19] M. Calaf, C. Meneveau, J. Meyers, Large eddy simulation study of fully developed wind-turbine array boundary layers, Physics of Fluids 22 (1) (2010) 015110. doi:10.1063/1.3291077.

[20] S. Rockel, E. Camp, J. Schmidt, J. Peinke, R. Cal, M. Hölling, Experimental Study on Influence of Pitch Motion on the Wake of a Floating Wind Turbine Model, Energies 7 (4) (2014) 1954–1985. doi:10.3390/en7041954.

[21] S. B. Pope, Turbulent Flows, Cambridge University Press, 2000.

[22] D. Poggi, A. Porporato, L. Ridolfi, The Effect of Vegetation Density on Canopy Sub-Layer Turbulence, Boundary-Layer Meteorology 111 (3) (2004) 565–587. doi:10.1023/B:BOUN.0000016576.05621.73.

[23] J. Finnigan, Turbulence in plant canopies, Annual Review of Fluid Mechanics 32 (2000) 519–571. doi:10.1146/annurev.fluid.32.1.519.

[24] K. Bai, C. Meneveau, J. Katz, Near-Wake Turbulent Flow Structure and Mixing Length Downstream of a Fractal Tree, Boundary-Layer Meteorology 143 (2) (2012) 285–308. doi:10.1007/s10546-012-9700-2.

[25] R.-E. Keck, D. Veldkamp, H. A. Madsen, G. Larsen, Implementation of a Mixing Length Turbulence Formulation Into the Dynamic Wake Meandering Model, Journal of Solar Energy Engineering 134 (2) (2012) 021012. doi:10.1115/1.4006038.

[26] J. Westerweel, F. Scarano, Universal outlier detection for PIV data, Experiments in Fluids 39 (6) (2005) 1096–1100. doi:10.1007/s00348-005-0016-6.

[27] R. Theunissen, a. Di Sante, M. L. Riethmuller, R. a. Van Den Braembussche, Confidence estimation using dependent circular block bootstrapping: Application to the statistical analysis of PIV measurements, Experiments in Fluids 44 (4) (2008) 591–596. doi:10.1007/s00348-007-0418-8.

[28] M. Raupach, R. Shaw, Averaging procedures for flow within vegetation canopies, Boundary-Layer Meteorology 22 (1) (1982) 79–90. doi:10.1007/BF00128057.

[29] M. Raupach, J. Finnigan, Y. Brunei, Coherent eddies and turbulence in vegetation canopies: the mixing-layer analogy, Boundary-Layer Meteorology 78 (3-4) (1996) 351–382. doi:10.1007/BF00120941.

[30] D. Poggi, G. Katul, J. Albertson, A Note On The Contribution Of Dispersive Fluxes To Momentum Transfer Within Canopies, Boundary-layer meteorology 111 (3) (2004) 615–621. doi:10.1023/B:BOUN.0000016563.76874.47.

[31] D. Poggi, G. Katul, J. Albertson, Momentum Transfer and Turbulent Kinetic Energy Budgets within a Dense Model Canopy, Boundary-Layer Meteorology 111 (3) (2004) 589–614. doi:10.1023/B:BOUN.0000016502.52590.af.

4 Dynamic wake development of a floating wind turbine in free pitch motion subjected to turbulent inflow generated with an active grid

Development of wake turbulence of a floating wind turbine model under low and high turbulence inflow was investigated in comparison to the wake of a bottom fixed turbine. In wind tunnel experiments, two inflow conditions were generated using an active grid and the wakes of the model wind turbines were measured using a rake of 16 hot-wires, at downstream positions from one to seven rotor diameters. The flow was analyzed using statistical, spectral and spatial analysis. Under low turbulence inflow, the turbine type has highest impact on the wake, where structures created at the blade tips define substantially characteristics of the wake. Formation of a correlated tip and root vortices, that is found for the fixed turbine, is inhibited by the floating turbine. Under high turbulence inflow, the turbine type plays a subordinated role. Tip vortices are destabilized by large structures created with the active grid, that persist in the wake. Further analysis using proper orthogonal decomposition reveals more complex pattern under high turbulent inflow, that contain high percentage of turbulent kinetic energy, when compared to the low turbulent inflow, where the wake is composed by local point-wise contributions to the turbulent kinetic energy.

4.1 Introduction

With increasing demand in renewable energy resources and more specifically wind energy, offshore wind farms are installed due to steady wind conditions [20]. For areas with water depth >50 m, classical bottom fixed offshore turbines are not feasible and floating wind turbines are considered as a potential solution. Wind turbines positioned on floating platforms are subject to additional degrees of freedom, when compared to a bottom fixed turbine. The additional motion of a floating wind turbine has an impact on the wake development, thus on the inflow of further turbines within a wind farm [13, 21, 22]. Numerical experiments were performed in Refs. [10–12, 15, 27] to investigate structural and aerodynamic effects of platform motions of floating offshore wind turbines. FAST code for classical turbines was expanded with hydrodynamic wave-body interaction covering hydrodynamic damping and wave excitation of the platform. A comparison of three concepts of floating platforms with land-based turbines showed an overall increase of loadings on all turbine components due to the floating platform. Wind tunnel experiments with model wind turbines were carried out on the influence of isolated degrees of freedom on performance and

wake of the turbines under same inflow conditions (cf. Refs. [21, 22, 25]). For a streamwise oscillating turbine, a vertical deflection in the mean streamwise direction and an increase in the mean vertical flow was found, accompanied by an upwards shift/deflection in space of the turbulent kinetic energy. Due to that shift, the flow containing most of the turbulent kinetic energy is displaced above a downwind turbine at 6-7D in the wake, thus experiencing reduced fluctuations in the inflow. For a turbine subjected to surge motion, higher power output and reduced thrust loads were measured on average, as well as longer wake persistence due to reduced shear stresses [13].

Herein, the dynamic wake development of a floating wind turbine model under two different inflow conditions is investigated and compared to the wake of a bottom fixed turbine model. Therefore wind tunnel experiments were performed, where low and high turbulence inflow conditions, respectively referred to as "passiveänd "activeïnflow, were generated using an active grid. In Section 4.2 the setup of the active grid, the hot-wire rake and both turbines is described. Further, turbulent characteristics of the two inflow conditions are presented. Results for the wake are presented in Section 4.3, where the mean flow and turbulence intensities are shown for selected measurement positions. Also, different properties of the fluctuations are investigated using probability density functions (pdf) as well as spectral analysis. Spatial insights into structures of the wake are gained by means of spatial correlations. In Section 4.4 the compositions of wake flows are analyzed by means of proper orthogonal decomposition (POD) and the contained turbulent kinetic energy per mode, to find a low dimensional representation of the flow and allow for a deeper understanding of the different flow conditions and turbine types. Drawn conclusions on the investigations are given in Section 4.5.

Proper orthogonal decomposition

Proper orthogonal decomposition (POD) is used to identify coherent structures in the flow by projecting the flow onto an orthogonal basis and weighting the orthogonal functions by its contribution to the total energy of the flow in a descending order, which is represented by the corresponding eigenvalues [4, 9].
The basis functions $\phi(x)$ for the best representation of the flow in terms of kinetic energy are obtained by maximizing the expression

$$\frac{\overline{\langle u(x,t), \phi(x)\rangle^2}}{\langle \phi(x), \phi(x)\rangle} \tag{31}$$

where the overline indicates temporal averaging and the parenthesis $\langle\rangle$ indicate

an inner product of two functions $\langle f, g\rangle = \int_a^b f(x)g(x)dx$ or in a discretized case $\sum_{k=1}^{N} u(x_k, t)\phi(x_k)$, with x_k being a discrete measurement position. This problem is shown to be equivalent to the eigenvalue problem (cf. Refs [4, 6, 9])

$$\sum_j R_{i,j}\phi(x_j) = \lambda_i \phi(x_i), \tag{32}$$

with $R_{i,j} = \overline{u(x_i, t)u(x_j, t)}$ being the covariance tensor and λ_i the eigenvalues to the eigenfunctions or POD eigenmodes $\phi(x_i)$, respectively. Solving the eigenvalue problem yields the eigenvalues and corresponding POD eigenmodes. The reconstructed field is given as a linear combination of the eigenfunctions by,

$$u(x_i, t)_{recon} = \sum_{n=1}^{N} a_{(n)}(x_i, t)\phi(x_i)_{(n)}, \tag{33}$$

with n giving the mode-number and the obtained weighting coefficients,

$$a_{(n)}(t) = \sum_{i=1}^{N} u(x_i, t)\phi(x_i)_{(n)}, \tag{34}$$

of the orthogonal eigenfunctions [5].
In the context of wind energy PODs have been used successfully by Saranyasoontorn *et al.* [26] to characterize a simulated inflow field with 36 nodes distributed over a rotor area of a 600 kW two bladed wind turbine and investigate the statistics of blade and tower bending moments. Only few POD modes were found to be necessary to describe main characteristics of the inflow field and resulting loads. The POD was applied by Bastine *et al.* on the wind turbine wake data obtained from large eddy simulations [1, 2], where it was shown that the basic dynamics are well described by the first few modes, which describe larger scales that - typically for turbulent flow - contain most of the kinetic energy. Hamilton *et al.* [7] applied the snapshot POD on data obtained from wind tunnel experiments on a small scale wind farm using stereoscopic particle image velocimetry. It was found that the content of kinetic energy per mode is considerably changing with measurement location and with presence of turbine. In the wake of a turbine, turbulent kinetic energy is shifted to intermediate and high mode numbers, when compared to the undisturbed inflow.

4.2 Experimental Setup

Wind tunnel

Experiments were performed in the acoustic wind tunnel at the University of Oldenburg (cf. Figure 34). It is a low turbulence closed-circuit wind tunnel with a cross

section of 0.8 m × 1 m and a test section of 2.6 m in length.

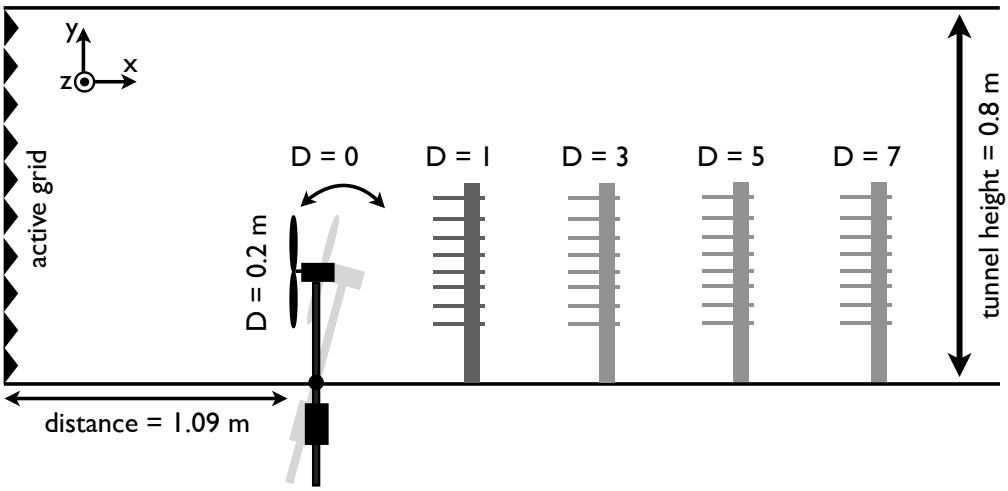

Abbildung 34: Closed-loop wind tunnel setup with the active grid, model wind turbine and hot-wire rake at measurement positions $x/D = 0$ to $x/D = 7$. *(Schematic not to scale.)*

Measurements with two different turbulent inflow conditions are performed: one with a static active grid used as passive grid with a low turbulence level (passive inflow) and one with highly turbulent inflow conditions (active inflow) imposed by motions of the axes of the active grid (cf. Fig. 35). Details on the inflow characteristics are discussed in Section 4.2.

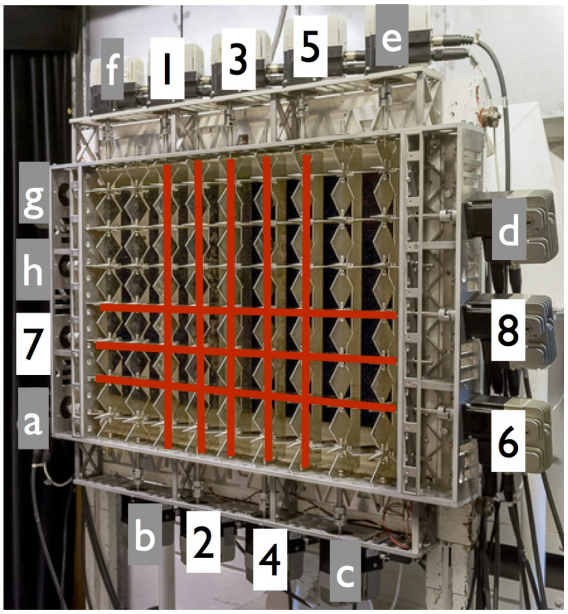

Abbildung 35: Image of the active grid with individually controlled axes in an opened wind tunnel. A phase shift between the inner axes (1-8) and the outer axes (a-h) is introduced, to compensate changes in the mean blockage.

The grid consists of 7 horizontal and 9 vertical axes with flaps. Each axis is individually controlled with stepper motors. The angle of attack between the flow and the flaps is changed over time following a defined excitation protocol, which allows for statistically reproducible inflow conditions. Further details on the grid can be found in Refs. [14, 31]. First, both inflow conditions were characterized measuring the inflow profiles with a rake of 16 hot-wires. Then, a classical bottom fixed model wind turbine and a model wind turbine allowed to freely oscillate in downstream direction, i.e., in free pitch motion, was positioned in the wind tunnel and subjected to the different inflow conditions. Wakes of both turbines were measured with the hot-wire rake at downstream positions from 1 to 7 rotor-diameters. The wake development in terms of mean velocity $\overline{u}$, turbulence intensity $Ti = \sqrt{\overline{(u-\overline{u})^2}}/\overline{u}$, distributions of fluctuations, power density spectra and cross-correlations are compared.

Hot-wires

A hot-wire rake with 16 1D hot-wires (*Dantec 55P16*) of 1 mm length was used for flow measurements. Two Dantec multichannel CTA 54N80 were used to operate the hot-wires, with an low-pass filter set at 10 kHz. The data acquisition consists of an 18 bit A/D-converter (*NI 6281*) with a sampling frequency of 20 kHz.

The hot-wires were calibrated in the wind tunnel with the active grid installed and operated in an open configuration with low turbulence intensity. To assure that

turbulence generated by the grid was well mixed and did not influence the calibration, the rake was positioned at the end of the closed test section. Two Prandtl tubes connected to pressure sensors were used to measure the mean velocity over a time period of 120 s to achieve converged means for pressure and hot-wire sensors. The velocity range for the calibration was 0.6 m/s - 13.7 m/s in steps of 1 m/s. After all measurements were taken a second calibration was performed following same procedure, which matched the first calibration, so that drift of the hot-wires can be excluded.

The hot-wire arrangement is shown in figure 36 and was designed to cover one quadrant of the rotor area and a vertical profile at the centerline of the turbine.

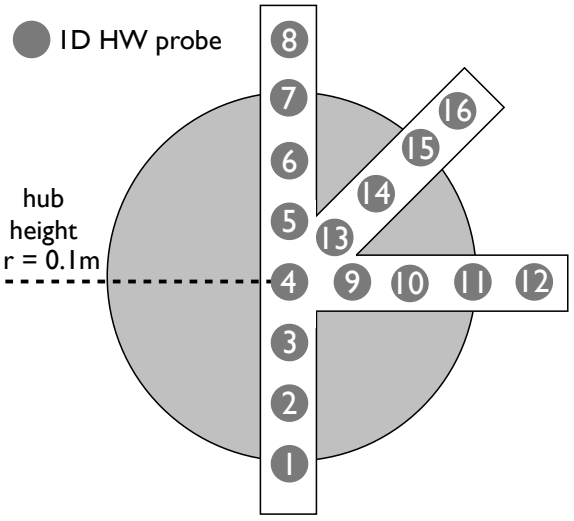

Abbildung 36: Hot-wire rake with the arrangement of the hot-wires and corresponding hot-wire numbers. Schematic not to scale.

The grey area respresents the rotor area of the later installed turbine, where hot-wire 4 is set to hub height of the later installed turbine. The spacing between the hot-wires is 33 mm. Hot-wires 8, 12 and 16 are outside of the rotor area to account for effects due to expansion of the wake.

Model wind turbine

The model wind turbine used in the experiments has a rotor diameter D of 0.2 m, a nacelle with a diameter of 28 mm and a cylindric tower with a diameter of 16 mm. Hub height was set to 0.24 m. The blockage ratio of rotor area to wind tunnel cross-section is below 4% so blockage effects can be neglected [28]. To allow for observations of introduced effects by an isolated degree of freedom, here the pitching motion, the turbine is mounted in a gimbal support which allows for oscillations

in streamwise direction and is stabilized by a cylindrical weight. Typically, floating wind turbines are stabilized by catenary wires; not considered here for simplification purposes. The oscillating turbine is referred to as floating turbine. The stabilizing weight of 650 g was positioned at the tower below the gimbal support in such way that the turbine is allowed to oscillate with respect to the incoming flow with a mean inclination angle of 15° and a standard deviation of 0.1° under low turbulence and a mean inclination angle of 14.4° with a standard deviation of 2.6° under high turbulence inflow conditions. The operational point of the turbine was set using a fixed ohmic resistor for all measurements. Averaged tip speed ratios $\lambda = \frac{\omega R}{u}$ with ω being the rotational frequency, power coefficients $c_p = \frac{torque \cdot \omega}{power_{wind}}$ and corresponding standard deviations are given for the fixed and floating turbine in Table 3. The power in the floating case was corrected for the reduced area due to the mean inclination. Further details on the power measurement are found in [21].

	low turbulence		**high turbulence**	
	fixed	floating	fixed	floating
c_p	28 % ± 1 %	27 % ± 1	26 % ± 5 %	22 % ± 5 %
λ	6.2 ± 0.2	5.8 ± 0.2	5.9 ± 0.6	5.2 ± 0.5

Tabelle 3: Operational conditions of the model wind turbine: mean power coefficient $c_p \pm$ its standard deviation; mean tip speed ratio $\lambda \pm$ its standard deviation

The performance of the turbine is close to what is expected for full scale turbines. Under high turbulent conditions the variation in power is high, due to high variation in the inflow, for the floating turbine c_p and λ are reduced, which is due to the motion of the turbine and that the turbine is not actively controlled. The tip speed ratio, which is an important parameter for the impact of the turbine on wake characteristics [23], matches well with full scale experiments. No scaling of Reynoldsnumber and Froud-scaling are applied, but due to the matching λ and the direct comparison of the floating turbine to a fixed turbine, general implications can be deduced from the results.

Inflow conditions

The experiments were performed under two different turbulent inflow cases. In the passive case, the grid was opened, i.e., all flaps of the active grid were fixed parallel to the flow. In the active case, one excitation protocol for all axes was used following Weitemeyer *et al.* [31], where the angles of attack α between the flow and flaps were changed with 2 Hz and were Gaussian distributed with a mean angle of attack $\overline{\alpha} = 0°$, i.e., parallel to the flow, and standard deviation $\sigma_\alpha = 25°$. The active grid protocol

is designed to generate a highly turbulent inflow with a wide range of fluctuations. Changes in mean blockage of the active grid were compensated by introducing a phase shift of 90° between the inner axes (Fig. 35, axes 1-8) and the outer axes (Fig. 35, axes a-h), such that for both cases the incoming velocity converged to 5.9 m/s over 10 minutes, when averaged over all 16 hot-wires. In the active case, the hot-wire measurements were triggered by a light-barrier sensing the movement of an axis of the active grid to assure reproduced synchronous measurements by repeating the same excitation protocol. Next, flow conditions are characterized at the location where the turbine will be placed. Figures 37a) and 37b) show the mean velocities and the turbulence intensities, respectively, at the inflow location at which otherwise the turbine is present when mounted.

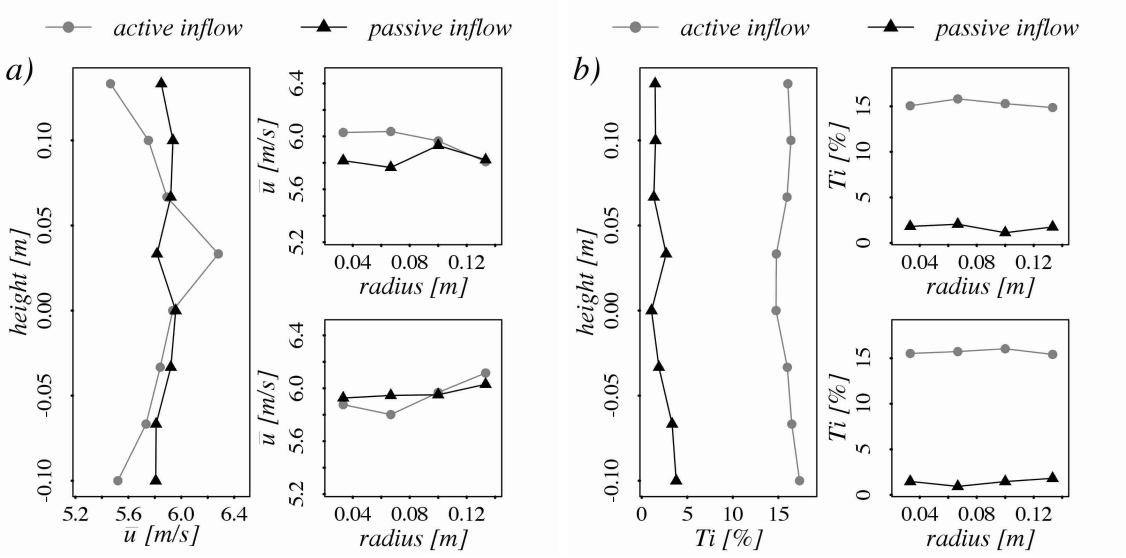

Abbildung 37: Comparison of the active and passive inflow conditions in terms of mean local velocities and turbulence intensities. Referring to, Fig. 36, measurements presented in a) and b) on the left are taken at hot-wire 1-8, on the bottom right plots at hot-wires 9-12 and on the upper right plots at hot-wires 13-16.

Under both inflow conditions, the turbulence intensity is homogeneously distributed over the rotor area, while the overall Ti differ severely between the inflow conditions with 1.8% in the passive and 15.9% in the active case. The inflow conditions were measured twice for each case. The reproducibility of the time signals created with the active grid was measured by calculating the cross-correlation between the time signals of hot-wire $i = 1..16$ for the first and second measurement. The average correlation coefficient was 0.66. This is due to the turbulent nature of the flow, that the high frequency fluctuations are not fully controlled with the active grid and are

not correlated on average. By low-pass filtering the data, the correlation increased to, e.g., 0.76 with a filter frequency of 60 Hz and 0.86 with a filter frequency of 10 Hz. The average deviation in the means between the measurements in the passive case is below 0.2% and for the active case below 2.1% of the mean inflow velocity. The turbulence intensity differs on average by 0.1% in the passive and 0.5% in the active case, resulting in reproducible inflow conditions.

Figure 38 shows averaged power density spectra (psd) of the inflow in the active and passive case measured at the horizontal center of the wind tunnel at a height of 0.24 m at $x/D = 0$. The averaging is performed to reduce the influence of random noise by splitting the time series into slices of 2^{17} (≈ 6.5 s) samples and calculating the psd of each slice, which are then averaged. Assuming Taylor's hypothesis of frozen turbulence as valid [18, 29], the frequencies f are expressed as scales $r = \overline{u}/f$. This does not change the shape of the spectra but simplifies interpretation. Spectra measured at remaining locations in the rotor area show similar trends. The power density spectra for the active case are shifted for clarity.

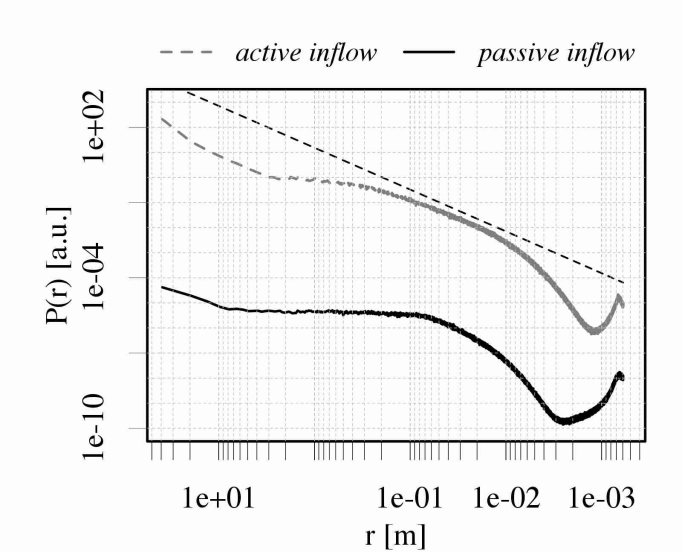

Abbildung 38: Power spectrum density of the active and passive inflow at a height of 0.24 m at $x/D = 0$ D. The power spectrum in the active case was shifted up, to increase clarity.

In the passive case, structures of 6 m to 0.07 m contribute equally to the power and dominate the inflow conditions. The integral length for the passive case is of order 0.01 m to 0.1 m, which is the mesh size of the opened active grid. It is calculated as the integral of the auto-correlation function of the time-series $u(t)$ up to the auto-correlation-value of $1/e$ (cf. Refs [17, 30]) and is commonly interpreted as the largest correlated scale in the flow (cf. Refs. [3, 30]). For scales < 0.07 m the power is

decaying with no clear range with a linear trend to the power.

In the active case, scales > 6 m, which are generated by the active grid, as was shown by Knebel *et al.* [14], contribute significantly to the spectral power of the inflow. The integral length is in the order of 20 m for the active case, i.e., larger correlated structures approach the later installed turbine, when compared to the passive case. A linear range for scales of 0.4 m to scales of 0.01 m, where the energy decay follows a scaling law, is found for the active case. The slope of the linear decay is -1.5, i.e., the energy-decay is close to that found for homogeneous isotropic turbulence. Also, the active inflow conditions are such, that the turbine is affected by small scale turbulence, as it is seen in field measurements [16].

4.3 Results and Discussion

Results of the wake development for the fixed and floating case under passive and active inflow conditions are presented. Flow characteristics at measurement positions above top tip, top tip, hub height and bottom tip are shown. First, the development of mean velocities and turbulence intensities at downstream positions $x/D = 0$ to $x/D = 7$ is presented. Thereafter the probability density functions of the fluctuations are discussed for a deeper insight into the range of fluctuations. Analysis in the frequency domain, using power density spectra, allow the identification of dominant periodicities in the flow and analyze the energy distribution at scales contained in flow, i.e. scaling behavior of the turbulence. Completing the picture, spatial analysis is then performed by means of cross-correlations between all measurement points in the hot-wire rake, that allow to recognize correlated patterns in the flow and analyze their development in dependence on inflow conditions as well as turbine type.

Means and turbulence intensities

Figures 39 a) and 39 b) show the downstream evolution of the mean velocity $\overline{u}$ and the turbulence intensity Ti under active and passive inflow conditions for the fixed and floating turbine measured above top tip (hw 8), top tip (hw 7), hub height (hw 4) and bottom tip (hw 1). Averages are performed over the time series of 594 s and the mean velocities are normalized by the incoming inflow at $x/D = 0$.

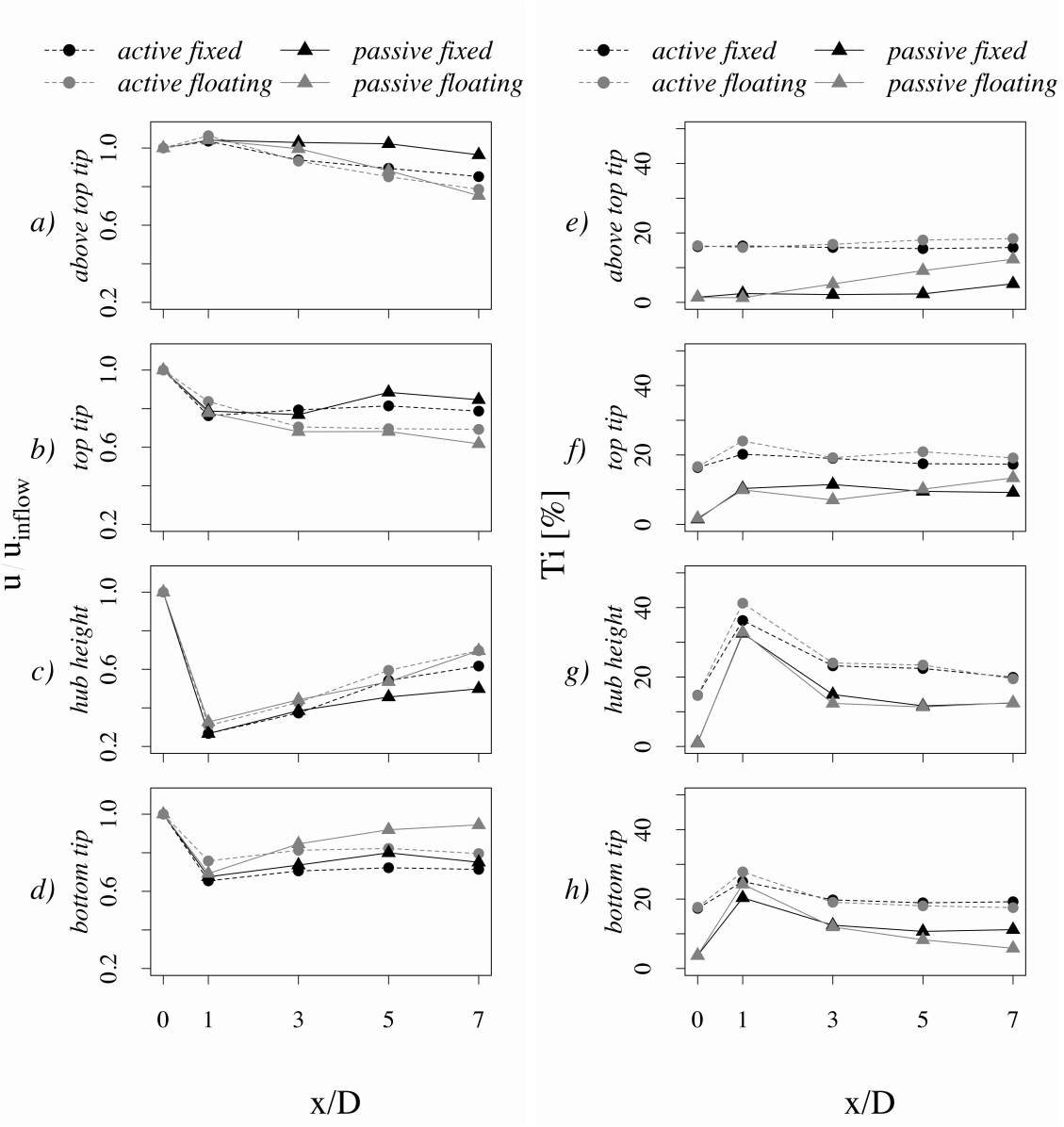

Abbildung 39: Development of the mean velocity $\overline{u}$ and the turbulence intensity Ti for hot-wires above top tip, top tip, hub height and bottom tip for downstream positions $x/D = 0$ to $x/D = 7$.

In Figure 39 a) above top tip, $\overline{u}$ increases to 103%-106% of the free stream velocity at $x/D = 1$ for all cases, which is also found at the remaining out of rotor-plane measurement positions, (hot-wire 12, 16) and indicates a rotor blockage effect, thus a redirection of the flow approaching the rotor area to the surrounding flow. In the passive floating case, a significant decrease to 75% of the undisturbed inflow in the far wake is observed. Under active inflow conditions, $\overline{u}$ is reduced over distance for both turbines, i.e., mean kinetic energy is removed at this height due to enhanced turbulent mixing in the shear layer.

In Figure 39 b) at top tip, the mean velocity decreases by 16%-24% for both inflow conditions and both turbine cases. With increasing distance, the wake in the fixed case recovers faster than for the floating case for both inflow conditions. Substantial differences in $\overline{u}$ are found under passive inflow conditions in the far wake, where $\overline{u}$ is 85% of the undisturbed inflow for the fixed turbine and only 62% for the floating turbine.
At hub height, the velocity decreases below 33% of the incoming flow, for both inflow conditions and both turbine types. With increasing distance the flow recovers up to 70% in the far wake, where for both inflow conditions the wake in the floating case recovers faster than in the fixed case.
At bottom tip in Fig. 39 d), the velocity at $x/D = 1$ is reduced to 65-76% of the undisturbed inflow for all cases. In the passive floating case, the wake recovers continuously from 69% at $x/D = 1$ to 94% at $x/D = 7$. The deficit in the active fixed case is highest and recovers only slowly from 65% at $x/D = 1$ and 71% at $x/D = 7$. For both turbines, the velocity in the wake remains nearly constant over distance under the active inflow condition.

In general, a comparable breakdown in the mean velocities is found for all cases in the near wake, but no clear clustering by turbine type or inflow condition is then observed in the further development of the wake. Thus, the commonly used assumption of rotational symmetry of the wake for wind turbine design is not supported by the data [8, 24], since the local flow velocities in the wake depend strongly on the turbulence of the inflow and the oscillation of the turbine. The far wake recovering for the fixed turbine decreases with decreasing measurement height under active as well as under passive inflow conditions. Differences in the wake recovery between fixed and floating turbine are similar to what was found with PIV measurements in Ref. [21], where the mean velocities were shifted upwards. This effect is observed for different turbulence intensities as well as with a shear layer, which was present in Ref. [21] and without, as in this study. Under highly turbulent inflow conditions as created with the active grid, the influence of the turbine type is mitigated due to enhanced turbulent mixing.

Next the development of the turbulence intensity is presented and discussed. In contrast to the mean velocities, a clear clustering for the inflow conditions is observed for the turbulence intensities. In Figure 39 e) under passive inflow, Ti slightly increases in the far wake to 5% for the fixed case, but significantly for the floating case with a maximum of 12% at $x/D = 7$. Under active inflow conditions, Ti stays approximately constant at 16% - 18% with the higher value for the floating turbine.

At top tip, the turbulence intensity increases in the near wake to 10% under passive and to 20%-24% under active inflow conditions. With increasing downstream distance, a constant offset of 8% is found for the fixed turbine under active inflow conditions in comparison to the passive.
At hub height at $x/D = 1$, Ti increases significantly for both inflow conditions and turbines, being highest in the active case for the floating turbine (cf. Fig. 39 g). This increase is dominated by the enlarged deficit in the mean velocity. At $x/D = 3$, the turbulence intensity is reduced to 24% under active and to 15% under passive inflow conditions for both turbines. This offset of $\sim 9\%$ between the inflow conditions is equal to that observed in the inflow and persists into the far wake.
At bottom tip, the turbulence intensity shows similar trends as at the top tip, being higher for the passive inflow, which is due to the interaction of the flow with the tower.

In contrast to the mean flow, a clear grouping of Ti-development by the inflow conditions is given, being generally higher for the active case. A clear upwards shift in Ti for the floating turbine is observed in the far wake under passive inflow conditions, which is in agreement with PIV measurements in Ref. [21], where the fluctuations are shifted upwards. Under passive inflow conditions, Ti is driven strongly by the rotation of the rotor and with increasing vertical height by the oscillation of the turbine. Under active inflow conditions, the oscillation of the turbine has a minor impact on the Ti and the high level of turbulence is preserved in the wake even with increasing distance, i.e., in the inflow for a downstream turbine. For the inflow of a turbine positioned downstream in a wind-farm configuration, the presence of a turbine - fixed or oscillating - resembles in an increase of Ti, being even higher for inflow conditions with high ambient turbulence intensity.

For a turbine positioned in the far wake of a floating turbine, the upwards-shift of the mean inflow causes shifted loads over the rotor area on average, which has to be considered in the design. Under high turbulence inflow, predictions of mechanical loads for a floating turbine are further complicated by the increased turbulence and in addition the wider variation in the inclination angle of the turbine, which could cause an up and down oscillation of the loads.

Probability density

In Section 3.1 the first and second statistical moment of the distribution of the fluctuations were discussed, being the mean and a normalized standard deviation. In this section a more detailed understanding of the turbulent characteristics of the flow is given by probability density functions, which allow for a deeper quantitative

analysis of the fluctuations in the wake and of the inflow conditions of wind turbines in wind farms. A measure of symmetry of a pdf and its deviation from a Gaussian distribution is given by the third and fourth statistical moment, respectively [19]. The third moment is the skewness $S(u) = \overline{(u-\overline{u})^3}/\sigma_u^3$ and the fourth moment is the flatness $F(u) = \overline{(u-\overline{u})^4}/\sigma_u^4$. A Gaussian distribution has a skewness of 0 and a flatness of 3.

Figure 40 shows probability density functions of the fluctuations $u' = (u - \overline{u})$ under passive and active inflow conditions measured above top tip, top tip, hub height and bottom tip for downstream positions $x/D = 0$, with no turbine installed and $x/D = 1$, $x/D = 5$ for the fixed and floating turbine.

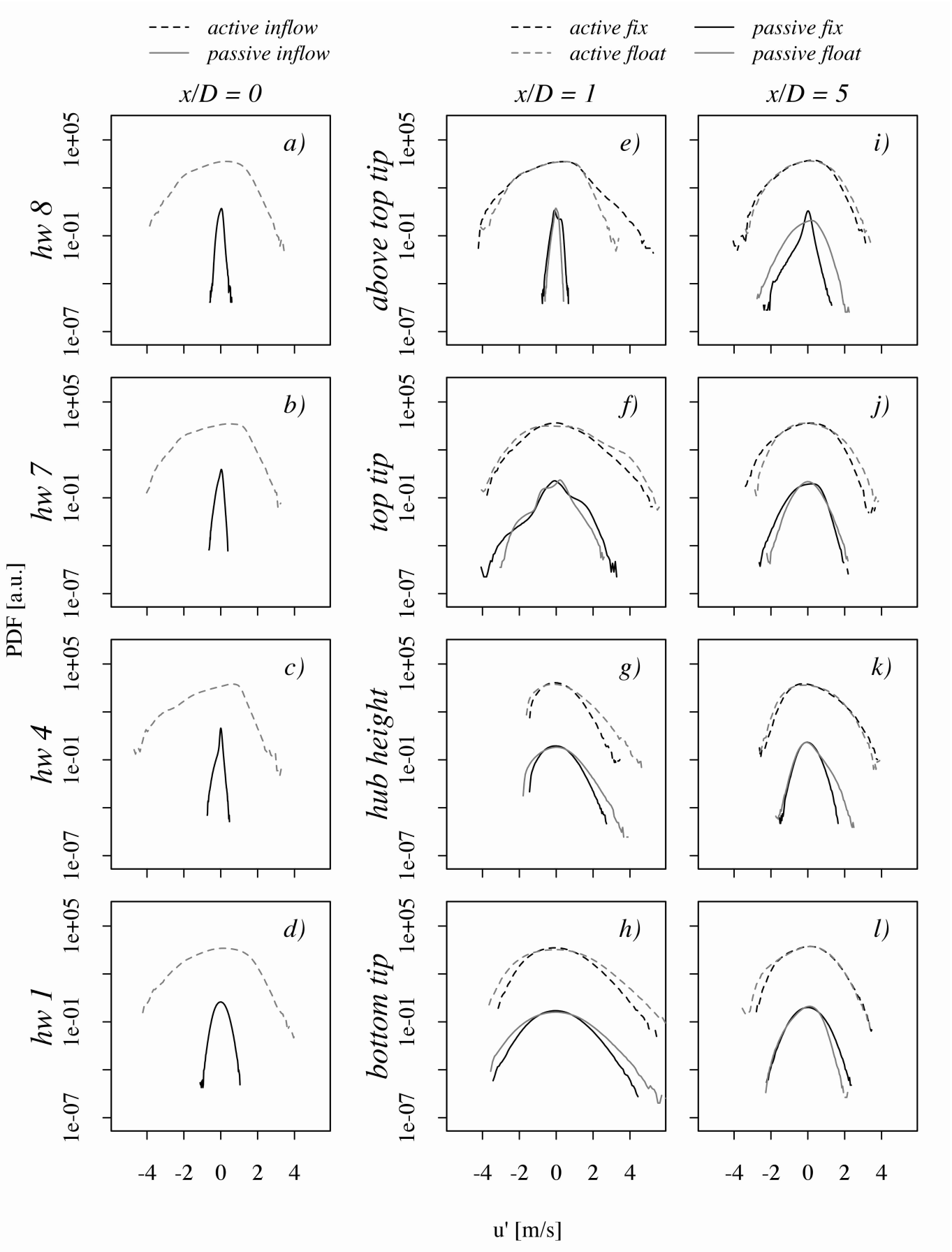

Abbildung 40: Probability density functions of u' measured above top tip, at top tip, hub height and at bottom tip. First column shows the inflow at x/D = 0 D without turbines. Second and third columns for near wake at x/D = 1 D and far wake at x/D = 5 D. The pdfs for the active case are shifted up for enhanced clarity.

In Figure 40 a) to d) for the passive inflow conditions the range of fluctuations is rather limited with maxima of ± 1.2 m/s. The pdfs are negatively skewed with S = -0.5 to -1, i.e., the probability for positive fluctuations is increased and despite of the small turbulence intensity, the distribution is heavy tailed, with the flatness being F = 3.3 - 4.7, thus stronger fluctuations are more likely than for a Gaussian distributed time series. Only at bottom tip, the distribution is symmetric and nearly Gaussian with a skewness of 0.07 and a flatness of 2.9. The active inflow conditions have a drastically higher range of fluctuation from -4.4 m/s to 4 m/s and the distributions are negatively skewed with a skewness of -0.4 to -0.6, while being flatter with F = 2.8 to 2.9, when compared to a Gaussian distribution. The wider range of fluctuations under active inflow conditions is expected to cause strong variations in the performance of the turbines and in the dynamics of the floating turbine, consequently affecting the wake development, thus the performance of downstream turbines.

Next, the top near wake under passive inflow conditions is discussed. Highest impact of the turbine on the fluctuations is found at top tip, where in the fixed case, the range of fluctuations reaches ± 4 m/s and a clear maximum at u' = 0 m/s as well as two saddle points at u' = 0.8 m/s and at u' = -1.6 m/s with an increased probability to higher fluctuations are observed. In the floating case, fluctuations are dampened and the local maxima are shifted to -0.7 m/s and 0.2 m/s, with a pronounced saddle point at u' = -0.3 m/s. The observed maxima in the pdfs are attributed to the periodicities due to the rotations of the rotor and the shed vortices at the blade tips, which have greatest influence at the upper wake.

The near wake under active inflow conditions, has increased probabilities for positive fluctuations with S = -0.4 and F = 3.1 for the fixed turbine, whereas in the floating case the pdf follow the same trend as in the inflow with S = -0.5 and F = 2.8, which is due to the inclination of the turbine and reduced interaction of the flow at the particular height. At top tip the turbine further broadens the range of fluctuations when compared to the inflow, while at the same time a reduction of the asymmetry (S = 0.2) is observed, with the pdf having similar shapes for both turbines. At hub height and bottom tip, the differences of the pdfs between the inflow conditions diminish. For both inflow cases and turbines the distributions are positively skewed (S $\sim$ 0.1 - 0.2) and have a wider range for the floating turbine, being significantly wider at bottom tip.

Generally, the pdfs in the near wake reveal significant differences between the inflow conditions at top tip, where under passive inflow conditions periodically detached structures dominate the turbulent characteristics of the top wake. Under active inflow conditions, the fluctuations are less susceptible to fluctuations created by the rotor

and tip vortices, since the flow is dominated by the surrounding turbulence. At hub height and bottom tip, the turbine type plays a major role for the shape of the pdfs. The presence of bluff bodies, such as the tower, nacelle and rotor dominate the behavior of the fluctuations. The motion of the hub in the floating case results in a broader range of fluctuations.

At $x/D = 5$, the major difference between the turbines is found above top tip under passive inflow conditions, where the pdf for the floating turbine has a four time larger range, when compared to the near wake and is rather symmetric (S = -0.4) as well as closer to a Gaussian distribution ($F = 3.2$). In contrast, the pdf for the fixed turbine is asymmetric (S = -1.5) and strongly heavy tailed ($F = 12.7$). Under active inflow conditions, pdfs resemble same shape as in the inflow, with a reduced skewness of -0.4 in the fixed case to -0.2 in the floating case.

At hub height and bottom tip, pdfs under passive inflow conditions become narrower and symmetric, when compared to the near wake. Under active inflow conditions, the distributions of u' are broader when compared to the passive inflow and independent of the turbine. In comparison to the top tip, no influence of shed vortices is observed at bottom tip.

In the far wake, differences introduced by the turbines, which are clearly seen in the near wake diminish, and the shape of the pdfs depends predominantly on the inflow conditions. The pdfs become more symmetric indicating the recovery of the flow. The shapes of the pdfs are similar at the measurement positions, indicating softened gradients in the vertical direction and a homogeneous distribution of fluctuations over the rotor area. Local maxima observed in the near wake are vanished.

Overall higher fatigue loads - also for a downstream turbine - under more turbulent inflow conditions are expected. Turbines positioned in the wake of other turbines experience highly turbulent inflow, even under low turbulence inflow conditions for the first turbine as it is shown in the passive case. In the case of floating turbines, again a different distribution of fluctuating loads can be expected, but this effect is less pronounced than the shift in the mean inflow.

Spectral analysis

More detailed investigations of the impact of the inflow conditions and turbine type on the fluctuations are performed in the frequency domain by means of power spectral densities (psd). Figure 41 shows averaged power spectral densities for measurement positions above top tip, at top tip, hub height and at bottom tip under passive and active inflow conditions for the fixed and floating turbine measured at the inflow, near and far wake. As in Section 4.2, frequencies are represented as corresponding

scales.

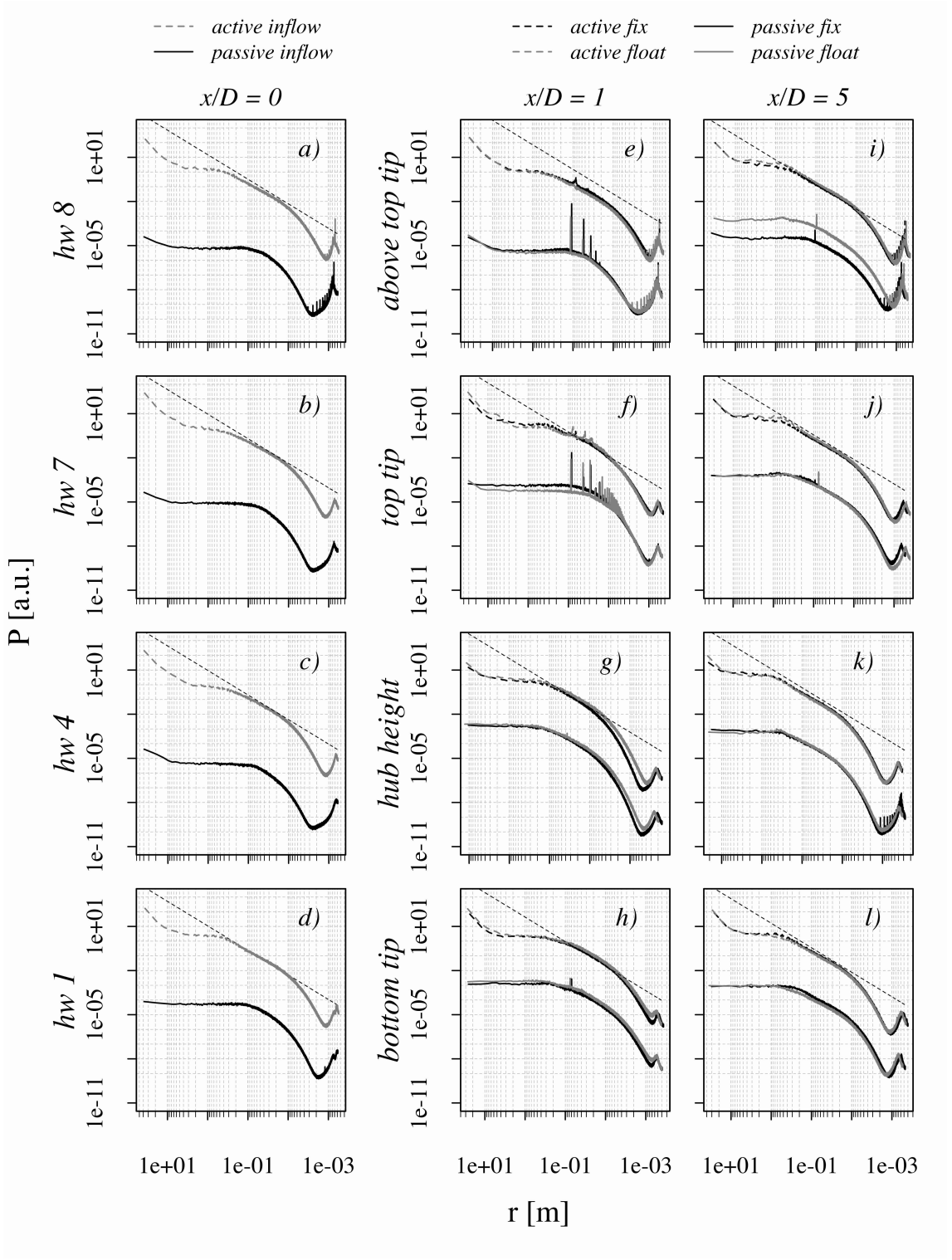

Abbildung 41: Power spectral densities for passive and active inflow conditions measured above top tip, at top tip, hub height and at bottom tip at downstream positions $x/D = 0$ D, $x/D = 1$ D, $x/D = 5$ D. Spectra for active inflow conditions are shifted up for clarity. The dashed lines follow $r^{5/3}$-scaling (corresponding to $f^{-5/3}$) which is found for homogeneous isotropic turbulence.

As was discussed in Section 4.2, the psds at $x/D = 0$ with no turbines installed in the flow are independent of the measurement position, but reveal significantly differing dynamics between passive and active inflow.
First, the inflow is discussed, where in the passive case, structures larger than 0.07 m are approaching the turbines with same intensity. With decreasing size from 0.07 m to 0.003 m a rapid decay is observed. The power for scales $<$ 0.003 m, i.e., frequencies $>$ 2 kHz, is attributed to noise and limitations of the low-pass filter in the CTA module. In the active case, large structures $>$ 3 m dominate the inflow dynamics and a plateau is found between $\sim$ 3 m and $\sim$ 1.3-1.6 m, where structures contribute equally to the power of the flow, when compared to the passive inflow. The power decay of smaller structures down to 0.006 m - attributed to higher frequencies - has a pronounced linear range following Kolmogorovs hypothesis [18].

Under passive inflow conditions, at the top of the near wake at $x/D = 1$ (cf. Figures 41 e, f) the general shapes of the spectra do not change when compared to the inflow, but peaks are found, with the first being at $\sim$ 0.09 m, i.e., 56 Hz corresponding to the rotational frequency f_{rot} of the rotor. The remaining peaks are harmonics of f_{rot}. In the passive floating case the power at the peaks is dampened and more harmonics are found due to the oscillation of the floating turbine and the reduced interaction between flow and turbine at that height.
Under active inflow conditions, energy is shifted from large scales to smaller scales and the dynamics of the flow are dominated by a behavior following a scaling law, thus turbulence production. The integral length is decreased to 0.01 m for the fixed case, indicating that the turbine destroys large structures, that are present in the inflow. The impact of shed vortices due to the rotational frequency is reduced by orders of magnitude, which are instable due to the turbulence generation, when compared to the passive case. This is further decreased for the floating turbine, where the rotational frequency is barely found in the spectrum, which is - in addition to the highly fluctuating inflow condition - due to the reduced interaction of the flow with the turbine caused by the oscillation.

At hub height and below in the passive case, energy is shifted to structures >0.5 m, i.e., in the size of the rotor and larger, when compared to the inflow. A short linear range develops, i.e., a turbulent energy cascade is created by the turbine. At bottom tip shed vortices from blade tips are less stable due to the interaction with the tower. These did not reveal in the fluctuations. In the active case, the inertial range with linear relation between power and scales is shortened and the shape of the spectrum is similar to what is found in the passive case for scales $<$ 5 m. The range of linear relation of power and scales is smaller for both turbines, indicating

earlier dominance of dissipation, when compared to the inflow.

The differences in dynamics between the two inflow conditions persist in the near wake. Under passive inflow conditions, the rotation of the rotor has a significant impact on the dynamics of the upper part of the wake. The total power in the signal is higher due to the presence of the turbine, thus the added turbulence and enhanced mixing, when compared to the inflow. The turbines tower disturbs shed vortices from the rotor tip, which is seen at bottom tip. Under highly turbulent inflow conditions, effects due to the rotation of the rotor are masked by the large structures and the inflow dynamics, where the turbulence dominates the flow and causes instabilities of shed vortices from the rotor. At hub height and bottom tip, spectra between passive and active inflow have similar shapes, indicating the dominance of aerodynamic effects introduced by bluff bodies, such as hub and tower.

In the far wake at $x/D = 5$ at top tip and above in the passive fixed case, one order of magnitude more power is contained in scales down to 0.2 m. The contribution of shed tip vortices is less outstanding at top tip due to more mixed flow conditions in the far wake and the expansion of the wake. An energy cascade is found for scales of 0.2 m to 0.02 m. In Figure 41 i) the signal for the floating turbine has a similar shape when compared to the fixed turbine, but contains two orders of magnitude more power in scales down to 0.2 m, indicating much stronger dynamics in the signal introduced by the presence of the turbine and its oscillation, which is in agreement to findings in the pdfs.

In the active case, the spectra at all measurement positions resemble similar shapes as for the inflow and collapse for the fixed and floating turbines. The spectra contain more power for scales between 10 m and 0.2 m, as well as an extended inertial range, when compared to the spectra of the inlow and also when compared to the spectra of the near wake. At hub height in the passive case, the plateaus down to 0.6 m persist in the spectra of both turbines, when compared to the near wake. A decay following a power law is found between 0.6 m and 0.02 m.

In the far wake, the total power is higher for both inflow conditions, which is due to the larger distance to the turbine, thus more mixed flow. An overall shift in the power to scales of the size of the blade chord length, rotor diameter and even bigger is observed, thus the turbine adds to and modifies significantly the scales of the dynamics in the wake flow. Under active inflow conditions the spectra in the far wake contain more power for scales from 6 m down to 0.6 m, but have rather similar shapes as for the inflow, which is due to the strong turbulent mixing introduced by the active grid in the inflow. The application of spectral analysis reveals that due to the presence of the turbine an enhanced inertial range is found, thus a broader range

of scales approaching a wind turbine positioned downstream. The broader range of approaching scales could result in a more complex load situations, by producing mechanical vibrations on a wider range of frequencies as well as creating higher band of acoustical noise, which have to be considered and accounted for in the design of the turbine parts, especially the blades and the nacelle, where the blades are mounted. In terms of the scales, no significant changes are introduced by a floating platform, but the general turbulent characteristics of the flow are of importance.

Spatial analysis

After the spectral analysis we turn to the spatial aspects of the flow by means of cross correlations ρ, which determine linear dependence between the measurements taken with the hot-wires. Therefore two time series $u(t)$, $v(t)$ are shifted by a time lag τ and ρ is computed by,

$$\rho_{u,v}(\tau) = \frac{1}{\sigma_u \sigma_v} \frac{1}{N} \sum_{n=1}^{N-1} u(n) v(n-\tau) \quad , \tag{35}$$

with σ_u, σ_v being the standard deviations of the time series of length N. Calculating ρ between points in the measurement plane provides insight on the presence of coherent structures in the flow [30].

Figure 42 a) shows contour plots of pair-wise cross-correlations for $\tau = 0$ between the hot-wires $i, j = 1..16$ for the passive and active inflow at $x/D = 0$. The x- and y-axes represent the corresponding hot-wire numbers as located in the hot-wire rake diagram and $\rho_{i,j}$ is color coded. The upper left triangle shows the correlations of the passive inflow conditions and the lower right triangle for the active.

Correlations found in the near wake at $x/D = 1$ and far wake at $x/D = 5$ of the fixed and floating wind turbine are shown in Figure 42 b) for passive and active inflow conditions. The upper left triangle shows ρ_{ij} for the fixed turbine and the lower right triangle for the floating turbine. On the diagonal the correlation is 1, since it is the auto-correlation of each hot-wire measurement. A sketch of the hot-wire arrangement is added to facilitate interpretation.

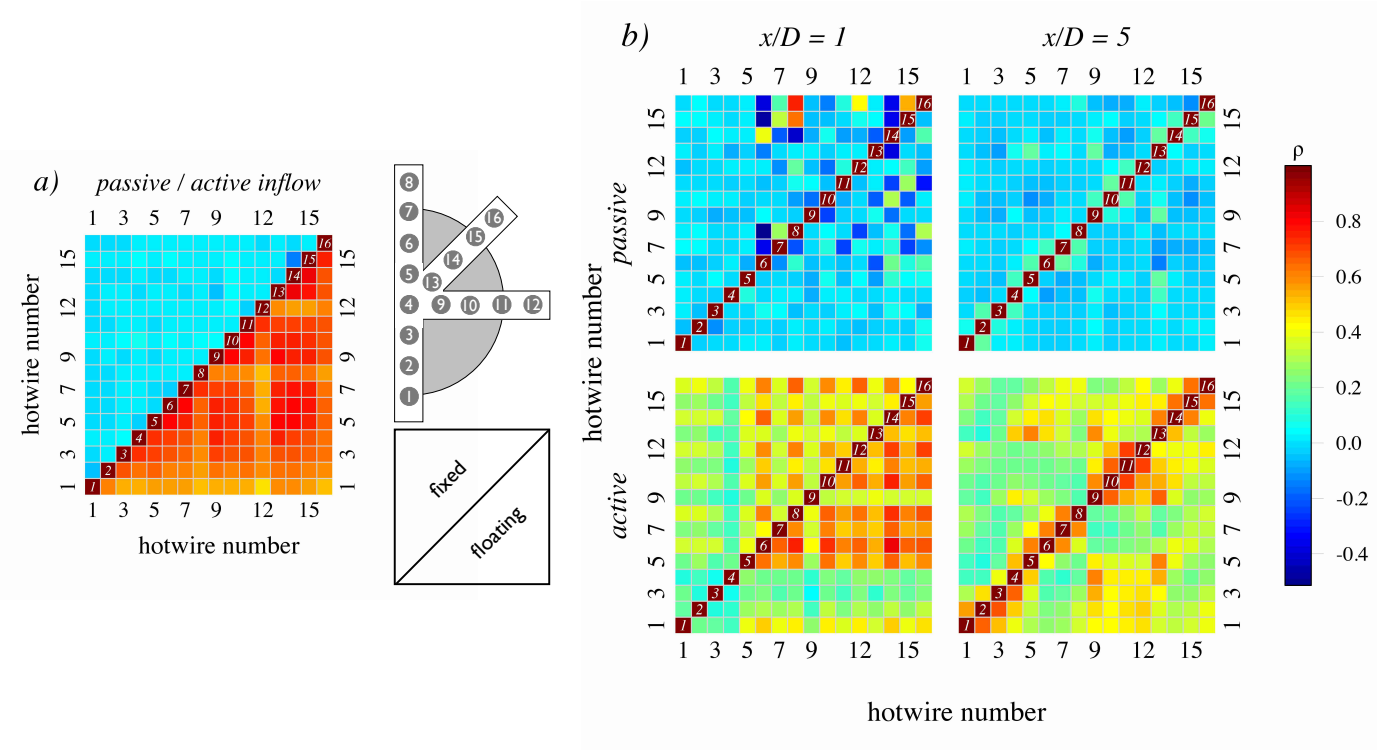

Abbildung 42: Cross-correlation coefficients $\rho_{i,j}(\tau)$ between measurement positions at hot-wires i, j under passive and active inflow conditions for the fixed and floating turbine at (a) $x/D = 0$ D, (b) $x/D = 1$ D, $x/D = 5$ D. A sketch of the hot-wire arrangement is added, to facilitate the interpretation. The colorbar for ρ on the right applies for all contours in the figure.

At $x/D = 0$ under passive inflow conditions, no clear correlations are observed. This is due the small structures introduced by the passive grid, which are well mixed at $x/D = 0$ as was shown in section 4.3. Under active inflow conditions, significant positive correlations are introduced by the active grid where large scales are introduced when compared to the passive grid (cf. Ref [14]). Note, no significant differences between sensors is observed - all correlations are quite homogeneous. Results are in agreement with the power density spectra, where large structures contain most of the energy.

Next we discuss the wake behavior, where we see again the overall tendency that the active flow is more correlated, i.e. the wind turbine is not destroying the large scales completely, which is in accordance with what was found for the spectra. At $x/D = 1$, under passive inflow conditions for the fixed case, clear correlations are found between hot-wires 16 and 12 as well as 16 and 8, which could be explained by vortex shedding at the blade tips and the expansion of the wake. Once again, this is in accordance with peaks observed in the power density spectra. Signals of hot-wire 12 and 8 are weakly correlated, which is due to the larger distance between

the two measurement points, since the turbine rotates counter-clockwise, thus the wake clockwise. Furthermore, $\rho_{16,15}$ and $\rho_{8,7}$ are positive, while $\rho_{16,14}$ and $\rho_{8,6}$ are negative. This is due to the helical structure created by the rotor at the blade roots being transported downstream slower, than the structures created at the blade tips. This creates a phase shift between the helix created at, e.g., hot-wire 16 and hot-wire 14, which is shown in Figure 43 a), where the correlations are plotted over τ. From this, an analogue development is expected for $\rho_{12,11}$ and $\rho_{12,10}$, which has the phase shift, but overall reduced correlations. In the near wake of the floating turbine (cf. Fig 43 b)), the coherent structures created at the blade tips are destroyed by the oscillation of the turbine.

In general, high absolute values of correlations are found in the top tip region and the diagonal outer tip region of the wake in the fixed case under passive inflow conditions. The oscillation of the turbine weakens the correlation caused by shed vortices, i.e., the harmonics found in the spectra in Figure 41 e), f) are uncorrelated on average.

Still observing the near wake and under active inflow conditions, the correlations contained in the inflow are reduced, especially for the fixed turbine, i.e., the turbine cuts down large correlated structures of the flow and - as was shown in the spectra - the rotation of the rotor does not create dominating structures, that persist in the near wake as it was found under passive inflow (cf. Fig. 44 a). The floating turbine introduces correlations in the upper quadrant of the rotor (cf. Fig 42 b), where the structures created by the rotor rotation remain longer in the flow, which is in agreement to observations in the power density spectra. In addition, correlations are introduced by the oscillation of the turbine, which acts as a “hand fan”. Below hub height, the tower disrupts coherent structures, so ρ is close to 0. Figure 44 a) shows the correlation functions between hot-wire 16 and 15, 14 as well as 13 under active inflow conditions for the fixed and floating turbine at $x/D = 1$. Correlations caused by the grid decay very slowly and become 0 for $\tau > 10$ s, i.e., the present structures are large in a spatial and temporal sense, while turbine type and rotation of the rotor has a negligible influence.

In the far wake at $x/D = 5$, correlations are not apparent under passive inflow conditions for both turbines, i.e., the flow is well mixed with no remaining dominant structures on average. Under active inflow conditions, the neighboring hot-wires are correlated in the far wake for both turbines, i.e., structures in size of ~ 0.033 m, corresponding to the spacing between the hot-wires would approach a turbine positioned downstream.

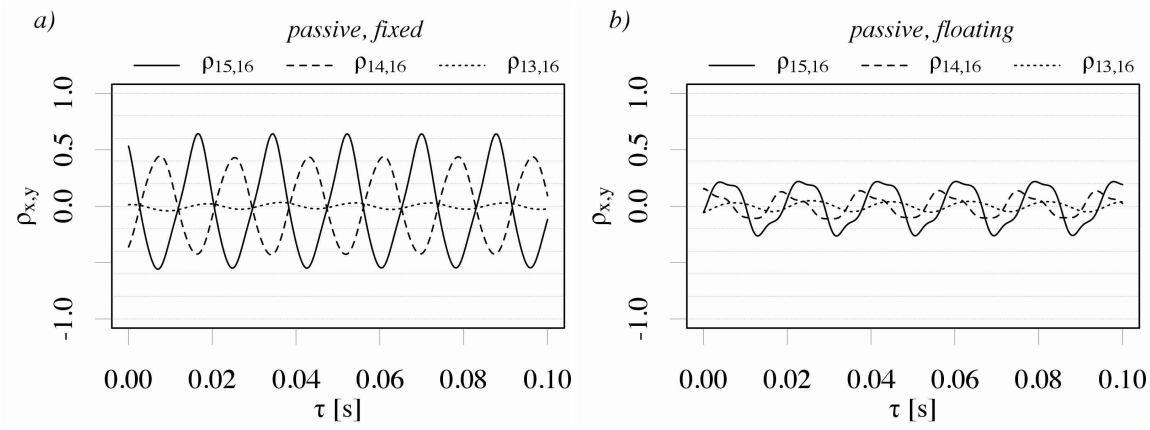

Abbildung 43: Correlation function $\rho_{15,16}(\tau)$, $\rho_{14,16}(\tau)$ and $\rho_{13,16}(\tau)$ under passive inflow conditions for fixed and floating turbine $x/D = 1$ D.

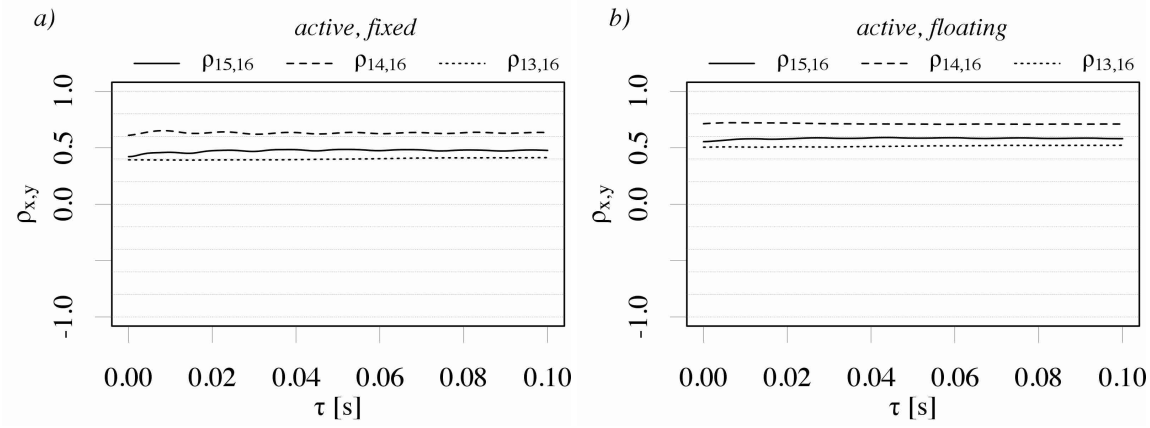

Abbildung 44: Correlation function $\rho_{15,16}(\tau)$, $\rho_{14,16}(\tau)$ and $\rho_{13,16}(\tau)$ under active inflow conditions for fixed and floating turbine $x/D = 1$ D.

For a turbine positioned in the wake of a turbine subjected to active and passive inflow conditions, large differences arise in terms of structures approaching the turbine, thus acting forces on the turbine. Under passive inflow, coherent structures introduced in the near wake by the fixed turbine are vanished in the far wake, resulting in more homogeneously mixed inflow. Under active inflow conditions, larger coherent structures approach the turbine when compared to the passive inflow, which have a higher variability at scales of 0.5 m to 6 m, as it was shown in the spectra. This will cause larger velocity gradients over the rotor area, thus stronger moments acting on the downstream turbine.

For a turbine positioned in the far wake of the turbine, again, the turbulence of the inflow plays a major role. An oscillating platform smears correlated pattern in the wake considerably under low turbulence, whereas under high turbulent inflow, the

impact of the turbine is covered under the surrounding turbulence already present in the inflow.

4.4 Proper orthogonal decomposition

The POD allows for an understanding of contained turbulent kinetic energy in reoccurring patterns in the flow and reveals differences in the structural composition of the passive and active inflow conditions as well as in resulting wake developments for both turbine types. Following Section 4.1, the POD is applied on the data measured with the hot-wire rake for both inflow conditions with the fixed and floating wind turbine.

Kinetic energy per mode

First the varying development of the turbulent kinetic energy between the measurement cases is discussed. Figure 45 shows the normalized eigenvalues λ_i with $i = 1..16$ representing contained turbulent kinetic energy per mode 1 to 16 for the inflow at $x/D = 0$ as well as in the wake of the turbines at $x/D = 1$ and $x/D = 5$. In Figure 46, the cumulative energy contained in the modes is presented, which is the summation of energy in the subset of modes.

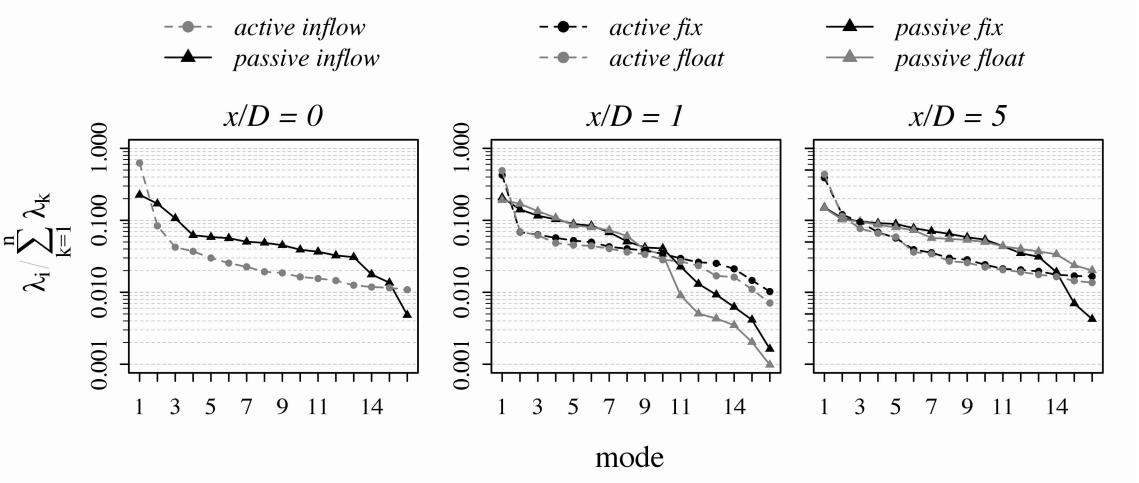

Abbildung 45: Normalized Eigenvalues for passive and active protocol at $x/D = 0$ D, $x/D = 1$ D, $x/D = 5$ D

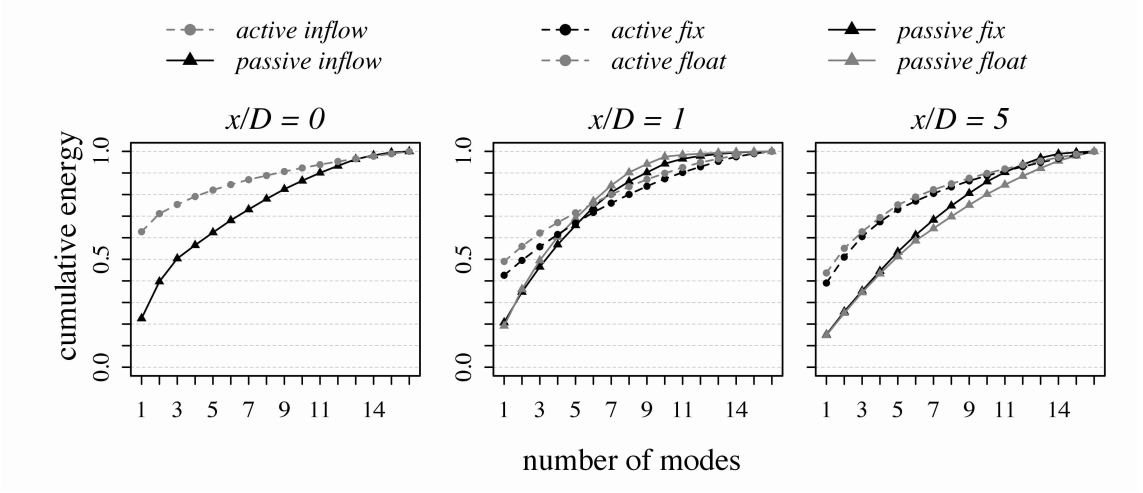

Abbildung 46: Cumulative energy of Eigenvalues for passive and active protocol at $x/D = 0$ D, $x/D = 1$ D, $x/D = 5$ D

The active inflow is dominated by the first mode, which contains 62% of the total energy. Modes 2 to 4 show a rapid decrease in terms of contained energy, but cover $\sim$ 18% of the total energy in the inflow. This is in agreement with findings in the correlations (cf. Sec. 4.3), where the active inflow is dominated by large reoccurring structures and the small, less energetic structures are covered by higher modes. The curves for the active inflow, found in Fig. 45 and 46 indicate similarities to atmospheric inflow conditions by resembling similar shapes as was found by Saranyasoontorn *et al.* for simulated wind fields under the assumptions of a Kaimal spectral model and the IEC exponential coherence model (cf. [26]). Also under passive inflow the first modes are found to be dominant, but 5 modes are needed to cover as much of the kinetic energy as the first mode in the active case. The decay of energy per mode is much slower, with no significantly dominant structures driving the flow.

In the near wake under active inflow conditions, the first 3 modes cover as much energy as the first mode in the inflow, then a decay of energy per mode is observed, similar to what was found for the passive inflow condition at $x/D = 0$. Under passive inflow conditions, the energy per mode for modes 1 to 10 follows an exponential decay (a linear trend in a semi-log plot, cf. Fig. 45), where at mode 10, it is converged to almost 100% of the total kinetic energy. The type of the turbine has a minor impact on the distribution of energy per mode. The POD as a representation of the whole flow field reveals only a minor impact of the turbine type on the contained turbulent kinetic energy.

In the far wake under passive inflow, the energy described by the first mode is further decreased and a slow decay in energy per mode is observed, resulting in the

need of 12 modes to describe 90% of the cumulative energy, which is due to the flow containing less correlated structures. Under active inflow in the far wake, the first modes gain importance in describing kinetic energy contained in the flow, when compared to the near wake. The shift to scales of the size of the turbine geometry observed in the spectra and correlations, results in a shift of contained kinetic energy from the first mode to higher modes, increasing the complexity in the flow structures. Again the turbine type has a negligible impact, as was observed in the statistical quantities discussed in Section 4.3.

Eigenmodes

The POD-Eigenmodes represent reoccurring patterns in the flow, which are then weighted with the eigenvalue, i.e. contained kinetic energy, to represent flow characteristics. Figure 47 shows the first four eigenmodes ϕ_1 to ϕ_4 at distinct vertical measurement positions (cf. Section 4.1). The modes are normalized to have a length of 1. The signs of the modes are arbitrary and are not physically interpreted. The radial positions are not shown for visual clarity.

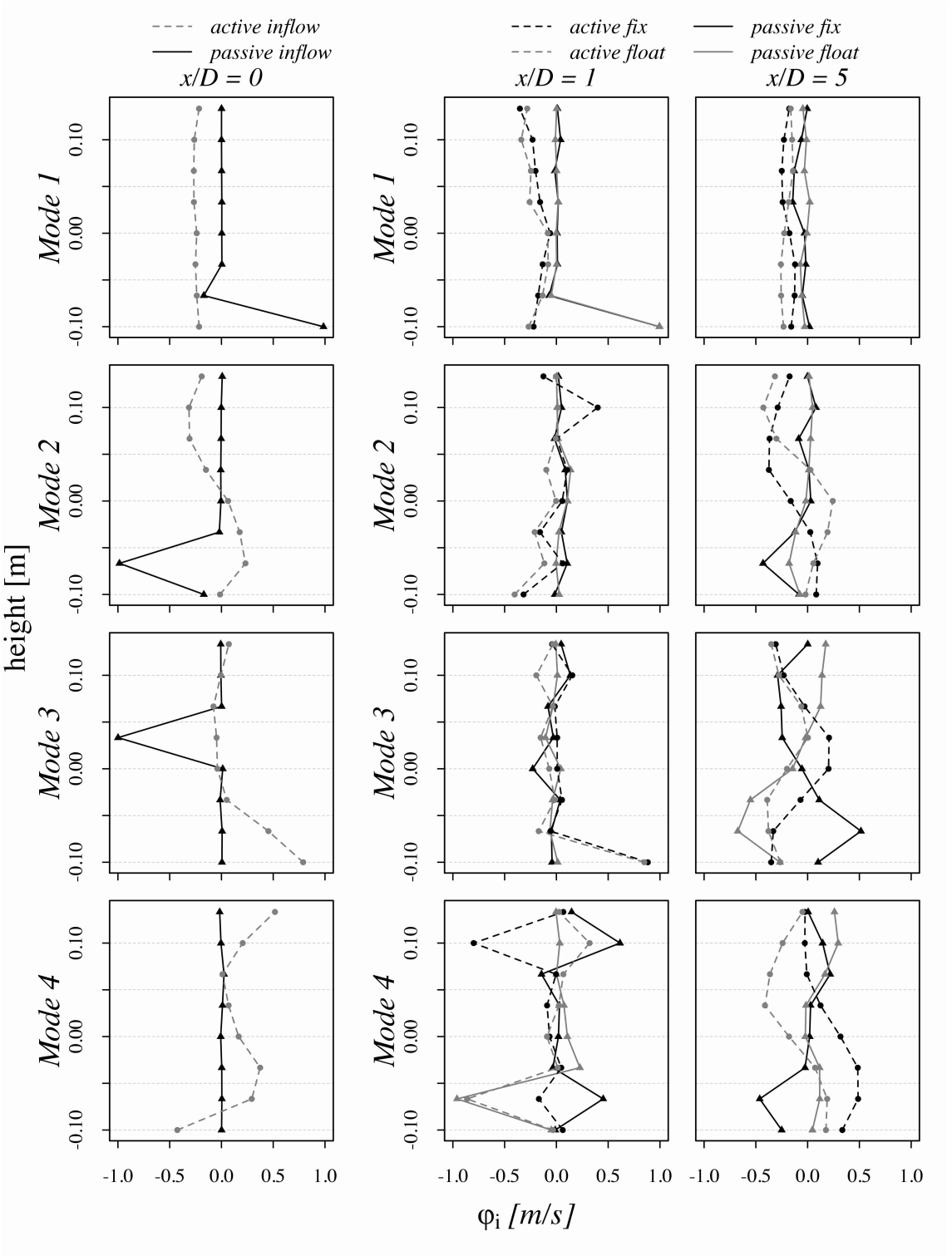

Abbildung 47: Eigenmodes $\phi = 1$ to 4 at $x/D = 0$ D, $x/D = 1$ D, $x/D = 5$ D

For the passive inflow, a clear dominance at one measurement point per mode is seen, while at other positions the values are zero, i.e., the passive inflow consists of

small pattern locally contributing to flow structure, which follows the development of the cumulative energy in Figure 46. Under the active inflow, the first mode contributes evenly, but with a slight convex shape, to all measurement positions, which corresponds well to the large structures created by the active grid and is also covered by the high turbulence kinetic energy contained in the first mode. The second and fourth modes have an "Sshape, causing an asymmetric inflow profile above and below hub height, while mode 3 represents structures found below hub height. The combination of the modes results in a complex, highly energetic (cf. 4.4) flow pattern aproaching the wind turbine, resulting in a complex load situation for the wind turbine, which also varies locally due to the dynamic inclination of the turbine.

In the near wake at $x/D = 1$, presence and type of the turbine have negligible influence on mode 1 under passive inflow conditions. Modes 2 and 3 are close to 0 at all points and have spikes at radial positions, which are not shown here. A significant difference between the fixed and floating turbine is observed at mode 4, where in the fixed case mode 4 describes dynamics at top tip and close to bottom tip, while in the floating case only the dynamics close to the bottom tip are captured.

Under active inflow condition in the near wake, mode 1 has a concave shape and is 0 at hub height for the fixed and floating turbine, where highest deficit is found in the mean velocities. Mode 2 captures increased dynamics at top tip for the fixed turbine, when compared to the floating case, which also was observed in increased influence of the rotational frequency in the spectra (cf. 4.3). Mode 4 for the fixed turbine is horizontally mirrored to that for the floating turbine, i.e., the oscillation of the turbine shifts the importance of structures from top to bottom tip, which is also true for passive inflow.

In the far wake at $x/D = 5$ under passive inflow conditions, the mode pattern become more complex, when compared to the inflow and near wake. Mode 2 is zero at hub height and above, i.e. structures below hub height and at radial positions impact the dynamics in the far wake. Mode 3 is horizontally mirrored for the far wake of fixed turbine, when compared to the floating, which could be due to the arbitrary choice of the mode sign.

Under active inflow conditions, mode 1 contributes to all measurement positions having an SSshape for the fixed and floating turbine. Mode 2 to 4 are SSshaped and contribute at all positions to the flow structure, indicating opposing energetic contributions above hub height and below. Mode 2 for the floating turbine is shifted upwards, which was also found for mean and fluctuating quantities in PIV-data by Rockel *et el.* [21]. This is due to the floating turbine causing a deflection of structures in the order of the rotor size, which dominate the flow dynamics under active inflow

conditions. This shift is not observed under passive inflow conditions, which is due to the importance of all modes in terms of kinetic energy.

In general, modes under active inflow conditions have smother shapes at $x/D = 0$ and 5 when compared to passive inflow, which is due to the large correlated structures being present in the inflow, but also being maintained and transported into the far wake. Under passive inflow, every mode contributes predominantly at one point to the flow dynamics, with every mode being energetically important, which is due to the low correlation between the measurement positions, i.e. the absence of large correlated structures.

Reconstruction

The POD allows for reconstruction of the investigated time series using a set of POD-modes, to find a low-dimensional representation of the flow, but containing a significant amount of turbulent kinetic energy. This allows for a simplified representation of complex flow conditions, by choosing a reduced set of eigenmodes. The reconstruction is performed, to give insight on the number of modes required to achieve a low order representation of the flow, depending on turbine type and inflow conditions.

The first row in figure 48 shows 5 s of the original time-series measured at hot-wire 7 (top tip) under passive and active inflow conditions at $x/D = 0$ without the turbine installed and in the wake of the fixed and floating turbine at $x/D = 1$ and $x/D = 5$. Below the reconstructed time-series are shown, where the first mode, modes 1 to 2, 1 to 3 and 1 to 4 were used. As discussed earlier, higher turbulence is observed under active inflow condition throughout the measurement positions.

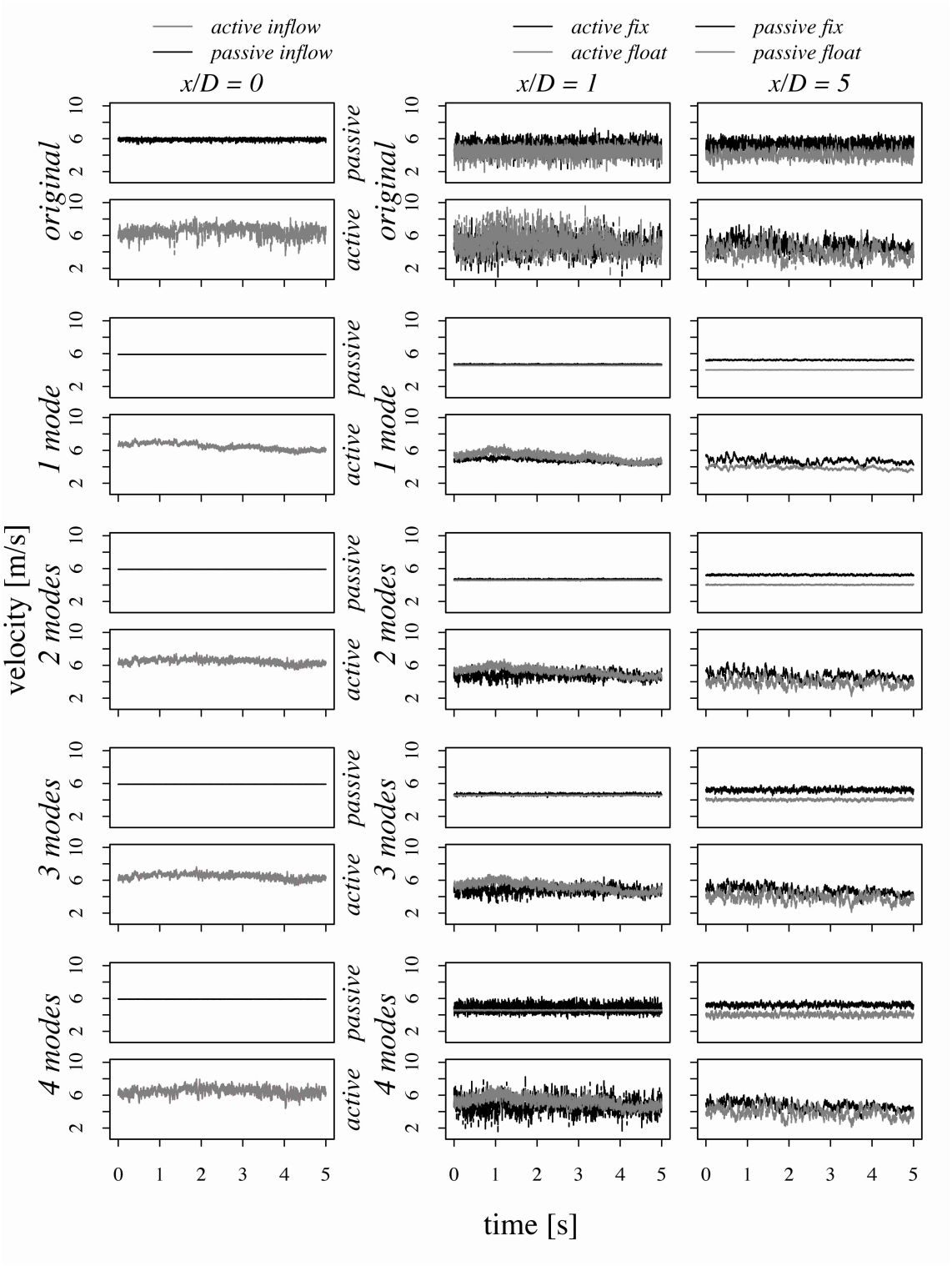

Abbildung 48: Original time series at hot-wire 7 (top tip) and reconstructed time series using 1 to 4 modes at $x/D = 0$ D, $x/D = 1$ D, $x/D = 5$ D. The black lines represent the flow for the fixed and the grey lines for the floating wind turbine.

As expected from the eigenmodes (cf. Fig. 47) no dynamics are reconstructed for the passive inflow at $x/D = 0$ using the first 4 modes, since the first four eigenmodes are zero at top tip. Under active inflow conditions, already the first mode allows a reconstruction of main characteristics of the inflow, which is steadily improved by adding modes 2 to 4, where the flow contains 50% of the turbulent kinetic energy when compared to the original time series.

In the near wake at $x/D = 1$, under passive inflow the original time series shows similar ranges of fluctuations for the fixed and floating wind turbine. Under active inflow conditions, stronger fluctuations are observed, which are also present on large scales, again for both turbines. Using the first 3 modes no dynamics are reconstructed under passive inflow. Mode 4 allows to reconstruct 57% of the turbulent kinetic energy of the original time series for the fixed turbine and 0% for the floating wind turbine. Under active inflow conditions, mode 1 reconstructs dynamics on larger scales, but not the strong short term fluctuations. For the fixed turbine 9% of the turbulent kinetic energy are reconstructed, while for the floating turbine 27% are covered. Mode 2 and 3 do not add significant improvement for the floating wind turbine, but for the fixed turbine 24% of turbulent kinetic energy are reconstructed. Mode 4 allows to reconstruct 88% of the turbulent kinetic energy for the fixed turbine, while for the floating turbine less information is added with 38% of turbulent kinetic energy when compared to the original time series. The flow at top tip for the fixed turbine is dominated by shed vortices, which are less correlated for the floating turbine, due to its oscillation.

In the far wake at $x/D = 5$, under passive inflow conditions only minor differences are present in the range of fluctuations for the fixed and floating wind turbine. As in the near wake, the reconstruction using modes 1 to 4 covers less than 50% of the turbulent kinetic energy. Under active inflow conditions, the range of fluctuations of the original time series is broader when compared to the passive inflow and changes on large scales are observed. In contrast to the passive inflow, mode 1 to 3 allow to reconstruct large scale dynamics and 48% of the turbulent kinetic energy for the fixed turbine and 39% for the floating turbine. Mode 4 does not add dynamics for the fixed turbine, but allows to reconstruct 55% of turbulent kinetic energy for the floating wind turbine.

4.5 Conclusion

Turbulent wake characteristics of a floating wind turbine model in comparison to the wake of a classic bottom fixed turbine model under low and high turbulence inflow conditions have been investigated. In order to achieve this wind tunnel experiments

were performed, where the differing inflow conditions were created using an active grid and the wakes of the turbines were measured with a rake of 16 hot-wires.

When compared to the passive inflow, the wider range of fluctuations under active inflow conditions causes strong variations in the performance of the turbines, which is seen in the broader range of rotational frequencies as well as varying power coefficients. This results in an increased effort in controlling the turbine to optimal operational conditions and is further complicated by the oscillation of the turbine.

The oscillation of the turbine causes an upwards shift of the wake, which is dampened under highly turbulent inflow. Turbulence intensity level in the wake remains higher for highly turbulent inflow, even at hub height, where in the near wake the turbulence intensity increases to comparable levels for both inflow conditions.

Under low turbulence inflow conditions, shed tip vortices formed at the blade remain stable in the wake and define the wake characteristics. These structures are destabilized but still present for the floating wind turbine. In addition, the floating turbine inhibits the formation of correlated structures at the blade root and at the blade tips, which are clearly present in the wake of the fixed turbine. There, structures created due to the rotation of the rotor are transported downstream with the reduced mean velocities in the wake, as it was seen in the spatial analysis.

Under high turbulence inflow, the wake structure is defined by the inflow condition and is only weakly dependent on the turbine type. Large correlated structures found in the inflow are cut down by the turbines and the structure size is shifted to the size of the rotor, as it was seen in the spectral analysis.

Characteristics found in the far wake are results of the conditions created in the near wake by the presence of varying inflow conditions and operation of different turbine types. The observed influence of the turbine type on the flow in the near wake, such as the increased fluctuations as it is seen in the broader pdfs for the floating turbine under active and passive condition (cf. Figure 40), the shed tip vortices as observed in the spectra at top tip (cf. Figure 41), show to have subordinated influence on the turbulent characteristics in scales and fluctuations compared to the general turbulent characteristics of the inflow conditions.

The POD reveals, that the modes found under active inflow conditions have a higher complexity, but due to the high amount of contained kinetic energy only the first few modes are needed to reconstruct a representation of the flow situation, covering high percentage of the original turbulent kinetic energy, thus characteristic fluctuations. Under passive inflow, the modes only contribute point-wise to the wake structure, thus many modes are needed to reconstruct an energetically representative composition of the flow. For both inflow conditions, the oscillation of the turbine has

a subordinated influence on the reconstruction of the flow. A systematic investigation on how the reconstruction of the time series performs depending on the choice of the POD basis could be addressed in future work.

Platform pitch results in an upwards shift of the mean and fluctuating inflow of a downstream turbine, resulting in an increase in the varying load situations over the rotor area. These loads will also oscillate up and down over time, due to the non constant inclination of the turbine, which is a result of the inflow characteristics. The situation is further complicated by the potential motion of the downstream turbine, which is mounted on a floating platform, thats motion is not synchronized with the motion of the first turbine. This potentially leads to the need of more robust design in terms of load variability for floating wind turbines in wind farm configurations.

Further investigation on how other isolated degrees of freedom and their combination, as well as different floating turbine designs effect wake structures and inflow conditions of the downwind turbine can be considered in future work.

Literaturverzeichnis

[1] D. Bastine, L. Vollmer, M. Wächter, and J. Peinke. Stochastic Wake Modeling Based on POD Analysis. *Wind Energ. Sci. Discuss.*, 2016.

[2] D. Bastine, B. Witha, M. Wächter, and J. Peinke. Towards a Simplified DynamicWake Model Using POD Analysis. *Energies*, 8(2):895–920, 2015.

[3] G. K. Batchelor. Introduction To Fluid Dynamics. 2000.

[4] G. Berkooz, P. Holmes, and J. L. Lumley. The proper orthogonal decomposition in the analysis of turbulent flows. *Annual Review of Fluid Mechanics*, (1971), 1993.

[5] J. Citriniti. Experimental investigation into the dynamics of the axisymmetric mixing layer utilizing the proper orthogonal decomposition. *Vasa*, 1996.

[6] M. N. Glauser, S. J. Leib, and W. K. George. Coherent Structures in the Axisymmetric Jet Mixing Layer. *Turbulent Shear Flows 5*, 1987.

[7] N. Hamilton, M. Tutkun, and R. B. Cal. Wind turbine boundary layer arrays for Cartesian and staggered configurations: Part II , low-dimensional representations via the proper orthogonal decomposition. *Wind Energy*, 18(2):297–315, feb 2015.

[8] S. Ivanell, R. Mikkelsen, J. N. Sørensen, and D. Henningson. Stability analysis of the tip vortices of a wind turbine. *Wind Energy*, 13(8):705–715, nov 2010.

[9] P. B. V. Johansson, W. K. George, and S. H. Woodward. Proper orthogonal decomposition of an axisymmetric turbulent wake behind a disk. *Physics of Fluids*, 14(7):2508, 2002.

[10] J. M. Jonkman. Dynamics of offshore floating wind turbines—model development and verification. *Wind Energy*, (June):459–492, 2009.

[11] J. M. Jonkman and D. Matha. A quantitative comparison of the responses of three floating platforms. *National Renewable Energy Laboratory*, 2010.

[12] J. M. Jonkman and D. Matha. Dynamics of offshore floating wind turbines—analysis of three concepts. *Wind Energy*, (January):557–569, 2011.

[13] M. Khosravi, P. Sarkar, and H. Hu. An Experimental Investigation on the Performance and the Wake Characteristics of a Wind Turbine Subjected to Surge Motion. *33rd Wind Energy Symposium*, (June):1–18, 2015.

[14] P. Knebel. Aktives Gitter zur Simulation atmosphärischer Windfelder im Windkanal. PhD thesis, 2011.

[15] D. Matha, M. Schlipf, A. Cordle, R. Pereira, and J. Jonkman. Challenges in Simulation of Aerodynamics, Hydrodynamics, and Mooring-Line Dynamics of Floating Offshore Wind Turbines. *National Renewable Energy Laboratory*, 2011.

[16] A. Morales, M. Wächter, and J. Peinke. Characterization of wind turbulence by higher-order statistics. *Wind Energy*, 15(3):391–406, apr 2012.

[17] P. L. O'Neill, D. Nicolaides, D. Honnery, and J. Soria. Autocorrelation Functions and the Determination of Integral Length with Reference to Experimental and Numerical Data. *15th Australasian Fluid Mechanics Conference*, 1(December):1–4, 2004.

[18] S. B. Pope. *Turbulent Flows*. Cambridge University Press, 2000.

[19] W. H. Press. Numerical recipes: the art of scientific computing. *Cambridge, UK*, 2007.

[20] S. C. Pryor and R. J. Barthelmie. Statistical analysis of flow characteristics in the coastal zone. *Journal of Wind Engineering and Industrial Aerodynamics*, 90(3):201–221, 2002.

[21] S. Rockel, E. Camp, J. Schmidt, J. Peinke, R. B. Cal, and M. Hölling. Experimental Study on Influence of Pitch Motion on the Wake of a Floating Wind Turbine Model. *Energies*, 7(4):1954–1985, mar 2014.

[22] S. Rockel, J. Peinke, M. Hölling, and R. B. Cal. Wake to wake interaction of floating wind turbine models in free pitch motion: An eddy viscosity and mixing length approach. *Renewable Energy*, 85:666–676, jan 2016.

[23] B. Sanderse. Aerodynamics of wind turbine wakes -literature review. *Technical Report No. ECN-E-09-016*, 2009.

[24] B. Sanderse. Review of computational fluid dynamics for wind turbine wake aerodynamics. (February):799–819, 2011.

[25] T. Sant, D. Bonnici, R. Farrugia, and D. Micallef. Measurements and modelling of the power performance of a model floating wind turbine under controlled conditions. *Wind Energy*, 18(5):811–834, may 2015.

[26] K. Saranyasoontorn and L. Manuel. Low-Dimensional Representations of Inflow Turbulence and Wind Turbine Response Using Proper Orthogonal Decomposition. *Journal of Solar Energy Engineering*, 127(4):553, 2005.

[27] T. Sebastian and M. A. Lackner. Characterization of the unsteady aerodynamics of offshore floating wind turbines. *Wind Energy*, (March 2012):339–352, 2012.

[28] D. A. Simms, S. Schreck, M. Hand, and L. J. Fingersh. NREL unsteady aerodynamics experiment in the NASA-Ames wind tunnel: A comparison of predictions to measurements. *National Renewable Energy Laboratory*, 2001.

[29] G. I. Taylor. The spectrum of turbulence. *Proceedings of the Royal Society A: Mathematical, Physical and Engineering Sciences*, 164(919):476–490, 1938.

[30] D. J. Tritton. Physical Fluid Dynamics. 1988.

[31] S. Weitemeyer, N. Reinke, J. Peinke, and M. Hölling. Multi-scale generation of turbulence with fractal grids and an active grid. *Fluid Dynamics Research*, 45(6):061407, dec 2013.

5 Summary and Conclusions

Comprehensive wind tunnel experiments were performed to provide a detailed understanding of wake dynamics introduced by floating offshore wind turbines with additional degrees of freedom. Therefore, model scale wind turbines were set up and flow measurements were performed in two different wind tunnels under various inflow conditions. Wakes of the turbines were measured, analyzed and characterized using a broad set of methods. To isolate and identify wake effects induced by platform motion, all measurements were performed for classical bottom fixed turbines followed by measurements using the same turbine freely oscillating in streamwise direction, being the only change in the setup. Investigations were performed with single wind turbines, as well as with turbines operated in wind farm configuration.

Chapter 2 shows averaged statistical quantities of the near and far wake of a fixed and floating wind turbine obtained from stereoscopic PIV measurements. The major impact of the pitch motion of the turbine is a vertical upwards shift of mean and turbulent quantities. This results in reduced turbulent kinetic energy fluxes and available kinetic energy for a downwind turbine in offshore conditions. The upwards shift of the fluctuations causes increased fluctuation at top tip of a downstream turbine but can result in reduced fatigue loads over the whole rotor area. The induced increase in the mean vertical flow component can results in increased fatigue loads, that are not taken into account for classical bottom fixed turbines. A comparison of the experimental results with standard engineering level models shows, that the models do not cover effects introduced by platform pitch motion, such as the vertical shift in all velocity components, the averaged fluctuations and fluxes.

Chapter 3, characterizes the far wake of a fixed vs a floating turbine by means of eddy viscosity and the mixing length. Furthermore, wake to wake interactions are discussed in terms of the influence of the far wake on the statistical quantities of the downstream turbine's near wake. The descending order of the obtained eddy viscosity from fixed turbine, to floating turbine, to freestream inflow, shows a decreasing trend in the eddy viscosity with reduced opposing force on the flow. Vertical profiles of the mixing length calculated from measured data reveal an increase in turbulent mixing for the fixed turbine by having an increased drag on the flow due to its rigidity. The capability of the floating turbine to follow fluctuations in the flow reduces turbulent mixing in the far wake. The influence of the mixing length on the Reynolds stresses is present in the shear layer, where no disturbance by the nacelle, the rotation of the rotor and the oscillatory motion of the turbine in the floating case on near wake characteristics is observed. The eddy viscosity and the mixing length profiles derived from measured data, can be used to calibrate simplified

computational models, to increase performance and quality of predictions. Turbulent fluctuations are dampened by the ability of the floating turbine to follow the flow. This is followed by a suppressed entrainment of kinetic energy from undisturbed flow above the shear layer, which results in a reduced mean streamwise velocity as it is observed in the experiment. The reduced oscillation of the downwind turbine when compared to the first turbine suggests a reduction of motion induced fatigue loads. Further load reduction is expected for the floating downwind turbine due to the deflected wake fluctuations, when compared to the fixed turbine.

In chapter 4 low and high turbulence inflow conditions generated with an active grid as well as wakes of a fixed and floating turbine are characterized in time-, spectral- and spatial-domain. Measurements were taken using a hot-wire rake with 16 hot-wires positioned parallel to the rotor area at the turbine's position and at wake positions from 1 to 7 rotor diameters downstream. It was found that the actual inflow conditions and turbulent characteristics of the flow are important parameters for performance of the turbine and wake characterization. The wide range of fluctuations under active inflow conditions causes strong variations in the performance of both turbine types, which is transferred to a broader range of rotational frequencies as well as varying power coefficients. Under low turbulence, the presence of the turbine and the turbine type, fixed or floating, has highest impact on wake development. By deflecting flow, significant modifications of the floating turbine's wake in terms of kinetic energy transports as well as stresses, structures and shed tip vortices formed at the blade are induced. These structures are stable in the wakes of fixed turbines and drive wake characteristics. Still present for the floating wind turbine they are destabilized and smeared out. Also, the energy distribution over the scales is changed. Correlated flow patterns, which are distinct for the fixed turbine, were found to smear out for the floating turbine. Under high turbulence inflow with large incoming structures, the turbine type has a negligible influence on the flow, since the main energy transport mechanisms are driven by the inflow turbulence. The structural analysis using POD reveals, that the modes found under active inflow conditions have a higher complexity. However, due to the high amount of contained kinetic energy, only the first few modes are needed to reconstruct a representation of the flow situation that covers a high percentage of the original turbulent kinetic energy, thus characteristic fluctuations. Under passive inflow, the modes only contribute point-wise to the wake structure due to the absence of large correlated structures, thus many modes are needed to reconstruct an energetically representative composition of the flow. For both inflow conditions, the oscillation of the turbine has a subordinated influence on the reconstruction of the flow.

In total, the pitching motion of floating wind turbines in farms increases the turbine spacing needed to allow for enhanced wake recovery and to achieve the same energy yield as for bottom fixed turbines. The variability in fluctuations and inflow profiles of a floating wind turbine results in an increased effort in controlling single turbines and turbines in floating wind farms. This is further complicated by the not-synchronized oscillations of floating wind turbines in wind farms, resulting in further increased local variability of inflow profiles and hence potential fatigue load fluctuations. Due to the ability to follow the flow and to deflect and damp fluctuations, floating turbines are expected to benefit in terms of fatigue loads. The impact of the turbine type is of high interest for wind farms, where the averaged inflow conditions have low turbulence, so for these situations the oscillatory motions of floating wind turbines are of particular interest. For wind farm areas with generally high turbulence, the impact of the turbine type is of subordinated role and the optimization of turbine design and control for the wind farm are driven by the general presence of turbines and encompassed turbulence in the inflow.

6 Outlook

To gain further insights into induced effects of floating platforms on turbine performance and wake dynamics, other degrees of freedom, such as surge, heave and yaw motions, have to be isolated and investigated separately. Analogies to existing investigations for wake effects of wind turbines under yawed conditions could be drawn, by assuming a fixed pitch angle and neglecting the variation in inclination angle. This would allow to connect aspects of the results to a wider base of knowledge, since extensive work exists for yawed turbines. The emphasis of this work was on the pitch motion of the turbine under various turbulent inflow conditions, without taking water wave effects into account. A further approach would be to investigate wake patterns induced by periodic motions given by wave motions, which are of high interest for the induced fluctuations for floating wind turbines. Subsequent, knowledge about the influence of a combination of wind and wave fluctuations on the performance of a single turbine and its effects on the wake development would allow for more realistic evaluation of operational conditions of floating wind turbines and wind farms. Finally, validation of the results with full scale wake measurements would be of great interest, to embed found effects in model scale in full scale turbine operation and design.

Danksagung

Ich danke Prof. Dr. Joachim Peinke für das Ermöglichen dieser Arbeit und für die richtungsweisenden Impulse. Prof. Dr. Martin Kühn danke ich für das Begutachten der Arbeit. I thank Prof. Dr. Raúl Bayoán Cal for all the input to this work, all the discussions we've had, the advantage of working in his group and the pushing forward of this work. Thanks, Bayo! Ich danke Dr. Michael Hölling für alle Gespräche, Diskussionen und kritischen Fragen, die wir im Laufe der Jahre hatten, und dafür dass er immer für einen Ohrwurm gut war. Ich hoffe dass ich mir eine Scheibe von deiner besonnenen Art abgucken konnte. Danke auch an Joachim und Mike für das mir entgegengebrachte Vertrauen, dass ich das schon mache. Gerrit Kampers, Hendrik Heißelmann, Jannik Schottler, Dr. Jarek Puczylowski und Nico Reinke danke ich für die immer vorhandene Bereitschaft bei allen Fragen und anstehenden Aufgaben zu unterstützen. Dr. Matthias Wächter und David Bastine danke ich für die Unterstützung bei allen "stochastichen" Fragen. Dr. Gerd Gülker danke ich für die Unterstützung bei Fragen zu optischen Messmethoden, für seine organisatorische Arbeit und dass er das Feuer am Leben hielt. I also thank Betsy Camp, Nicholas Hamilton and Matt Melius for their support during the endless hours in the wind tunnel.
Diese Arbeit wurde durch ein Promotions-Stipendium der Deutschen Bundesstiftung Umwelt (DBU) gefördert. Ich danke der DBU und insbesondere Herrn Dr. Maximilian Hempel für viele positive Erfahrungen und die Unterstützung.

Nicht zu Letzt danke ich meinen Eltern, Larissa und Konstantin Rockel, und meiner Schwester, Elvira Mohr, für ihre grenzenlose Unterstützung während der Jahre und dafür, dass ihr nicht an mir gezweifelt habt. Danke.
Nicht genug danken, kann ich meiner Frau Rieke Jüchter für ihre bedingungslose Unterstützung, ihre Entbehrungen und für die Freiheiten, die ich mir rausnehmen durfte, um diese Arbeit zu erstellen. Ich liebe dich.

Lebenslauf

Stanislav Rockel

Geboren am 22. 07. 1982 in Kujbyschew (Russland)

seit 2016/01	Berater und Projektleiter im Bereich Smart Grid bei der BTC AG, Oldenburg
2014/06 - 2015/12	Wissenschaftlicher Mitarbeiter bei ForWind in der Arbeitsgruppe "TWiSt“ an der Carl von Ossietzky Universität Oldenburg
2011/07–2014/06	Doktorandenstipendium des Deutschen Bundesstiftung Umwelt (DBU)
seit 2011/07	Promotion in der Arbeitsgruppe "TWiSt“ an der Carl von Ossietzky Universität Oldenburg
2011/04 - 2014/06	Wissenschaftliche Hilfskraft bei ForWind in der Arbeitsgruppe "TWiSt“ an der Carl von Ossietzky Universität Oldenburg
2009/11–2011/02	Anfertigung der Diplomarbeit mit dem Titel: "Dynamische Eigenschaften einer schwimmenden Modell-Windenergieanlage“
2008/02–2008/07	Studentenaustausch mit ERASMUS Stipendium an der *Facultad de Ciencias de la Universidad de Zargoza* in Spanien
2004/10–2011/02	Studium Diplom-Physik an der Carl von Ossietzky Universität Oldenburg
1996–2003	Abitur am Herbartgynmasium Oldenburg in Oldenburg

List of publications

Rockel, S., Camp, E., Schmidt, J., Peinke, J., Cal, R. B., & Hölling, M. (2014). Experimental study on influence of pitch motion on the wake of a floating wind turbine model. Energies, 7(4), 1954-1985.

R.B. Cal, J. Peinke and M. Hölling had a supervising function. J. Schmidt performed the analytical wake model calculations (shown in Figure 19) and provided the model descriptions in Chapter 2.2 - "Wake models", as well as in the apendix. S. Rockel performed the scientific analysis as well as wrote the manuscript.

Rockel, S., Peinke, J., Hölling, M., & Cal, R. B. (2016). Wake to wake interaction of floating wind turbine models in free pitch motion: An eddy viscosity and mixing length approach. Renewable Energy, 85, 666-676.

R.B. Cal, J. Peinke and M. Hölling had a supervising function. S. Rockel performed the scientific analysis as well as wrote the manuscript.

Rockel, S., Peinke, J., Hölling, M., & Cal, R. B. Dynamic wake development of a floating wind turbine in free pitch motion subjected to turbulent inflow generated with an active grid. Renewable Energy, under revision.

R.B. Cal, J. Peinke and M. Hölling had a supervising function. S. Rockel performed the scientific analysis as well as wrote the manuscript.

Erklärung

Hiermit erkläre ich,

- dass eine Promotion zum Dr. rer. nat. angestrebt wird,
- dass ich diese Arbeit selbstständig verfasst und keine anderen als die angegebenen Hilfsmittel und Quellen benutzt habe
- dass die Dissertation in Teilen bereits veröffentlicht wurde, wie in der Publikationsliste dargestellt,
- dass ich die allgemeinen Prinzipien wissenschaftlicher Arbeit und Veröffentlichung, wie sie in den Leitlinien guter wissenschaftlicher Praxis der Carl von Ossietzky Universität Oldenburg festgelegt sind, befolgt habe,
- dass die Dissertation weder in ihrer Gesamtheit noch in Teilen einer anderen Hochschule zur Begutachtung in einem Promotionsverfahren vorliegt oder vorgelegen hat,
- dass im Zusammenhang mit dem Promotionsvorhaben keine kommerziellen Vermittlungs- oder Beratungsdienste (Promotionsberatung) in Anspruch genommen worden sind.

Oldenburg, der 02. August 2017

Stanislav Rockel